

ARTO HILTUNEN

# Photovoltaic Applications of Porous Atomic Layer Deposited Metal Oxides from Cellulose Templates



ARTO HILTUNEN

Photovoltaic Applications of  
Porous Atomic Layer Deposited Metal Oxides  
from Cellulose Templates

ACADEMIC DISSERTATION

To be presented, with the permission of  
the Faculty of Engineering and Natural Sciences  
of Tampere University,  
for public discussion at Tampere University,  
on 15 May 2020, at 12 o'clock.

# ACADEMIC DISSERTATION

Tampere University, Faculty of Engineering and Natural Sciences  
Finland

*Responsible  
supervisor  
and Custos*

Professor  
Nikolai Tkachenko  
Tampere University  
Finland

*Supervisor*

Senior Research Fellow  
Paola Vivo  
Tampere University  
Finland

*Pre-examiners*

Professor  
Olli Ikkala  
Aalto University  
Finland

Associate Professor  
Renata Solarska  
University of Warsaw  
Poland

*Opponent*

Professor  
Kati Miettunen  
University of Turku  
Finland

The originality of this thesis has been checked using the Turnitin OriginalityCheck service.

Copyright ©2020 author

Cover design: Roihu Inc.

ISBN 978-952-03-1573-3 (print)  
ISBN 978-952-03-1574-0 (pdf)  
ISSN 2489-9860 (print)  
ISSN 2490-0028 (pdf)  
<http://urn.fi/URN:ISBN:978-952-03-1574-0>

PunaMusta Oy – Yliopistopaino  
Tampere 2020



## ABSTRACT

Global warming, caused by the enormous use of fossil fuels to supply our energy demand, is forecast to have a negative net impact on the life on Earth. To fight the excessive heating of the planet, alternative energy technologies to replace the burning of fossil fuels should be explored. In many contexts hydrogen economy stands out as one of the most prominent alternative for the contemporary fossil economy. Hydrogen can be separated from water in the form of hydrogen gas, which reacts back to water when burned to heat or when used in an electrochemical cell to produce electricity. Thus hydrogen can provide a  $\text{CO}_2$  free source of heat and electricity if the processes for hydrogen gas production are  $\text{CO}_2$  free. This thesis deals with materials that are able to produce hydrogen gas from water using solar power as the driving force.

In this thesis we describe the fabrication of adjustable porous weblike metal oxide nanostructures from cellulose templates. The templated structures were tested in solar water splitting (i.e. hydrogen production) as well as in dye-sensitized solar cells. The fabrication begun by casting a porous cellulose template which then was coated with titanium dioxide using atomic layer deposition (ALD). The ability of the ALD-technique to make nanometer precision coatings enabled us to run optimization on the coating thickness for more efficient solar to hydrogen conversion. Moreover, as a result of varying the coating thickness we were able to reveal the progression of ALD- $\text{TiO}_2$  film growth on the cellulose templates. Finally, in order to extend the absorption of the  $\text{TiO}_2$  photoanodes an additional ALD- $\text{Fe}_2\text{O}_3$  layer was deposited on the surface of  $\text{TiO}_2$ . An increase in photocurrent was observed as a result of extended range of visible light absorption which was attributed to the formation of iron titanium oxides.

The results of this thesis clearly show that atomic layer deposition combined with cellulose templating can be used to fabricate materials for sustainable  $\text{CO}_2$ -free energy production that complies with the current climate goals. In light of the results presented here, we expect the ever developing atomic layer deposition techniques of new materials together with the abundance of cellulose templates available in forms of nanofibers and nanocrystals to have the potential to provide new high performance materials for the needs of sustainable energy production.

## TIIVISTELMÄ

Fossiilisten polttoaineiden liiallisesta käytöstä aiheutuvan ilmaston lämpenemisen ennustetaan vaikuttavan negatiivisesti elämämme laatuun. Lämpenemisen pysäyttämiseksi tulisi etsiä vaihtoehtoisia energiantuottotapoja öljyn, hiilen ja kaasun polttamiselle. Useissa tulevaisuudennäkymissä vety nostetaan esille kaikkein lupaavimpana vaihtoehtona fossiilisten polttoaineiden korvaajaksi. Vetyä voidaan erottaa vedestä vetykaasuna, joka voidaan polttaa lämmöksi tai muuntaa sähköksi sähkökemiallisessa kennossa. Molemmissa prosesseissa vety reagoi hapen kanssa muodostaen vettä ainoana päästönään. Näin ollen vety voisi taata hiilidioksidivapaan lämmön- ja sähkönlähteen, mikäli vedyn tuottamiseen käytetty energia olisi hiilidioksidivapaata. Tämä väitöskirja käsittelee materiaaleja, jotka pystyvät tuottamaan vetykaasua vedestä käyttäen energianlähteenä auringonvaloa.

Tässä työssä valmistimme huokoisia metallioksidinanorakenteita selluloosamuotteja apuna käyttäen. Muottien avulla valmistettujen materiaalien tehokkuus testattiin valokemiallisessa vedyntuotannossa sekä väriaineaurinkokennojen elektrodina. Rakenteiden valmistaminen alkaa huokoisen selluloosamuotin levittämällä, joka päällystetään seuraavassa vaiheessa titaanidioksidilla käyttäen atomikerroskasvatustekniikkaa (ALD). Titaanidioksidikerroksen paksuutta kyettiin optimoimaan ALD-tekniikan nanometriluokan tarkkuuden avulla, jolloin vedyntuotannon tehokkuutta pystyttiin parantamaan. Tutkiessamme useita eri pinnoitepaksuuksia onnistuimme lisäksi kuvaamaan ALD:llä kasvatettujen titaanidioksidikalvojen kasvun etenemistä selluloosamuottien päällä. Väitöskirjatyön viimeisessä vaiheessa tutkimme titaanidioksidirakenteiden valon absorptiokaistan laajentamista lisätyllä rautaoksidipinnoitekerroksella. Rautaoksidipinnoitteella onnistuttiin kasvattamaan valon absorptiota, jolla saavutettiin suurempi valokemiallisten kennojen virta. Titaani- ja rautaoksidien havaittiin sekoittuvan keskenään valmistusprosessin aikana, minkä todettiin olevan välttämätöntä kennon toiminnan kannalta.

Tämän väitöskirjatyön tulokset osoittavat, että yhdistämällä selluloosamuottitekniikan ja atomikerroskasvatuksen voidaan valmistaa materiaaleja hiilidioksidivapaan energiantuotannon sovelluksiin. Näiden tulosten valossa uskomme, että yhä kehittyvillä ALD-tekniikoilla sekä uusilla nanoselluloosamateriaaleilla on mahdollista valmistaa entistä tehokkaampia materiaaleja ilmastotavoitteiden saavuttamiseksi.

## PREFACE

I would like to begin this book by expressing my gratitude to Professor Helge Lemmetyinen for giving me the chance to begin as his PhD student in January 2014. As I have my background in electrical engineering, I had a lot to catch up in chemistry. In this context, Professor Lemmetyinen's way of finding the essential in the midst of complex phenomenon (and data) meant great deal for me. Therefore, I would like to thank him for being a great teacher of chemistry as well as science in general.

This research was conducted in Laboratory of Chemistry and Bioengineering at Tampere University of Technology, which today is known as the Chemistry and Advanced Materials research group at Tampere University. Funding from TEKES (Business Finland) project Photosphere, and personal research grants from Finnish Foundation for Technology Promotion and Fortum Foundation are gratefully acknowledged.

I would like to thank Professor Nikolai Tkachenko for continuing the thesis supervision after Professor Lemmetyinen's retirement. His broad expertise was extremely valuable during these years. Also, I would like to thank Dr. Paola Vivo for her help and advice throughout the years, in particular, in the beginning and in the end of the process where perhaps the most support is quite often needed.

I find the work in the field of experimental chemistry quite exciting! Not only because of the sophisticated experiments one is privileged to perform but also because of the fantastic people one meets. I would like to thank all the colleagues, co-authors, laboratory personnel and faculty staff I have got to work with. One a personal note, I wish to mention Tero-Petri Ruoko, Kirsi Virkki, Venla Manninen, Lauri Judin, and Henri Salonen for the good time we had in the lab and outside the lab.

Finally, I wish to take the opportunity to say how I am grateful for my family and friends. Having you in my life is a profoundly beautiful thing. I love you and I look forward to meeting you wherever in the World you may be.

Tampere April 26, 2020  
Arto Hiltunen

# CONTENTS

Abstract . . . . .	iii
Tiivistelmä . . . . .	iv
Preface . . . . .	v
List of symbols and abbreviations . . . . .	viii
List of publications . . . . .	x
Author's contribution . . . . .	xi
1. Introduction . . . . .	1
1.1 Research objectives and scope of the thesis . . . . .	2
1.2 Outline . . . . .	3
2. Theoretical background . . . . .	4
2.1 Solar cells . . . . .	4
2.2 High surface area electrodes . . . . .	13
2.3 Templating for high surface area . . . . .	13
3. Materials and methods . . . . .	15
3.1 Celluloses . . . . .	15
3.2 Atomic layer deposition . . . . .	18
3.3 Device assembly . . . . .	19
3.4 Photovoltaic characterization . . . . .	21
4. Results and discussions . . . . .	23
4.1 Cellulose templating for ALD of metaloxides . . . . .	23
4.2 Photovoltaic applications of the templated photoanodes . . . . .	29
5. Summary and future outlook . . . . .	38
References . . . . .	41
Original papers . . . . .	52

Paper I . . . . .	53
Paper II . . . . .	63
Paper III . . . . .	71
Paper IV . . . . .	82

## LIST OF SYMBOLS AND ABBREVIATIONS

aCNC	Aldehyde functionalized CNC
ALD	Atomic layer deposition
CA	Cellulose acetate
CNC	Cellulose nanocrystal
CNF	Cellulose nanofiber
c-Si	Crystalline silicon
CZTS	Copper zinc tin sulfate
DSSC	Dye-sensitized solar cell
EIS	Electrochemical impedance spectroscopy
EtOH	Ethanol
FTO	Fluorine doped tin oxide
hCNC	Hydrazine functionalized CNC
HER	Hydrogen evolution reaction
IPCC	Intergovernmental panel on climate change
<i>IPCE</i>	Incident photon to current efficiency
ITO	Indium doped tin oxide
NHE	Normal hydrogen electrode
OER	Oxygen evolution reaction
<i>PCE</i>	Power conversion efficiency
PEC	Photoelectrochemical cell
PV	Photovoltaic
redox	Oxidation-reduction
RHE	Reversible hydrogen electrode
sCNC	Sulfate half-ester functionalized CNC
SEM	Scanning electron microscope
SQ	Shockley-Queisser
STH	Solar to hydrogen
TAS	Transient absorption spectroscopy
TDMAT	Tetrakis(dimethylamino)titanium
TEM	Transmission electron microscope
UV	Ultraviolet
XPS	X-ray photoelectron spectroscopy
XRD	X-ray diffraction

$e^-$	Electron
$E$	Energy
$E_{\text{total}}^0$	Total standard reduction potential of reaction
$FF$	Fill factor
$h^+$	(Electron) hole
$I_{\text{sc}}$	Short circuit current
$I$	Current
$j_{\text{photo}}$	Photocurrent density
$P_{\text{light}}$	Power of light
$S^0$	Dye molecule ground state
$S^+$	Oxidized dye molecule
$S^*$	Excited state
$V$	Voltage
$V_{\text{bias}}$	Bias voltage
$V_{\text{oc}}$	Open circuit voltage
$\eta_{\text{SQ}}$	Schokley-Queisser efficiency
$\eta_{\text{STH}}$	Solar to hydrogen efficiency

## LIST OF PUBLICATIONS

- I. Hiltunen, A., Lahtonen, K., Saari, J., Ojanperä, A., Sarlin, E., Wondraczek, H., Efimov, A., Kaunisto, K., Vivo, P., Maccato, C., Barreca, D., Fardim, P., Tkachenko, N., Valden, M. and Lemmetyinen, H., *Tailored Fabrication of Transferable and Hollow Weblike Titanium Dioxide Structures*. ChemPhysChem, 2017, 18, 64
- II. Hiltunen, A., Ruoko, T-P., Iivonen, T., Lahtonen, K., Ali-Löytty, H., Sarlin, E., Valden, M., Leskelä, M. and Tkachenko, N., *Design Aspects of All Atomic Layer Deposited  $\text{TiO}_2$ - $\text{Fe}_2\text{O}_3$  Scaffold-Absorber Photoanodes for Water Splitting*, Sustainable Energy Fuels, 2018, 2, 2124-2130
- III. Ruoko, T-P., Hiltunen, A., Iivonen, T., Ulkuniemi, R., Lahtonen, K., Ali-Löytty, H., Valden, M., Leskelä, M., Tkachenko, N., *Charge Carrier Dynamics in Tantalum Oxide Overlayed and Doped Hematite Photoanodes* J. Mater. Chem. A, 2019, 7, 3206-3215
- IV. Hiltunen, A., Or, T., Lahtonen, K., Ali-Löytty, H., Tkachenko, N., Valden, M., Sarlin, E., Cranston, E., Moran-Mirabal, J., and Vapaavuori, J., *Ultrathin-walled 3D Inorganic Nanostructured Networks Templated from Crosslinked Cellulose Nanocrystal Aerogels*, Submitted



## AUTHOR'S CONTRIBUTION

The realization of this thesis has been a joint effort of multiple research groups with a major scientific contribution from all of the co-authors of the included research papers. In this chapter the doctoral candidate's personal scholarly contribution to the published papers is described.

- I. Candidate Hiltunen chose the cellulose fabrication method to be used from literature and fabricated the films accordingly. His responsibility was the characterization of the films by SEM after the ALD of  $\text{TiO}_2$ . Based on these characterizations he developed the technique for transferring the films. These films were used as electrodes in dye-sensitized solar cells, which were built and characterized by him. Hiltunen wrote the manuscript draft, coordinated the manuscript preparation and was the corresponding author for this paper.
- II. Hiltunen designed the photoanodes together with Dr. Ruoko. Hiltunen had major contribution in planning and managing this research project. Personally he performed the post treatments after ALD, photoelectrochemical measurements, SEM imaging, transient photocurrent measurement, and the pump-probe experiment. Hiltunen wrote the manuscript draft, coordinated the manuscript preparation and was the corresponding author for this paper.
- III. Hiltunen carried out the *IV*-curve measurements and the electron microscopy imaging of the photoanodes. Experimental part of EIS and TAS were conducted by Dr. Ruoko. Hiltunen contributed in the data analysis and manuscript preparation.
- IV. Hiltunen planned and designed the study together with Dr. Vapaavuori. Together they share the responsibility of the project management. Hiltunen was responsible for the photoanode design, including the selection of the ALD- $\text{TiO}_2$  coating thicknesses to be used. Personally he performed the SEM imaging, and photoelectrochemical characterizations. The manuscript draft was written by Hiltunen and Vapaavuori.



# 1. INTRODUCTION

Global warming is considered to be one of the biggest challenges of our time. To prevent the heavy weather conditions to have its negative effect on us, global warming should be limited to 1.5 °C with respect to the pre-industrial levels, according to the 2018 Special Report by IPCC.<sup>1</sup> Currently, the world is 1 °C warmer (see Figure 1.1).<sup>1,2</sup> Heart of the problem lies in the world's immense energy need that is met by burning fossil fuels. The fossil fuel combustion raises the level of greenhouse gases in the atmosphere which in turn leads to the global temperature rise. In the combat against climate change, the scientists' task is to develop alternative energy technologies free from greenhouse gas emissions to replace the fossil fuels.

The Sun radiates more energy onto the Earth in an hour, than the whole world consumes in a year.<sup>3</sup> Therefore, due to its vast potential, in many scenarios solar energy is projected to be one of the main sources of energy in the future. Solar energy can be harvested — in a greenhouse gas free manner — using photovoltaic technology that converts the solar irradiation into electrical energy or by using solar thermal collectors that convert the irradiation into heat. The drawback of solar technology is in its difficult storing. This is particularly inconvenient due to the changes in the availability of solar energy. As a consequence, efficient ways to store solar energy would be required for its large scale utilization.

Electrical energy produced with solar cells could be stored in batteries. However, the high price of the present battery technology has limited the build-up of large battery centers. One prominent approach for storage is to use solar energy for hydrogen production from water. Hydrogen is an efficient fuel which can be stored, and transported compactly in tanks in its liquid form. Hydrogen can be directly burned to heat or converted to electric energy in a fuel cell. The only emission from these processes is clean water.

In the course of this work, we have combined the latest semiconductor fabrication technology and nanocelluloses to prepare materials, which are capable of producing hydrogen fuel from water, or which can to convert solar light to electricity.

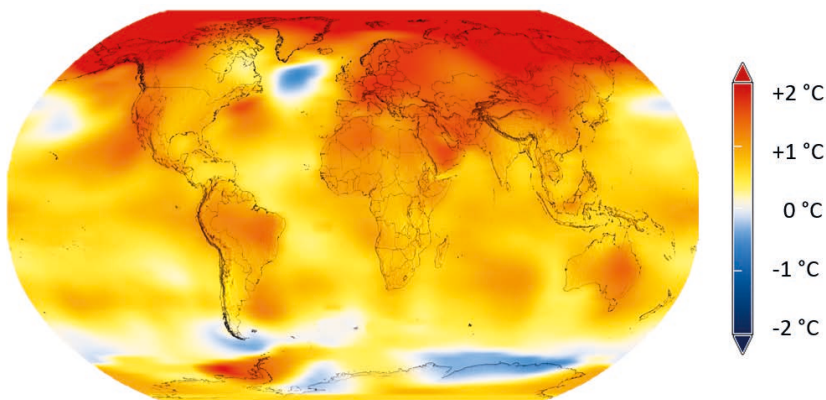


**Figure 1.1** Average temperature of Earth during 2014-2018 compared to that of 1951-1980 (Credit by NASA's Scientific Visualization Studio).<sup>2</sup>

## 1.1 Research objectives and scope of the thesis

In many applications, porous structures with high specific surface area are required to reach high efficiency. The nanocellulose materials selected for the study possess this property, however, cellulose itself is not photoactive. Therefore, this function has to be implemented onto the cellulose from other materials which in this thesis are semiconducting metal oxides, either  $\text{TiO}_2$ ,  $\text{Fe}_2\text{O}_3$ , or their combination. Among the many possible thin film technologies, we chose atomic layer deposition (ALD) as it can create metal oxide coatings with subnanometer precision therefore allowing us to precisely tune the coating thicknesses.

In this thesis, the suitability of porous cellulose (aerogel)-based templates for ALD of metal oxides is explored, and the application of the prepared structures in photovoltaic devices is demonstrated. We show that, combining ALD and cellulose based templating allows the preparation of high specific surface area semiconducting electrodes with control over multiple parameters: electrode thickness, composition of the metal oxide layer, layer thickness, and porosity. In addition, we show that the

electrodes can be prepared directly on the substrate (e.g. FTO) or they can be transferred from the deposition substrate to that of the final application which can even be curved. Moreover, the possibility to extend the light absorption range of the  $\text{TiO}_2$  with an additional ALD- $\text{Fe}_2\text{O}_3$  coating layer is shown. The porous metal oxide films are tested as photoelectrodes in dye-sensitized solar cells or in photoelectrochemical cells capable of solar water splitting. In short, the research questions can be summarized as follows:

- Can atomic layer deposition of metal oxides be applied on porous cellulose templates in order to make high specific surface area electrodes for photovoltaic devices?
- What are the advantages and disadvantages of this approach?
- Can the performance of the templated metal oxide photoanodes be improved further with yet another atomic layer deposited coating (e.g. ALD- $\text{Fe}_2\text{O}_3$ )?

## 1.2 Outline

The thesis consists of a short *Theoretical background* chapter which will introduce the reader to the main concepts behind this work. In the *Materials and methods* chapter, the experimental procedures are described. *Results and discussion* chapter will present in separate sections first the structure of the cellulose templated metal oxides, and second their applications in photovoltaic devices. The main outcomes of this work are summarized the chapter *Summary and future outlook*. The original papers are included at the end of the thesis.

## 2. THEORETICAL BACKGROUND

In this chapter we give a general overview on the current status of the state-of-the-art photovoltaic devices. First, we describe the working principles of dye-sensitized solar cells which were the application in **Paper I**, and then focus on solar water splitting that was the application in **Papers II, III and IV**. These photovoltaic applications especially benefit from a high specific surface area active electrode. The remainder of this chapter is therefore devoted to the high specific surface area structures.

### 2.1 Solar cells

Solar cells are devices that are able to convert the energy carried by light into another form of energy. Photovoltaic solar cells convert the energy of light to electricity.

The energy of light is carried by photons, which are emitted by the Sun at varying amounts depending on the photon's energy. Figure 2.1a presents the solar spectrum which shows the amount of photons that the Sun radiates on Earth as a function of the photon's wavelength. An ideal solar cell would absorb all of these photons, and convert them to electricity. The maximum theoretical solar to electricity conversion efficiency for a single junction solar cell is 33.7 % (under 1 Sun conditions) which is obtained with a band gap of 1.37 eV.<sup>6</sup> This calculation is based on the detailed-balance model first presented by Shockley and Queisser (see Figure 2.1b).<sup>7</sup>

Figure 2.2 shows how close different solar cell technologies are to the theoretical limit.<sup>6</sup> In this sense the most mature technologies are c-Si, GaAs, and GaInP which can provide efficiency that is more than 75 % of the Shockley-Queisser limit. Dye-sensitized solar cells, together with organic, CZTS, and PbS quantum dot cells are yet to achieve even half of the theoretical maximum. The record efficiencies<sup>8</sup> for GaAs is 27.8 % and for c-Si 26.1 %. Multijunction cells employing the GaInP absorber have reached 47.1 %. Noteworthy is that perovskite solar cells have surpassed

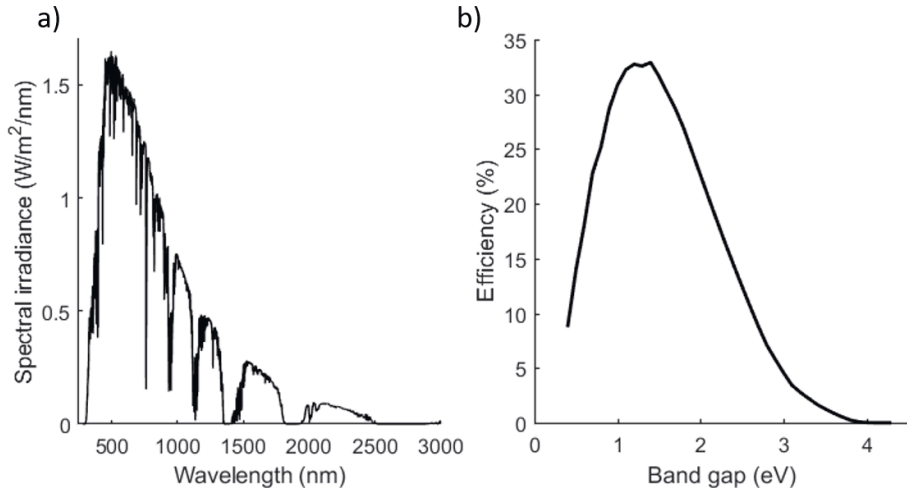


**Figure 2.1** a) The solar spectrum (ASTM G173-03, Global tilt 37°)<sup>4</sup>, b) The Shockley and Queisser limit according to Rühle.<sup>5</sup>

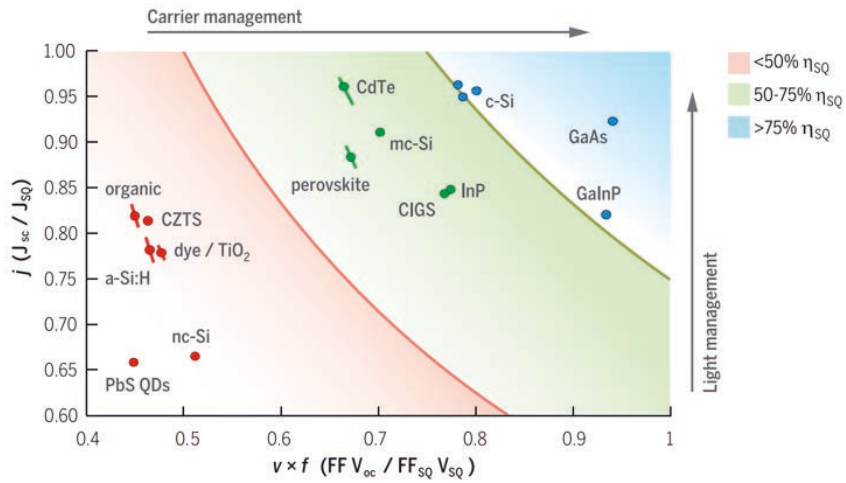


**Figure 2.2** The graph describes the maturity of various photovoltaic technologies. Solar cell types in the blue area are the most advanced technologies having reached over 75 % of the Shockley-Queisser limit ( $\eta_{SQ}$ ). From Science 15 Apr 2016: Vol. 352, Issue 6283, aad4424. Reprinted with permission from AAAS.

CdTe technology with efficiency of 25.2 % against 22.1 %, despite the fact that perovskite solar cells have been developed only for 10 years<sup>9</sup> while CdTe technology has been developed since 1950s.<sup>10</sup>

### 2.1.1 Dye-sensitized solar cells

The dye-sensitized solar cell is one of the many types of solar cell technologies developed to date. The major breakthrough in the field occurred in 1991 when Brian O'Regan and Michael Grätzel demonstrated 7-8 % efficiency which meant tenfold increase over the state-of-the-art.<sup>a</sup> The idea behind dye-sensitized solar cells is to enhance the light absorption of a transparent semiconductor with dye molecules that are attached to the semiconductor surface. The breakthrough of O'Regan and Grätzel was to use nanometer sized titanium dioxide particles to provide a high specific surface area for dye coating that resulted in sufficient light absorption. A 10 micrometer thick film made of nanometer sized particles provides roughly 1000 times more surface for dye coating compared to a flat surface of the same size.<sup>14;15</sup> The idea behind the dyeing process is illustrated in Figure 2.3.

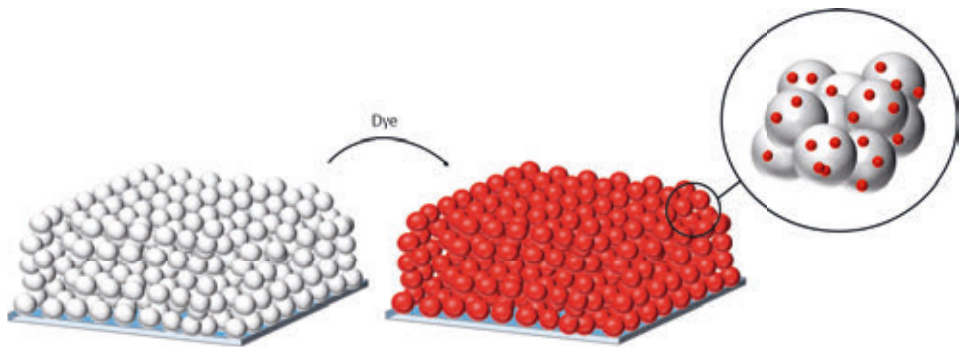


**Figure 2.3** Principle of using high surface area electrodes to achieve strong visible light absorption in dye-sensitized solar cells.

In a dye-sensitized solar cell the functions of charge transport and light absorption are divided between the  $\text{TiO}_2$  electrode and the dye, making them distinctively different to Si, CdTe, CIGS or III/V solar cells. Absorption of a photon by the

<sup>a</sup>Recommended reading of seminal work preceding the famous 1991 paper: Matsumura et al. (1977) *Dye-sensitization on the Photocurrent at Zinc Oxide Electrode in Aqueous Electrolyte Solution*,<sup>11</sup> Beley et al. (1981) *Dye sensitization of ceramic semiconducting electrodes for photoelectrochemical conversion*,<sup>12</sup> Desilvestro et al. (1985) *Highly efficient sensitization of titanium dioxide* (1985)<sup>13</sup>



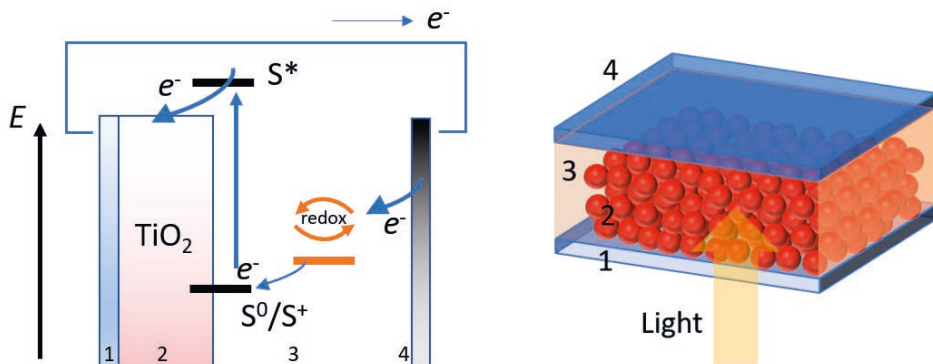


**Figure 2.4** Energy diagram for charge transfer in a DSSC together with a schematic drawing of an actual device. Numbers in the drawings refer to: 1) transparent electrode, 2) high specific surface area electrode, 3) electrolyte, 4) counter electrode.

dye excites an electron from the ground state  $S^0$  of the molecule to the excited state  $S^*$  from where it is further injected to the conduction band of  $\text{TiO}_2$ , leaving behind an oxidized dye molecule  $S^+$ . Timescale for these processes is in the range of femtoseconds to hundreds of picoseconds depending on the dye. To complete a cycle, charge is transferred through the external circuit to the counter electrode, and further to the redox electrolyte that regenerates (reduces) the oxidized dye. The regeneration cycle occurs in the range of 100 ns to 10  $\mu\text{s}$ .<sup>14;16</sup> The energy diagram of a DSSC is depicted in Figure 2.4.

Coming back to Figure 2.2, we see that dye-sensitized solar cells can provide less than 50 % of the theoretical maximum. The highest reported efficiency for a DSSC is today 12.3 %, <sup>8</sup> therefore it's obvious that there is still plenty of space for improvement. The challenges lie in the *carrier management* which in the graph is given as the product of fill factor ( $FF$ ) and open circuit voltage ( $V_{oc}$ ).<sup>6</sup> State-of-the-art devices today rely on  $\text{TiO}_2$  nanoparticle electrode and liquid electrolyte which together are responsible for the losses in voltage and fill factor.

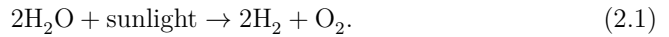
One of the main challenges is the low redox potential of the commonly used iodide/triiodide ( $\text{I}^{3-}/3\text{I}^-$ ) electrolyte, which causes a large potential loss in the device.<sup>16</sup> Alternative electrolytes have been developed (e.g. cobalt complexes,<sup>17</sup> copper complexes,<sup>18</sup> ferrocene based,<sup>19</sup> and organic disulfide/thiolate based<sup>20;21</sup>) which have better matched redox potential with the dye, however, their large size causes slow dye regeneration due to slow diffusion of the redox species within the  $\text{TiO}_2$  pores.<sup>22</sup>

Another challenge caused by the nanoparticle morphology is the large density of trap states concentrated at the grain boundaries of the film. The electron transport is therefore greatly slowed down by the trapping/detrapping events occurring during their transport through the nanoparticle structure.<sup>23;24</sup>

The problems related to the diffusion of redox species and to the charge transport through the nanoparticle electrode are preventing the dye-sensitized solar cell technology to approach the Shockley-Queisser limit. These challenges, caused by the nanoparticulate morphology, serves as a motivation to look for alternative high specific surface area photoanodes.

### 2.1.2 Solar water splitting

Solar water splitting means making *fuel out of water* using the power of the Sun to drive the reaction. This is achieved via a reaction where two water molecules are split into two hydrogen molecules and one oxygen molecule according to reaction

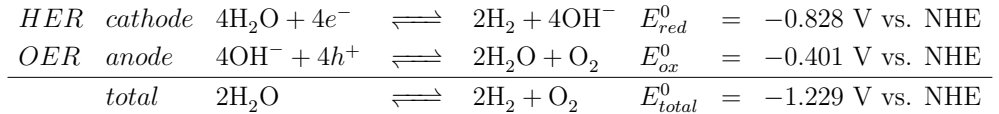


Solar water splitting is typically achieved via either having an external solar cell connected to an electrolyser (PV/electrolysis), or in a photoelectrochemical cell (PEC) where the photoanode is immersed directly in water.<sup>25</sup> Competence of these devices is assessed based on the solar-to-hydrogen (STH) conversion efficiency given as

$$\eta_{\text{STH}} = \frac{j_{\text{photo}} \cdot (1.23 \text{ V} - V_{\text{bias}})}{P_{\text{light}}}, \quad (2.2)$$

where  $j_{\text{photo}}$  (mA/cm<sup>2</sup>) is the photocurrent,  $V_{\text{bias}}$  is the applied bias voltage, and  $P_{\text{light}}$  (mW/cm<sup>2</sup>) is the light intensity.<sup>26</sup> The thermodynamical upper limit of solar-to-hydrogen conversion for a single junction device is in the range of 29-34 %. However, taking into account unavoidable losses in the system realistically achievable efficiency lies in the range of 10-15 %.<sup>25</sup> Obviously, multijunction systems can reach even higher efficiencies. For a multijunction PEC device employing III/V semiconductor 12.4 % has been reported.<sup>27</sup> For a PV/electrolyser system 30 % STH conversion was recently achieved.<sup>28</sup>

The half cell reactions written down below (in alkaline electrolyte) describe the hydrogen evolution reaction (HER) at the cathode and the oxygen evolution reaction (OER) at the anode.<sup>26</sup> From these equations one sees that it takes two electrons to produce one molecule of  $H_2$ . However, the OER has been identified to be the rate limiting step in solar water splitting because it is four electron reaction with slow kinetics compared to the competing recombination processes.<sup>29</sup>



The redox potential,  $E_{total}^0$ , for the overall reaction is  $-1.23$  V meaning the semiconductor band gap should be at least  $1.23$  eV to be able to drive the reaction. In practice, the band gap should be larger,  $1.8$ – $2.2$  eV, to account for kinetic losses due to overpotentials for OER and HER, and thermodynamic losses in the cell.<sup>30;31</sup> In addition to having a correct size band gap, the energy levels of the semiconductor should be matched with the OER and HER potentials; the conduction band edge should be above that of the HER potential and the valence band should be below that of the OER potential.<sup>26</sup> Figure 2.5 shows some common semiconductors and their band energies with respect to the water oxidation and reduction reaction potentials.

In this work we use the PEC type solar water splitting i.e. we employ semiconductors immersed in the electrolyte to directly drive the reaction on the semiconductor's surface (Figure 2.6). The advantage of the PEC technology over PV/electrolyser is that fewer compounds are needed because the whole cell can be made to a single monolithic device.<sup>26</sup> Although technically the system is less complicated, a lot is demanded on the photoanode material. An ideal PEC photoanode should be good light absorber, be able to perform water oxidation, have catalytic property for OER, and be stable under the reaction conditions. In addition, to make it in large-scale production the materials should be low cost, safe, and environmentally friendly. Today there is no single material that would satisfy all the conditions.<sup>25;26;31</sup>

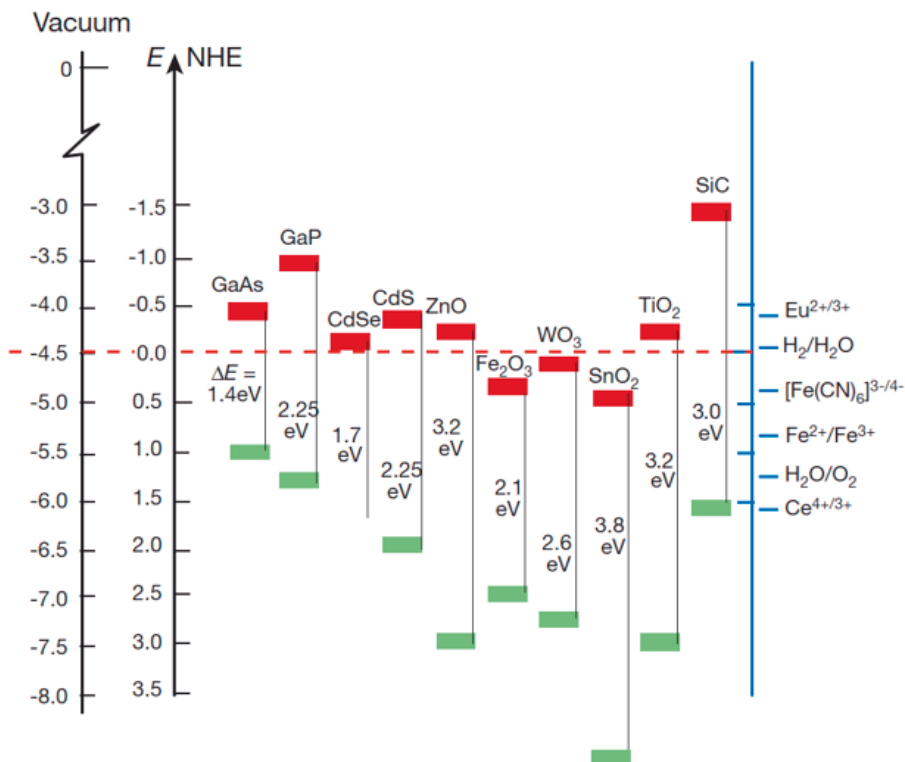


**Figure 2.5** Band energies of common semiconductors with respect to OER and HER reactions.<sup>32</sup> Reprinted by permission from Springer Nature: Nature volume 414, pages 338-344, Photoelectrochemical cells, Michael Grätzel, Copyright (2001)

### Semiconductors used in this work

**Hematite**,  $\alpha\text{-Fe}_2\text{O}_3$ , fulfills many of the aforementioned conditions for water splitting and has therefore been considered as a promising photoanode material. Hematite has a 2.0 - 2.2 eV band gap,<sup>33</sup> fitting well into the ideal range of 1.8-2.2 eV. Furthermore, it is stable under neutral and basic conditions, abundant and safe to handle. Despite the multiple favorable qualities of hematite, there are some notable downsides. Hematite has an extremely short hole ( $h^+$ ) diffusion length 2-10 nm,<sup>31;34</sup> that prevents the holes generated in the bulk to take part in the water oxidation reaction at the electrode surface. Another drawback is that its conduction band edge is below that of the HER potential.<sup>33</sup> This however could be overcome in a tandem

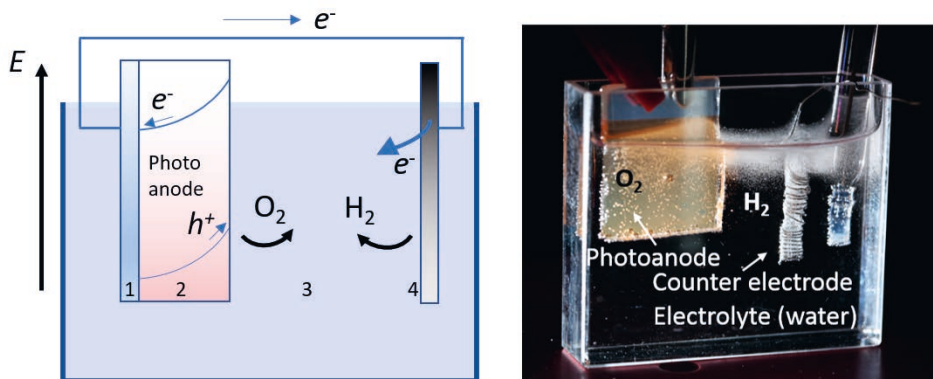


**Figure 2.6** Left) Schematic drawing of a water splitting cell: 1) transparent electrode, 2) photoanode (e.g.  $\text{TiO}_2$ ), 3) electrolyte (water), 4) counter electrode. Right) A photograph of the setup used in this work. The bubbles on the photoanode are oxygen gas and the bubbles on the coiled counter electrode are hydrogen gas (large bias voltage was used to get a high rate of gas generation for the photo).

PEC configuration. Coupled with an appropriate photocathode, the system could reach 15 % STH conversion efficiency.<sup>31</sup>

**Titanium dioxide**,  $\text{TiO}_2$ , was the first material on which photoelectrochemical water splitting was demonstrated.<sup>35;36</sup> Similarly to hematite, it fulfills many of the conditions for an ideal photoanode material such as the non-toxicity and abundance. Unlike hematite,  $\text{TiO}_2$  does not suffer from short carrier diffusion lengths.<sup>37;38</sup> Moreover, having the conduction band above the HER potential and valance band below that of the OER it can perform fully solar driven water splitting without assistance from external power sources as was shown by Fujishima and Honda in 1972.<sup>36</sup> The main disadvantage of  $\text{TiO}_2$  is its large band gap 3.0-3.2 eV meaning it can only absorb UV-light therefore greatly limiting the obtainable efficiency. Figure 2.7 shows the parts of solar spectrum that can be absorbed by hematite or  $\text{TiO}_2$ .

Due to the multiple attractive properties of hematite and titanium dioxide, in this work, we study them and their combination as the photoanode materials for solar water splitting. Successful combination of the favorable properties of the two materials would lead to finding a safe and efficient material for hydrogen production which is why this combination still is in the focus of researchers after decades of research. The problem caused by the short hole diffusion length of hematite could be solved by creating a porous material which would allow the infiltration of water into the

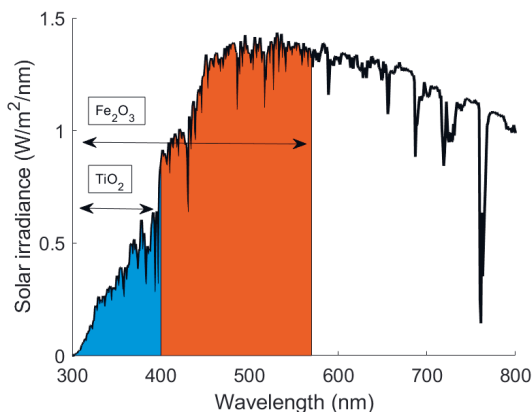


**Figure 2.7** The parts of solar spectrum absorbed by titanium dioxide ( $\text{TiO}_2$ ) and hematite ( $\text{Fe}_2\text{O}_3$ ).

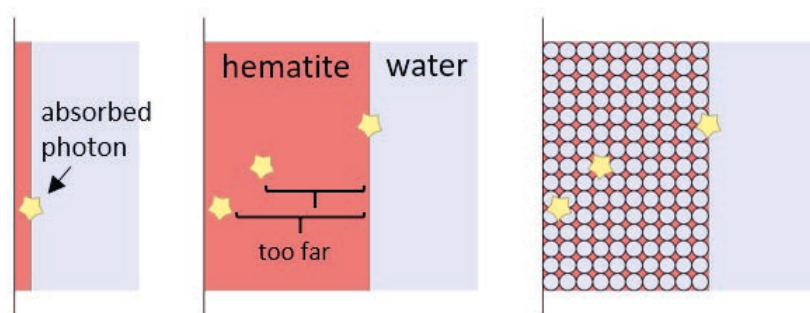


**Figure 2.8** The benefits of using porous structures in solar water splitting. Left) A thin photoanode results in low absorbance but the photogenerated holes can participate to the OER reaction. Center) thick films have high absorbance but the photogenerated holes are too far from the water interface. Right) porous structures create high absorbance and close proximity of the water interface.

pores. Now the photogenerated holes ( $h^+$ ) would have close proximity of water interface thus being able to take part in the OER reaction. In order to work efficiently the hematite layer shouldn't be thicker than the hole diffusion length (2-10 nm). A layer this thin would require another material to carry it which could be another metal oxide — titanium dioxide for example. The concept bears high resemblance to the idea behind dye-sensitized solar cells and is known as the scaffold-absorber approach.<sup>33</sup> Figure 2.8 illustrates the benefits of using porous materials in solar water splitting.

## 2.2 High surface area electrodes

Many applications benefit from nanostructuring in order to increase the active surface area with respect to the geometrical surface area. Nanostructured materials are commonly divided into four groups — 0D, 1D, 2D, 3D — according to the dominant dimensionality.<sup>39</sup> 0D materials include nanoparticles or quantum dots,<sup>40</sup> 1D materials include nanorods, wires or tubes,<sup>41</sup> 2D refers to sheets and plates,<sup>42</sup> and with 3D materials we mean porous structures such as hollow spheres or hollow fibers creating an interconnected network.<sup>43</sup>

Dimension of the structure will greatly define its properties. 0D nanoparticles can be used to cast films with high surface-to-volume ratio ( $\text{m}^2/\text{m}^3$ ) also known as high specific surface area making them ideal for fabricating thin films with good visible light absorption as in dye-sensitized solar cells.<sup>40</sup> Quantum dots are yet another example of 0D nanoparticles. 1D nanostructures in particular in the form of nanorods have found applications in batteries as well as in solar cells due to the unidirectional confined charge transport along the nanorod.<sup>41</sup> The most famous example of a 2D material is graphene that has found applications in many fields of electronics, and photonics.<sup>44</sup>

3D materials can be made in numerous different shapes that vary in pore size, distribution, geometry, and the nature of the structure frame. Owing to the great tunability of the 3D networks they are found in multiple applications including solar cells, photocatalysis, energy storage, and even self-cleaning surfaces and antifogging coatings.<sup>43</sup>

The desired dimensionality can be achieved via various different synthesis routes which can roughly be divided into two groups: template-free synthesis and templated synthesis. Examples of template free approaches are sol-gel synthesis, solvothermal/hydrothermal methods, and electrochemical film growth.<sup>43</sup> While the template-free synthesis is often simple, the downside is the resulting large variation in pore size distribution or irregular pore shapes. In this work we used templated approach which will be discussed in detail in the next section.

## 2.3 Templating for high surface area

Template-based methods often offer more regular pore size and shape distribution compared to the non-templated methods.<sup>43</sup> In a template-based method a separate

structure (i.e. the template) that possesses the desired pore size, shape, and distribution is used to give these properties to the deposited material. More precisely this is so called hard templating method in contrast to soft templating methods.<sup>43</sup>

Commonly used hard template materials include metal oxides (e.g. silica and alumina) or polymers (e.g. polystyrene, poly methyl methacrylate and celluloses). The selected template should be compatible with the target material processing conditions. The inorganic templates are very robust but the use of organic templates might in some cases be limited due to for example thermal resistance issues. Sometimes template removal is desired leaving behind a hollow structure. Silica can be removed using highly potent acids such as HF, and alumina using alkali solutions. Polymer templates, however, are more easily removed with organic solvents or by burning. Obviously, the coating (and the substrate) should withstand the template removal process.<sup>43</sup>

In exchange for the wet chemistry routes for the active material deposition, atomic layer deposition stands out as an excellent candidate due to its high precision. Kemell et al. were the first to combine cellulose templates and ALD-TiO<sub>2</sub> by applying the method on filter papers.<sup>45</sup> Hyde et al.<sup>46;47</sup> studied the properties of ALD-coated cotton. Korhonen et al.<sup>48</sup> used nanofibrillated cellulose (NFC) as templates and in addition to TiO<sub>2</sub> also deposited ZnO and TiO<sub>2</sub>. Buesch et al.<sup>49</sup> coated a cellulose nanocrystal (CNC) template with ALD-Al<sub>2</sub>O<sub>3</sub> to construct a high resolution 3D model of the template itself.

To summarize, one could consider using hard templating if the following conditions are met:

- The template should have the desired morphology
- The template should survive the target material deposition conditions
- If required, the template should be removable
  - The target material should survive the template removal processing conditions



### 3. MATERIALS AND METHODS

In this chapter a brief introduction to the material or method is given, after which the experimental details used in this work are described.

#### 3.1 Celluloses

Cellulose is one of the main constituents of plant biomass together with hemicellulose and lignin.<sup>50</sup> It is often said to be the most abundant renewable polymer on Earth.<sup>51</sup> In addition, cellulose is safe, non-toxic, non-petroleum based and bio-degradable therefore making it ideal material for modern products that should not pose any risk towards humans or environment.

Chemically cellulose is a linear chain polymer made of repeating glucose units. The chain is linked via covalent bonds through oxygen that joins two carbons of adjacent glucose units (i.e.  $\beta$  1  $\rightarrow$  4 glycosidic bond). The polymer chain is strengthened with hydrogen bonding between the hydroxyl groups and the oxygens in the cellulose ring. Typically the degree of polymerization is between 10000 – 15000.<sup>52</sup> The repeating unit of cellulose is presented in Figure 3.1a.

The cellulose polymer chains stack together via hydrogen bonding between neighboring chains (Figure 3.1b) forming fiber-like structures called nanofibrils. Furthermore, the nanofibrils stack together to form microfibrils. This construction is the main building block that gives green plants their structural stability.<sup>52</sup> The microfibrils can be up to several micrometers in length and 50 nm in thickness. The microfibrils separated into nanofibrils are the source for nanofibrillated cellulose (CNF). Figure 3.2 illustrates how the nanofibrils are obtained from the microfibrils. The nanofibrils contain crystalline and amorphous domains, therefore, upon removal of the amorphous regions cellulose nanocrystals (CNC) are obtained.<sup>53</sup> The CNCs are rod-like particles 100-200 nm in length and 5-20 nm in diameter, and the CNFs can be several micrometers long and around 5 nm in diameter.

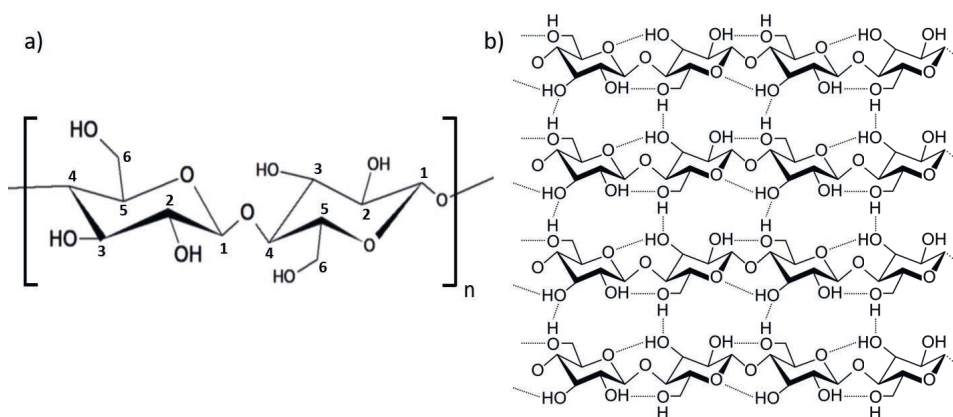


**Figure 3.1** a) Molecular structure of cellulose.<sup>52</sup> Carbons in the glucose rings are numbered to highlight position of the  $\beta$  1  $\rightarrow$  4 glycosidic bond. b) Strand of cellulose at the molecular level. The image shows how individual polymer chains group together via interchain hydrogen bonding to form the fibrils. The hydrogen bond is drawn with dashed line.

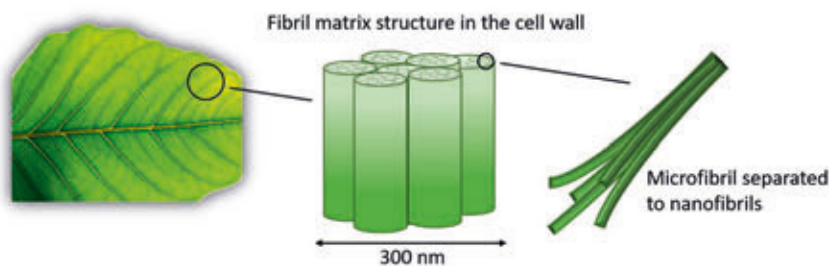


**Figure 3.2** a) An illustration of a cellulose microfibril and how it is made of a bundle of nanofibrils.

CNCs and CNFs can be used to make very lightweight and high surface area *aerogels*. Common preparation methods include freeze drying and critical point drying.<sup>51</sup> These nanostructured porous materials have found their way into multiple applications. CNC aerogels have been applied for example in superabsorbers (water or dodecane),<sup>54</sup> heat insulations,<sup>55</sup> and supercapacitors.<sup>56</sup> The literature on CNF applications is more extensive including use cases in humidity sensing,<sup>48</sup> batteries,<sup>57;58</sup> flexible supercaps,<sup>59</sup> hydrophobic coatings,<sup>60;61;62;63</sup> conductive substrates,<sup>64</sup> sound absorbers,<sup>65</sup> dye-sensitized solar cell electrolyte fillings,<sup>66</sup> and drug release.<sup>67</sup>

### 3.1.1 Cellulose film fabrication

#### Cellulose acetate films

Cellulose acetate (271 mg/ml) (CA-398-3 from Eastman) was dissolved in 1:5.64 (v/v) mixture of acetone and 1-methyl-2-pyrrolidinone. 5 mm wide stripe of solution was spread on a FTO substrate using the doctor blade technique (i.e. tape casting). Scotch Magic Tape 810 was used as the spacer. Immediately after spreading the whole substrate was dipped into a 1:4 (v/v) mixture of Milli-Q water and 1-methyl-2-pyrrolidinone for 3 s and then into Milli-Q water for 10 min. Then the films were dried in air at room temperature overnight. The excess of the film was cut out using a scalpel leaving a square ( $5 \times 5$  mm) of porous cellulose acetate in the middle of the substrate (Fig. 3.3a). The method was adapted from earlier work.<sup>68</sup>

These films were then placed in the ALD reactor for metal oxide deposition onto the cellulose (**Papers I & II**).

#### Cellulose nanocrystal films

Sulfate half-ester functionalized CNCs (sCNCs) were produced by hydrolyzing ashless cotton filter aid (Whatman, GE Healthcare Life Sciences, CAT No. 1703-050, Mississauga, Canada) in 64 wt% sulfuric acid.<sup>69</sup> The sCNCs were functionalized with aldehyde groups using a sodium periodate oxidation route as described in prior work resulting in aCNCs.<sup>70</sup> Hydrazine functionalized CNCs (hCNCs) were produced as described previously<sup>70</sup> by first oxidizing sCNCs with 2,2,6,6-tetramethyl-1-piperidinyloxy (TEMPO, Sigma-Aldrich). The resulting carboxyl groups on the CNCs were activated using N'-ethyl-N-(3-(dimethylamino)propyl)-carbodiimide and N-hydroxysuccinimide, then reacted with adipic acid dihydrazide to form hCNCs.

Aerogel films (1 wt% sol-gel concentration, 1:1 aCNC:hCNC weight ratio) were patterned onto FTO-coated glass (TEC-15, Pilkington, UK, sheet resistance 15 ohm/sq) substrates using a recently developed pressure-aided freeze casting technique. Briefly, FTO-coated glass was cleaned with Piranha solution (5:1 H<sub>2</sub>SO<sub>4</sub>:H<sub>2</sub>O<sub>2</sub> v/v) for 15 min at 110 °C to remove organic residue. A 7 µm-thick Parylene (Specialty Coating Systems, Indianapolis, IN, USA) film was deposited on the counter electrode and the film was patterned by xurography to create ( $5 \times 8$  mm) molds. It

should be noted that prior to Parylene deposition the substrate was spin coated with surfactant (1 % v/v, Micro-90, International Products Corp., Burlington, NJ, USA) to reduce Parylene-substrate adhesion. To ensure no interference with gel casting, the surfactant was washed from the substrate by bath sonication in water for 15 min. Pre-mixed aCNC:hCNC sol-gel suspensions were drop cast on the mold and immediately frozen at  $-30\text{ }^{\circ}\text{C}$  while under pressure. The frozen gel was lyophilized and the mold was subsequently lifted-off to reveal the aerogel of desired thickness and pattern.

These substrates were then placed in the ALD reactor for metal oxide deposition onto the cellulose (**Paper IV**).

## 3.2 Atomic layer deposition

In this work the cellulose templates were coated with a thin layer of  $\text{TiO}_2$  that were fabricated by the means of *atomic layer deposition* (ALD). Also all the other metal oxide thin films used in this work ( $\text{Fe}_2\text{O}_3$  &  $\text{Ta}_2\text{O}_5$ ) were fabricated using ALD.

Atomic layer deposition provides the means for depositing conformal coatings with ideally atomic scale control over the film thickness.<sup>71</sup> Typically the deposited film thickness is in the nanometer range. Thanks to the high quality of the ultrathin films fabricated by ALD, it has allowed the manufacture of ever smaller transistors and has therefore become a key technology in computers and smartphones. Intel Corporation took ALD into their production line already in 2007.<sup>72</sup>

ALD is based on repeated cycles. One cycle typically consists of four steps: 1) first precursor pulse, 2)  $\text{N}_2$  or Ar purge to remove excess precursor, 3) second precursor pulse, 4)  $\text{N}_2$  or Ar purge to remove excess precursor. This cycle is repeated until the desired film thickness is reached. Typically one cycle grows 0.01 - 0.3 nm of film.<sup>71</sup>

### 3.2.1 ALD methods used in this work

#### ALD of $\text{TiO}_2$

Throughout the work all depositions of  $\text{TiO}_2$  were done using Picosun Sunale ALD R200 Advanced reactor. Precursors used were TDMAT tetrakis(dimethylamido)titanium

(99 %, Strem Chemicals, Inc.) and deionized water. The purging gas was argon (99.9999 %, Oy AGA Ab). Pulsing times were 1.6 s for TDMAT, 0.1 s for  $\text{H}_2\text{O}$ , and 6 s for argon. Two different substrate temperatures were employed: for the cellulose acetate templates the substrate temperature during deposition was 100 °C (**Papers I,II**), and for the cellulose nanocrystal templates the substrate temperature was 200 °C (**Paper IV**).

Substrate temperature during deposition has an effect on the composition of the  $\text{TiO}_2$ , in particular on the  $\text{Ti}^{3+}/\text{Ti}^{4+}$  ratio. The  $\text{Ti}^{3+}$  defects lead to the dark appearance of the deposited ALD- $\text{TiO}_2$  layers (Fig. 3.3b).<sup>73</sup>

### ALD of $\text{Fe}_2\text{O}_3$

The  $\text{Fe}_2\text{O}_3$  thin films were deposited using a F-120 ALD reactor (ASM Microchemistry, Finland) using a  $\text{FeCl}_3/\text{H}_2\text{O}$  process at 400 °C.<sup>74</sup> When deposited on the cellulose acetate templated porous  $\text{TiO}_2$  (**Paper II**) pulsing times for  $\text{FeCl}_3$  and  $\text{H}_2\text{O}$  were 2 s with 8 s purging after each reactant (Fig. 3.3d).

### ALD of $\text{Ta}_2\text{O}_5$

The  $\text{Ta}_2\text{O}_5$  thin films were deposited using a  $\text{Ta}(\text{OC}_2\text{H}_5)_5/\text{H}_2\text{O}$  deposition process at 300 °C. The pulsing times were 0.8 s for  $\text{Ta}(\text{OC}_2\text{H}_5)_5$  and 1.0 s for  $\text{H}_2\text{O}$  with 2.0 s purging (**Paper III**).

## 3.3 Device assembly

### Solar cells

The dye-sensitized solar cells were assembled according to previous publication<sup>75</sup> apart from the porous  $\text{TiO}_2$  fabrication. The porous cellulose acetate films coated with ALD- $\text{TiO}_2$  were dipped into an acetone bath to detach the film from the substrate and to wash away the excess cellulose acetate. The floating ALD- $\text{TiO}_2$  film was transferred onto a new clean FTO substrate in the bath and subsequently calcined at 450 °C for an hour (Fig. 3.3c).

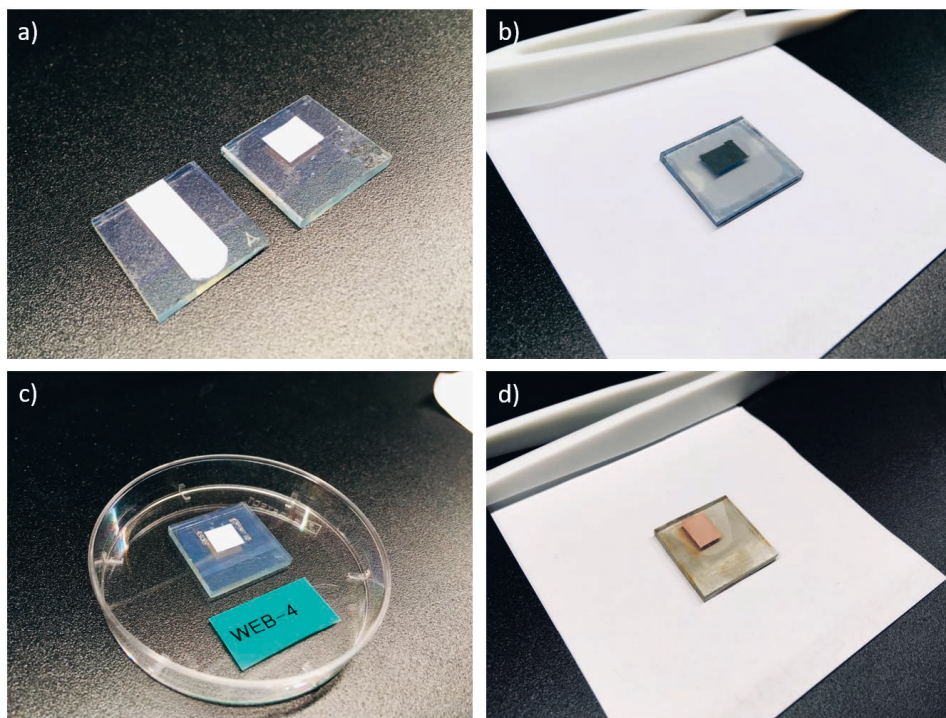


**Figure 3.3** Photographs of the films during different stages of fabrication. a) Cutting of cellulose acetate template, b) cellulose template after ALD of  $\text{TiO}_2$ , c) ALD- $\text{TiO}_2$  after calcination, d)  $\text{TiO}_2$  web coated with ALD- $\text{Fe}_2\text{O}_3$ .

The  $\text{TiO}_2$  was then stained in a 0.1 mM N719 (Ruthenizer 535-bisTBA from Solaronix) solution of acetonitrile:*tert*-butanol 1:1 (v/v) for 16 h. Platinum catalyzed counter electrode was prepared by depositing a drop of 5 mM  $\text{H}_2\text{PtCl}_6$  in EtOH on another FTO substrate and annealed at 450 °C for 15 min. The  $\text{TiO}_2$  electrode and the counter electrode were glued together using a 25  $\mu\text{m}$  thick hotmelt (from Solaronix) plastic such that it made a frame around the  $\text{TiO}_2$  film. Electrolyte was injected into the cavity inside the frame in between the glass substrates through a hole drilled into the platinum counter electrode. To make filling easier two holes were drilled so that air could escape through the second hole. The electrolyte was 0.6 mM 1,3-dimethyl-imidazolium iodide, 0.03 mM diiodine, 0.1 mM guanide thiocyanate, and 0.5 mM 4-*tert*-butylpyridine in a 85:15 (v/v) mixture of acetonitrile and valeronitrile. After filling, both holes were capped with a piece of microscope glass using the hotmelt film.

### Water splitting

The ALD-TiO<sub>2</sub> coated cellulose acetate films were transferred (similarly as described above for solar cells) onto FTO substrates that had a spin coated compact TiO<sub>2</sub> layer.<sup>76</sup> The films were then annealed at 450 °C (heating rate 7 °C/min) for 45 min, and cooled down slowly with the same rate. Additional ALD-Fe<sub>2</sub>O<sub>3</sub> layer was deposited onto these films according to method described above. These films were still subject to one more thermal treatment at 680 °C for an hour (heating rate 20 °C/min). After the hour the samples were removed from the hot oven to room temperature and let cool down.

The ALD-TiO<sub>2</sub> coated cellulose nanocrystal films were annealed at 500 °C (heating rate 20 °C/min) for an hour, and cooled down using the same rate.

Prior to photocurrent measurement, excess of the substrates were insulated using Kapton tape leaving only the templated ALD-TiO<sub>2</sub> structure exposed. These samples were then tested as photoanodes in an electrochemical cell.

## 3.4 Photovoltaic characterization

### Solar cells

The figures of merit ( $PCE$ ,  $I_{sc}$ ,  $V_{oc}$ ,  $FF$ ) for the dye-sensitized solar cells were determined from  $IV$ -curves measured with a Agilent E5272A source measurement unit in 4 wire setup under 1 Sun illumination. The light source was a 450 W Xe lamp with a  $\lambda = 315 - 710$  nm bandpass filter (KG3 from Schott) in front of the cells. The intensity was set to 1 Sun (100 mW/cm<sup>2</sup>) using a certified reference silicon solar cell from Oriel Instruments (model 91150V).

### Solar water splitting

The  $IV$ -curves for solar water splitting were measured in a 3-electrode setup where the sample was the working electrode, platinum wire the counter electrode and aqueous Ag/AgCl (sat. KCl) the reference electrode. Electrolyte was 0.1 M NaOH solution contained in a 5 × 1 cm quartz cuvette (Figure 2.6).  $IV$ -curves were recorded with Agilent E5272A source measurement unit under 1 Sun illumination.

The light source was 150 W Xe-lamp (Sciencetech SS150 - AAA Solar simulator) equipped with an AM1.5G filter. The intensity was set to 1 Sun using the certified reference silicon solar cell from Oriel Instruments (model 91150V). In Figures 4.8 and 4.11 the Ag/AgCl electrode potential is reported against the reversible hydrogen electrode (V vs. RHE). Conversion was done according to formula  $V_{\text{RHE}} = V_{\text{bias}} + 0.05916 \cdot \text{pH} + 0.197 \text{ V}$ .



## 4. RESULTS AND DISCUSSIONS

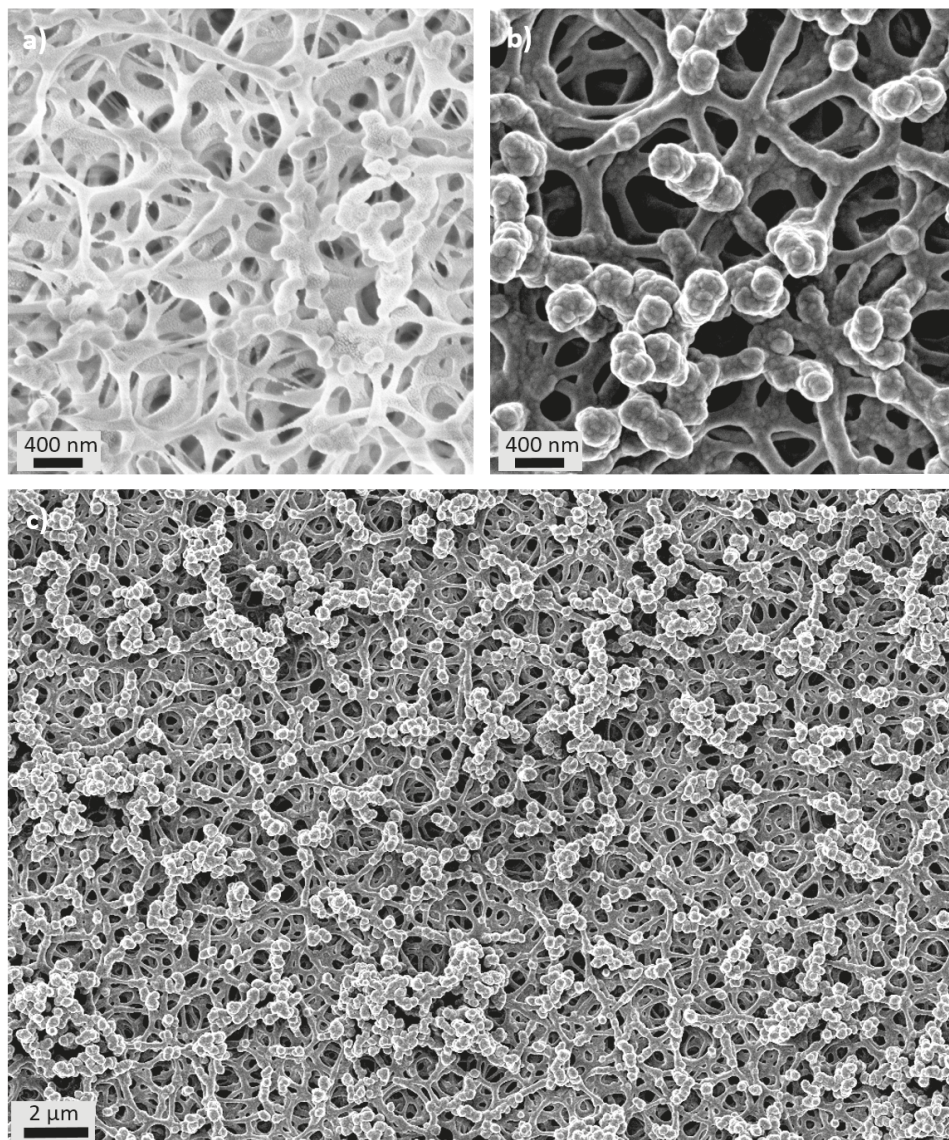
In this chapter we first focus on the structural characteristics of the cellulose templated metal oxide films and then look at their potential applications in photovoltaic devices.

### 4.1 Cellulose templating for ALD of metaloxides

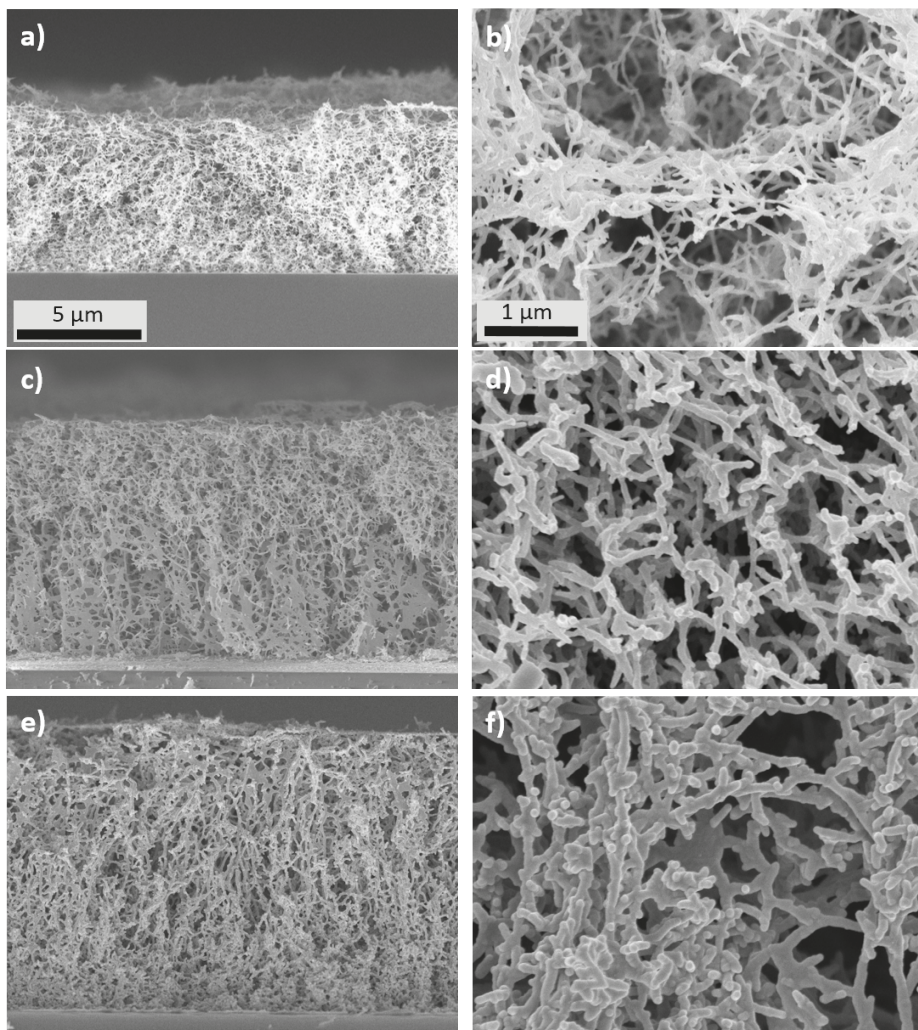
The objective of this work was to use cellulose acetate (CA) and later cellulose nanocrystal (CNC) templates to fabricate porous metal oxide thin films by the means of ALD. Cellulose acetate was selected as a starting point because it is commercially readily available and can be cast to porous films according to a facile method<sup>77</sup> which was adapted from earlier literature.<sup>68</sup>

Figure 4.1 shows characteristic SEM images of the porous cellulose acetate films before and after the ALD-TiO<sub>2</sub> coating. Comparison of Figures 4.1a and 4.1b shows that the ALD coating preserves the weblike structure of the template. The diameter of the openings in the web vary largely from 100 to 1000 nm, as well as the string diameter varies from 100 to 400 nm. The variations are caused by the variations in the cellulose template, and thus are not caused by the ALD process. The ALD coating thickness on top of the film is exactly 30 nm targeted with 480 cycles of TDMAT/H<sub>2</sub>O-process at 100 °C. However towards the bottom of the film the coating thickness decreases from the target value due to limited diffusion of the ALD precursors through the porous structure. This issue is further discussed in Section 4.1.3. Altogether, cellulose acetate was found to be suitable for the fabrication of porous TiO<sub>2</sub> thin films by means of ALD-templating.

Cellulose nanocrystal films were also studied as potential template materials in addition to cellulose acetate films. Figure 4.2 shows SEM images of CNC films coated with 145, 435, and 870 cycles of TDMAT/H<sub>2</sub>O-process at 200 °C that nominally corresponded to 5, 15 and 30 nm of TiO<sub>2</sub> layer thickness. Similarly to CA templates,



**Figure 4.1** a) SEM image of a cellulose acetate template (with thin layer of silver to facilitate the imaging), b) the template coated with 30 nm of ALD-TiO<sub>2</sub>, c) a larger image of the TiO<sub>2</sub> coated web.



**Figure 4.2** On left column cross sectional SEM images of 145, 435 nm and 870 nm ALD-TiO<sub>2</sub> coatings on cellulose templates, and on right column images from top of the films.

the structure of the CNC template could be replicated with the ALD-TiO<sub>2</sub> coating to a fine degree. In contrast to CA films, it was possible to coat the CNC films thoroughly from top to bottom with uniform coating thickness. We expect this to be enabled by the extremely low density of the CNC aerogel templates that allows more free diffusion of the ALD precursor gases into the film.



### 4.1.1 Calcining

Upon deposition, the ALD-TiO<sub>2</sub> coatings are amorphous.<sup>73</sup> Because in this work the films were applied in photovoltaic devices, the films were calcined to crystallize the TiO<sub>2</sub> which simultaneously lead to removal of the cellulose template from the structure. Typical temperature was 450 - 500 °C and calcination time 1 h. Calcining didn't create any changes to film's appearance which could have been observed by means of SEM or by eye. XRD measurements proved successful crystallization to anatase and XPS revealed slightly increased carbon contamination levels due to burning of cellulose.<sup>77</sup>

### 4.1.2 Early stage film growth & thinnest coatings

Often opto- and nanoelectronic, medical, and catalytic properties are highly dependent on the structure morphology. Therefore, the development of increasingly competent devices requires techniques which are not limited by the shortcomings of the fabrication methods. Instead, new technology should allow vast possibilities for fine tuning and optimization. While the combining of ALD and cellulose templating has previously been demonstrated in literature, only a limited range of coating thicknesses has been explored. Moreover, the question of sufficient metal oxide layer thickness to form a self standing structure after cellulose template removal remained unanswered prior to this work.

To address this question, a broad range of TiO<sub>2</sub> coating thicknesses were studied starting from a common literature benchmark<sup>45;77;78</sup> of 30 nm down to the collapse point of the structure upon template removal. The template was 10 µm thick CNC aerogel. The thinnest self-standing structure fabricated by us had only 87 ALD-TiO<sub>2</sub> cycles that equaled 7 nm coating thickness (see Figure 4.3 for SEM images). TEM images together with close-up SEM images (Figures 4.4a,b) revealed that the structure is remarkably held together by weakly connected TiO<sub>2</sub> crystallites which do not yet form a closed film on the surface. Hence, the structures fabricated this way form a high surface area TiO<sub>2</sub> aerogel where the strings of the weblike structure themselves are porous. To the best of our knowledge, this cellulose templated 3D self-standing structure has the thinnest wall thickness so far reported. Eventually, after 290 cycles (10 nm) the crystallites emerge to form a conformal smooth surface (Figure 4.4c).

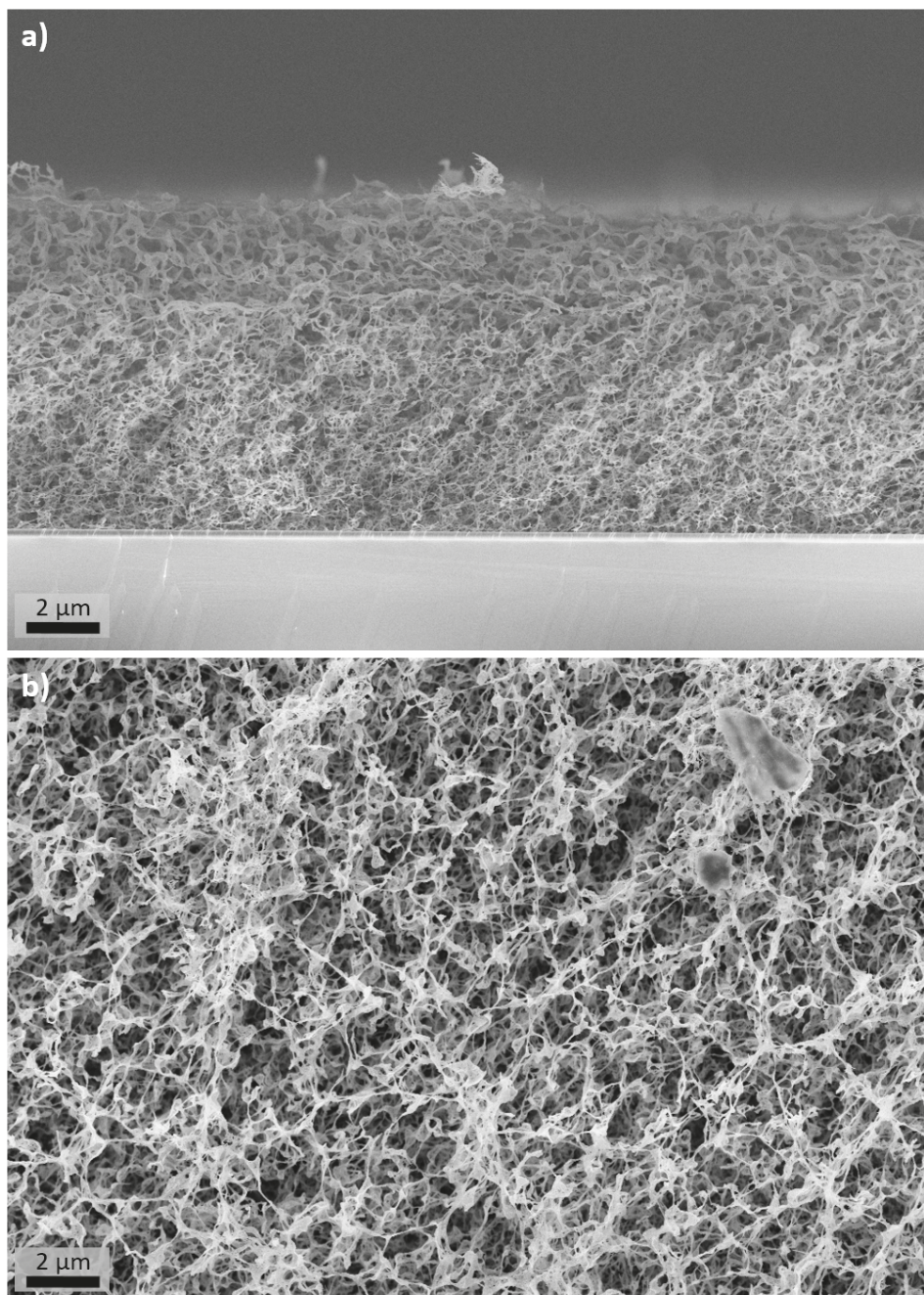


**Figure 4.3** SEM images of the  $\text{TiO}_2$  structures with the thinnest coating thickness (87 cycles/7 nm, calcined). a) Cross section, b) imaged from top.

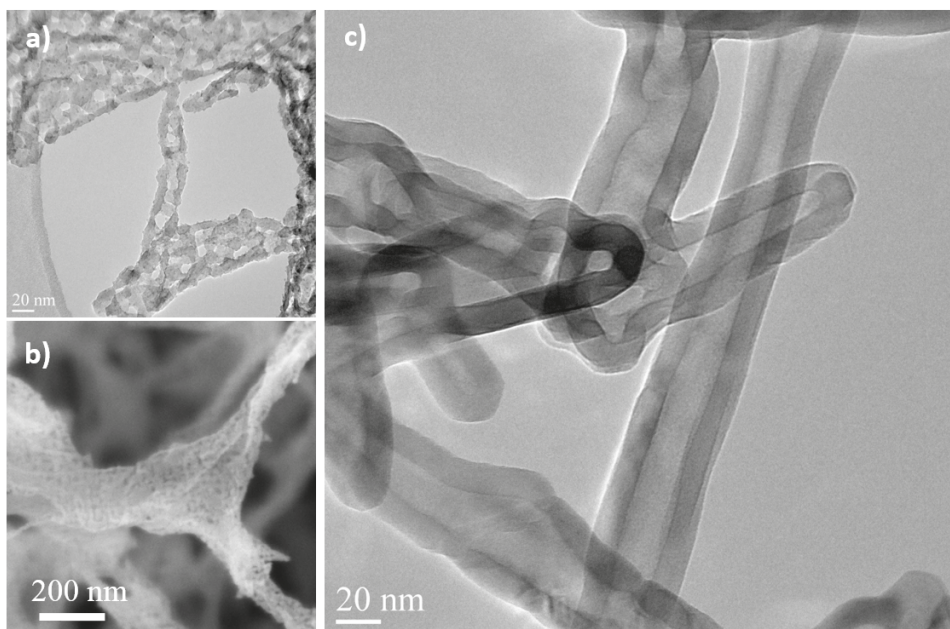


**Figure 4.4** a) TEM image of a templated structure having the thinnest ALD- $\text{TiO}_2$  coating (87 cycles, 7 nm, calcined), b) corresponding SEM image, c) TEM image of a templated  $\text{TiO}_2$  structure with increased number of coating cycles (290 cycles, 11 nm, calcined).

Above we used the term nominal coating thickness because the measured (from TEM images) value differed from the calculated value in the case of the thinnest coatings due to the crystallite formation that precedes the conformal film growth. In our case we found following relation between the number of cycles and actual measured film thickness: 87 cycles (nominal 3.0 nm) equaled  $7.2 \pm 2$  nm, 145 cycles (nominal 5.0 nm) equaled  $7.2 \pm 2$  nm, 290 cycles (nominal 10.0 nm) equaled  $11.4 \pm 1$  nm. After the 290 cycles the growth rate settled to a constant value 0.034 nm/cycle.

### 4.1.3 Fabrication of transferable thin films

Requirement for the template based methods is that the template and the template processing are compatible with the substrate of the end-application. Obviously, this might not always be the case for example due to solvent- or thermal resistance issues or due to excess mechanical stress during processing. Therefore it might be advantageous to be able to transfer the pre-processed templated films from one



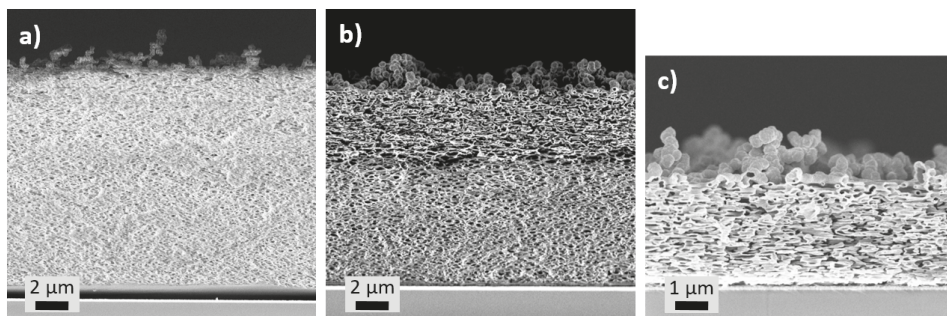


**Figure 4.5** SEM images describing the transferable web preparation. a) Cellulose template, b) coating of the top part of the template with ALD- $\text{TiO}_2$ , c) dissolution of cellulose acetate, and subsequent calcination leaves behind only the porous  $\text{TiO}_2$ .

substrate to another: from the fabrication substrate to that of the end-application.

Transferability was achieved using the observation that the ALD precursor gases weren't able to penetrate all the way through the CA template due to limited diffusion within the pores of cellulose acetate. Using the selected processing parameters the ALD coating thickness remained constant down to  $3.5\ \mu\text{m}$  from the surface towards the bottom but then gradually decreased to zero during the last  $500\ \text{nm}$  leaving behind a layer of uncoated cellulose acetate between the coated film and the substrate (see Figure 4.5b).

We discovered that it was possible to dissolve the uncoated cellulose acetate in an acetone bath that lead to detachment of the film from the processing substrate. The floating film could now be transferred onto a new substrate in the same bath. Because the  $\text{TiO}_2$  films are amorphous after the ALD deposition they possess flexibility that enabled the transfer even onto curved substrates as demonstrated in Figure 4.6.

## 4.2 Photovoltaic applications of the templated photoanodes

### 4.2.1 Dye-sensitized solar cells

Templating methods have been used in dye-sensitized solar cell technology in order to overcome the limitations imposed by the nanoparticle  $\text{TiO}_2$  electrode. While the nanoparticles provide a high surface area for dye absorption the electron transport



**Figure 4.6** A  $\text{TiO}_2$ -web transferred on a curved surface. Diameter of the glass rod is 6 mm.

through the nanoparticle electrode is hindered due to trapping within the particles and at grain boundaries.<sup>23;24</sup>

Taking advantage of the conformal coatings enabled by ALD, Hamann et al.<sup>79</sup> and Chandiran et al.<sup>80</sup> coated a nanoparticle  $\text{SiO}_2$  template with ALD- $\text{TiO}_2$  to transport the electrons along the ALD- $\text{TiO}_2$  coating therefore enabling the charges to travel around the nanoparticles rather than through them. Martinson et al. considered ITO nanotube templates coated with ALD- $\text{TiO}_2$  to shorten the electron transport pathway to the collector.<sup>81</sup>

In contrast to the inorganic templates also organic templates, namely cellulose, have been examined as alternatives to the traditional nanoparticle electrode. Ghadiri et al.<sup>82</sup> mixed cotton fibers with  $\text{NH}_4\text{TiF}_6$  and  $\text{H}_3\text{BO}_3$ , to obtain cellulose templated  $\text{TiO}_2$  fibers upon calcination. These fibers were subsequently crushed and formulated to a paste that could be used to cast a  $\text{TiO}_2$  electrode for a DSSC. Ivanova et al.<sup>83</sup> elaborated on this approach mixing titanium ethoxide with cellulose nanocrystals which could be directly cast into films and transformed into templated  $\text{TiO}_2$  upon



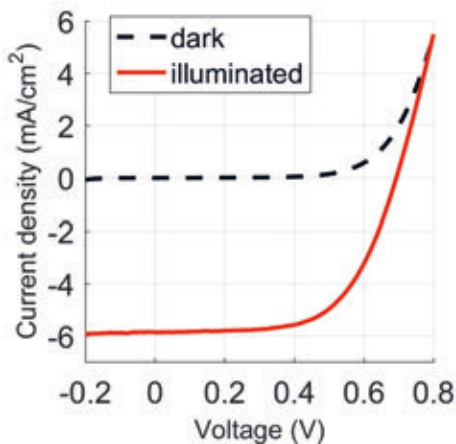


**Figure 4.7** A representative IV-curve of a DSSC prepared using the  $\text{TiO}_2$  web.

calcination. In this thesis, we replaced the wet chemistry routes with atomic layer deposition to obtain cellulose templated  $\text{TiO}_2$  photoanodes for DSSCs.

The cellulose acetate templated  $\text{TiO}_2$  films (as in Figure 4.1) were used as photoanodes in dye-sensitized solar cells to replace the common nanoparticle based  $\text{TiO}_2$  electrode. Using  $\text{I}^-/\text{I}_3^-$  redox couple and the dye N719 we obtained *PCE* of  $2.8 \pm 0.3 \%$ , *FF* of  $65 \pm 2 \%$ ,  $V_{oc}$  of  $0.69 \pm 0.01 \text{ V}$ , and  $I_{sc}$  of  $6.2 \pm 0.4 \text{ mA/cm}^2$  (see IV-curve in Fig. 4.7) at 1 Sun illumination. The main limiting factor for reaching high performance was the low current density caused by small amount of dye absorbed; color of the  $\text{TiO}_2$  after dyeing was light red in contrast to deep red color of the nanoparticle electrode. Albeit the pore size in the cellulose acetate network is measured in nanometers (100-500 nm) the state-of-the-art nanoparticle electrodes provide roughly 10 times more surface for the dye absorption resulting in higher current densities. This limitation could be overcome by replacing the cellulose acetate template with the latest cellulose nanocrystal aerogels having porosity up to  $190\text{-}320 \text{ m}^2/\text{g}$ .<sup>54;84</sup>

#### 4.2.2 Photoanodes for water splitting

All the cellulose templated ALD- $\text{TiO}_2$  photoanodes developed in the course of this thesis (i.e. the CA-templated & CNC-templated) were both tested in water splitting application. To the best of our knowledge **Papers II & IV** are the first demonstra-

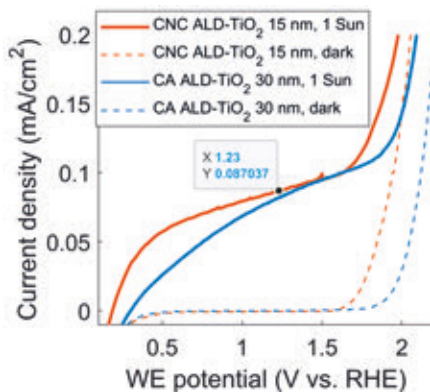


**Figure 4.8** Comparison of CA-templated vs. CNC-templated webs in solar water splitting (1 Sun, 0.1 M NaOH)

tions of using cellulose acetate or cellulose nanocrystals as templates for ALD-TiO<sub>2</sub> in water splitting application. Performance of the two templates under 1 Sun illumination in 0.1 M NaOH is compared side by side in Figure 4.8. Their performance is very similar giving 90  $\mu\text{A}/\text{cm}^2$  for the CNC-templated and 80  $\mu\text{A}/\text{cm}^2$  for the CA-templated at 1.23 V vs. RHE. However the current onset is clearly more sharp for the CNC-templated indicating more ideal photoanode 3D web structure and improved charge transport within the film. Furthermore, we were able to show that the coating thickness could be brought down from the current literature benchmark of 30 nm<sup>77;78</sup> down to 15 nm without losses in efficiency resulting in materials and time savings.

#### Visible light sensitization of CA-templated ALD-TiO<sub>2</sub> by ALD-Fe<sub>2</sub>O<sub>3</sub>

TiO<sub>2</sub> is a wide band gap semiconductor and therefore absorbs only UV-light. Extending the light absorption to visible with an additional coating — similarly as in dye-sensitized solar cells — was first demonstrated by Sivula et al.<sup>33</sup> calling it the scaffold-absorber concept. However, organic dyes degrade quickly during the oxidation reaction<sup>85</sup> therefore inorganic sensitizers have been proposed instead. One of the candidates is hematite ( $\alpha\text{-Fe}_2\text{O}_3$ ) since it has a band gap of 2 eV making it a promising choice for the application.<sup>86</sup> The problem in using hematite together with TiO<sub>2</sub> is the unfavorable band alignment for charge injection from hematite to TiO<sub>2</sub>.<sup>32</sup> Despite the obvious challenge multiple efforts have been made to combine

TiO<sub>2</sub> together with hematite<sup>87</sup> but the reports so far have been inconsistent.<sup>88;89;90</sup> Therefore, further clarification on the topic had been requested.<sup>87</sup>

Having the possibility to prepare iron oxide layers with ultrahigh precision using ALD, we fabricated ALD-Fe<sub>2</sub>O<sub>3</sub> coatings on the CA-templated TiO<sub>2</sub> to study the suitability of the TiO<sub>2</sub>-Fe<sub>2</sub>O<sub>3</sub> pair in a scaffold-absorber configuration. The deposited ALD-Fe<sub>2</sub>O<sub>3</sub> amounts were 100, 200 and 400 cycles corresponding nominally to 5, 10 and 20 nm thicknesses. The SEM images in Figure 4.9 reveal that the iron oxide grew on the TiO<sub>2</sub> scaffold as small crystallites which eventually coalesced together when 400 cycles were applied. Large view images (Fig. 4.10) show that the coatings were uniform throughout the films.

In the as-deposited condition no water oxidation was observed from the ALD-TiO<sub>2</sub>-Fe<sub>2</sub>O<sub>3</sub> photoanodes under illumination (see Figure 4.11a). However, upon annealing at 680 °C water oxidation was enabled (Figure 4.11b). Moreover, an improvement in the photocurrent over bare TiO<sub>2</sub> was obtained at 1.23 V vs. RHE and higher bias voltages. Interestingly, the enhancement was obtained with the thinner coatings (100 and 200 cycles) but not with the thickest coating (400 cycles). IPCE spectrum (Fig. 4.12) revealed that the ALD-Fe<sub>2</sub>O<sub>3</sub> coating indeed extended the photocurrent response range from UV to  $\lambda = 600$  nm confirming the hypothesis that the onset of photocurrent generation of TiO<sub>2</sub> scaffold could be extended to longer wavelengths using an ALD-Fe<sub>2</sub>O<sub>3</sub> absorber.

On the basis of Raman and XPS spectroscopy the reason for the broader wavelength range for photocurrent generation was found to be the formation of Fe(III)Ti(IV)-oxide on the surface of the TiO<sub>2</sub> scaffold upon annealing. The exact composition of the formed oxide could not be resolved in this study possibly because of it existing as a very thin layer on the scaffold surface. Further evidence on formation of a new oxide on the surface is given by the change of the photocurrent onset in function of WE potential (Figure 4.11b) when compared to the bare TiO<sub>2</sub> photoanode; the onset for bare TiO<sub>2</sub> is at 0.3 V vs. RHE while for the iron oxide coated TiO<sub>2</sub> the onset is at 1.0 V vs. RHE. The *IV*-curves measured with 100 and 200 cycles coatings bare close resemblance to those measured with Ti-doped hematite photoanodes.<sup>91;92;93</sup>

Furthermore, when 400 cycles were deposited a clear signal from hematite was observed with Raman and XRD.<sup>94</sup> Due to the unfavorable band alignment with TiO<sub>2</sub>, the hematite layer formed an injection barrier which explains the decreased performance compared to the 100 and 200 cycles coatings where no clear signal from

hematite was detected.

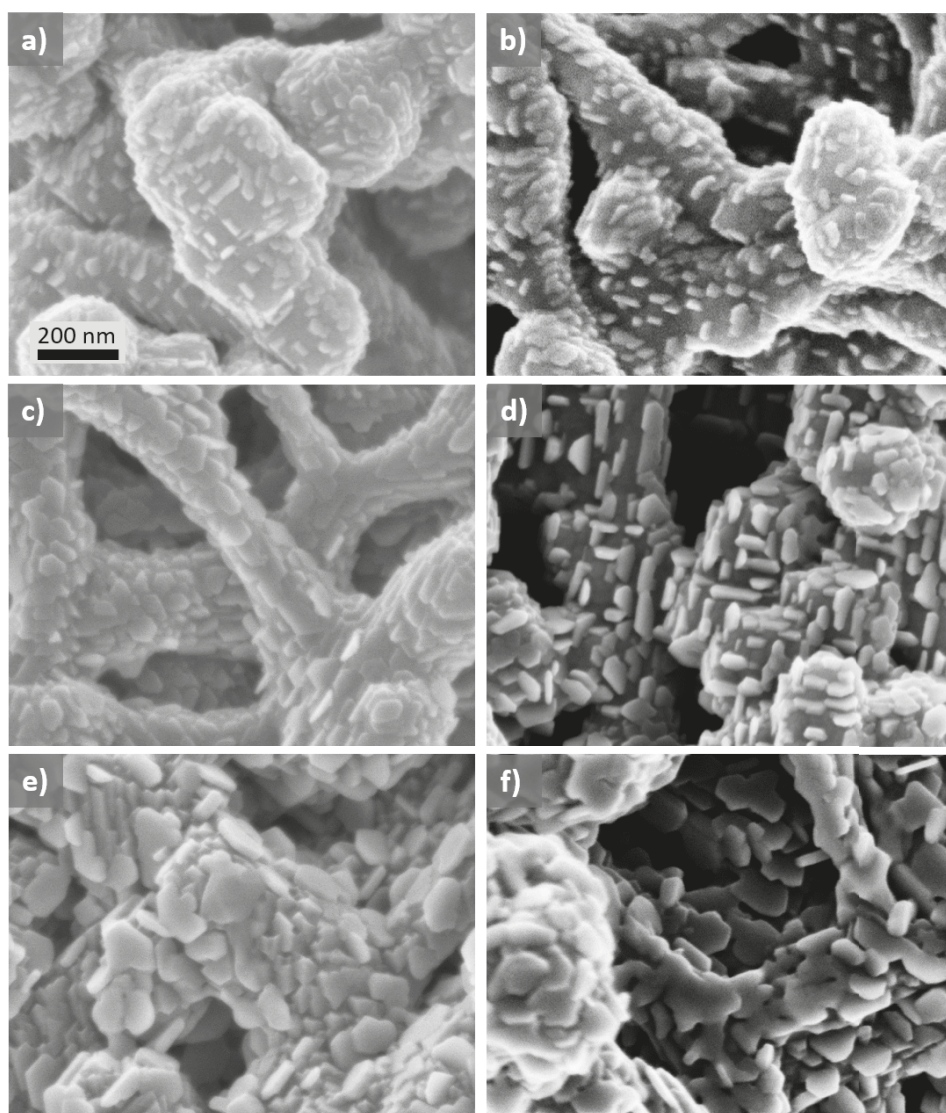


**Figure 4.9** SEM images of CA-templated ALD-TiO<sub>2</sub> webs having a (a,b) 100, (a,d) 200 or (e,f) 400 cycles ALD-Fe<sub>2</sub>O<sub>3</sub> coating applied to scaffold-absorber concept. Left column as-deposited, right column annealed.



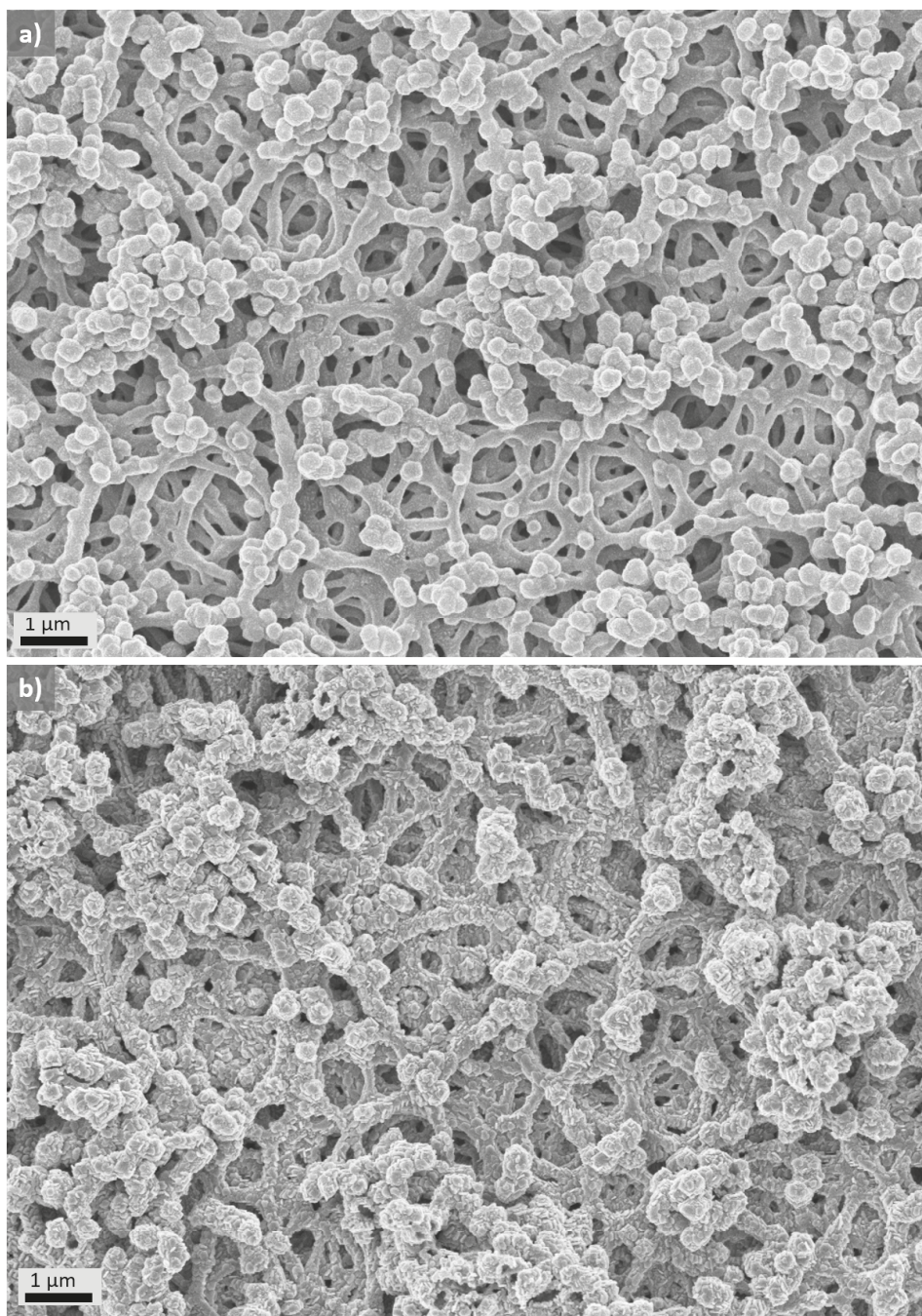


**Figure 4.10** Larger view on the  $\text{TiO}_2\text{-Fe}_2\text{O}_3$  scaffold-absorber photoanodes. a) 100 cycles, b) 400 cycles (annealed).

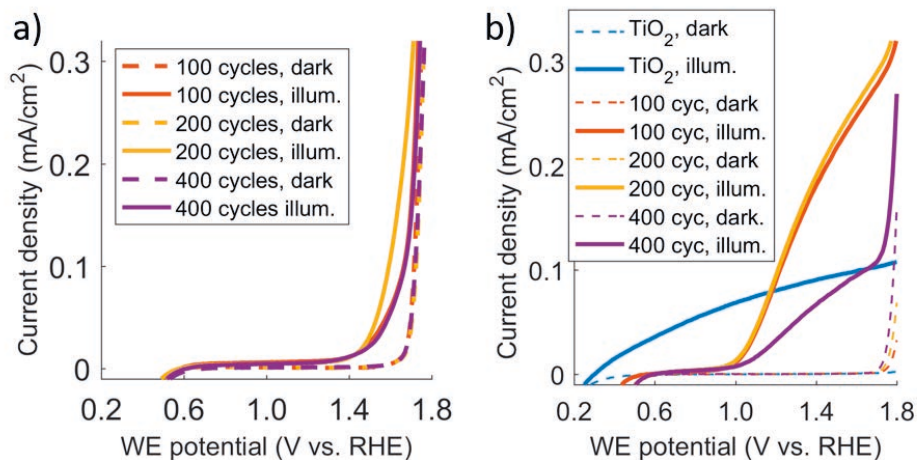


**Figure 4.11** a) IV-curves of  $\text{TiO}_2$  webs coated with  $X$  cycles of  $\text{ALD-Fe}_2\text{O}_3$  a) before and b) after annealing.

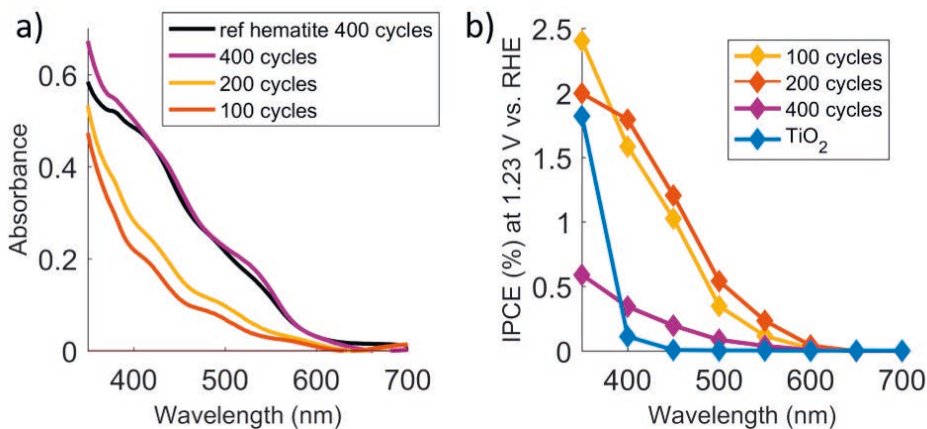


**Figure 4.12** a) Absorption spectra of annealed thin films:  $\text{glass/FTO/ALD-TiO}_2(30 \text{ nm})/\text{ALD-Fe}_2\text{O}_3(X \text{ cycles})$ , and the spectrum of hematite reference:  $\text{glass/FTO/ALD-Fe}_2\text{O}_3(400 \text{ cycles})$ . All films were annealed at  $680^\circ\text{C}$ . b) IPCE spectra of annealed  $\text{TiO}_2$  webs coated with  $X$  cycles of  $\text{ALD-Fe}_2\text{O}_3$ .

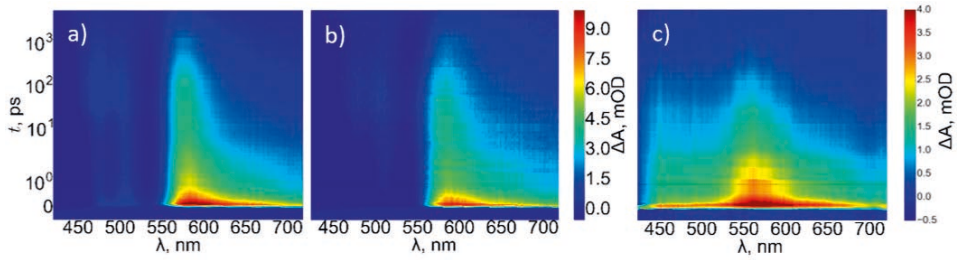


**Figure 4.13** Transient absorption spectra of a) reference hematite film, b) Ta-doped hematite film, c) FeTiO film.

### Photochemistry of ALD-Fe<sub>2</sub>O<sub>3</sub>

Photoelectrochemical reactions of the material compositions that constitute the templated structures were studied using transient absorption techniques. Transient absorption spectroscopy in the ps-ns timescale (in particular the pump-probe technique) provides information on the lifetimes of the excited states following the laser excitation and the following recombination and charge transfer processes.

The strong positive absorption band centered at 575 nm (see Fig. 4.13) has been assigned to the absorption of photoexcited electrons<sup>95</sup> in the hematite conduction band. When doped with tantalum the spectrum bears high resemblance to that of the reference hematite. However, when combined with titanium clear differences in spectra were observed. A new broad absorption band formed at 450–680 nm which we interpreted as charge transfer to TiO<sub>2</sub>. Furthermore, bleach observed for the bare hematite and the Ta-doped hematite, is not visible for the ALD-Fe<sub>2</sub>O<sub>3</sub>-TiO<sub>2</sub> sample which signifies clearly different charge transfer dynamics. The observation that the difference occurred immediately after the excitation was taken as further evidence of mixing of the TiO<sub>2</sub> and the Fe<sub>2</sub>O<sub>3</sub> layers creating a FeTi-compound on the surface as discussed above.

## 5. SUMMARY AND FUTURE OUTLOOK

This work looked into the photovoltaic applications of porous  $\text{TiO}_2$  films that were fabricated by the means of cellulose templating and atomic layer deposition (ALD). Studied cellulose templates were made of cellulose acetate or cellulose nanocrystal (CNC) aerogels that were then coated with ALD of  $\text{TiO}_2$ . Additional  $\text{Fe}_2\text{O}_3$  coating on top of the  $\text{TiO}_2$  was also implemented. The cellulose nanocrystal templated films were tested as photoanodes for solar water splitting while cellulose acetate templated ALD- $\text{TiO}_2$  films were tested in dye-sensitized solar cells as well. The main findings are summarized in the following paragraphs.

Cellulose aerogels are versatile template materials. They can be modified in shape, structure of the aerogel pattern, thickness, density and porosity. When combined with atomic layer deposition, these properties can be replicated in the deposited metal oxide to the finest degree in addition to having nanometer precision in the coating thickness. Cellulose aerogel templating opens a new diverse library of structures for applications that require porous metal oxides.

This thesis describes a method for fabrication of transferable cellulose acetate films. Transferability function was achieved by coating the porous substrate halfway such that the metal oxide coating layer did not form any contact with the supporting substrate. This allowed the dissolution of the remaining template that resulted in detachment of the ALD-coated film which could then be transferred to a new substrate. The advantage of this approach is that the transferred film can adopt the shape of the new support which can for example be curved. These films showed good initial performance when tested in dye-sensitized solar cell photoanodes. This work also served as the first demonstration of cellulose acetate templated ALD- $\text{TiO}_2$  photoanode applied to DSSCs.

Cellulose nanocrystal templates coated with different thicknesses of ALD- $\text{TiO}_2$  were tested in water splitting application. Highest performance was observed for 15 nm  $\text{TiO}_2$  coating that is significantly thinner than the commonly used literature bench-



mark of 30 nm. Increased performance, combined with reduced fabrication time and materials savings substantially reduces the price of the produced solar hydrogen.

In the course of coating thickness optimization we looked into the mechanical properties of the fabricated porous  $\text{TiO}_2$  networks. 10 micrometer thick CNC aerogel ALD- $\text{TiO}_2$  replica was found to be self supporting at 7 nm coating thickness. Thinner ALD-coatings resulted in the collapse of the structure. In addition, systematic study of different coating thicknesses revealed the growth mode of the ALD- $\text{TiO}_2$  on the CNC template. The growth begins as weakly connected crystallites that eventually coalesce together to make a smooth film once the coating thickness reaches 10 nm.

Additional ALD coating on top of the  $\text{TiO}_2$  was tested in order to increase the light absorption of the photoanode to visible range. Application of 100 or 200 cycles of ALD- $\text{Fe}_2\text{O}_3$  over the  $\text{TiO}_2$  extended the effective spectrum range to red, from 400 to 600 nm, resulting in increased overall photocurrent under 1 Sun illumination. The key enabler for the enhanced performance was found to be the formation of iron titanium oxides on the surface.

Further evidence on the role of iron mixed into the  $\text{TiO}_2$  was explored by the means of ultrafast transient absorption spectroscopy.  $\text{Ti-Fe}_2\text{O}_3$  ALD-films were compared against tantalum  $\text{Ta-Fe}_2\text{O}_3$  films. Obtained data supports the formation of new iron titanium oxides upon mixing of the ALD- $\text{Fe}_2\text{O}_3$  and ALD- $\text{TiO}_2$  layers while on the other hand no evidence of tantalum iron oxides was observed.

## Future outlook

The methods developed during the course of this work clearly demonstrate the possibility to use cellulose templating together with atomic layer deposition to fabricate 3D photoactive materials for solar cells or for solar water splitting. We propose that the fibrous framework of the cellulose based templates could be further customized to be more application specific. Tailored aerogel porosity optimized for light harvesting and charge transport could result in increased DSSC and solar water splitting performance over that what is reported here. For DSSCs the  $\text{TiO}_2$  replica of the CNC aerogel template has the potential to solve the problems related to the charge transport across the currently employed nanoparticle electrode. Similarly, in particular for hematite based solar water splitting, the aerogel structures could provide

close proximity of the water interface solving the problems related to the short hole diffusion length related problems. However, this would require development of low temperature ALD recipes for hematite growth in order to deposit the hematite directly on the cellulose aerogel. On a final note, owing to the high precision of ALD and the structural diversity of cellulose based aerogels, we expect this combination to enable the fabrication of high performance materials for various applications in the field of nanoscience especially in energy harvesting, energy storage, and catalysis.

## REFERENCES

- [1] V. Masson-Delmotte, P. Zhai, H.-O. Pörtner, D. Roberts, J. Skea, P.R. Shukla, A. Pirani, W. Moufouma-Okia, C. Pean, R. Pidcock, S. Connors, J.B.R. Matthews, Y. Chen, X. Zhou, M.I. Gomis, E. Lonnoy, T. Maycock, M. Tignor, and T. Waterfield (eds.). IPCC, 2018: Summary for Policymakers. Global Warming of 1.5 °C. An IPCC Special Report on the impacts of global warming of 1.5 °C above pre-industrial levels and related global greenhouse gas emission pathways, in the context of strengthening the global response to the threat of climate change, sustainable development, and efforts to eradicate poverty. *World Meteorological Organization, Geneva, Switzerland*, 2018.
- [2] Robert B. Schmunk. *NASA's Scientific Visualization Studio (NASA/GSFC GISS)*, 2018.
- [3] Matthew W. Kanan and Daniel G. Nocera. In situ formation of an oxygen-evolving catalyst in neutral water containing phosphate and  $\text{Co}^{2+}$ . *Science*, 321:1072–1075, 2008.
- [4] NREL. Reference air mass 1.5 spectra. <https://www.nrel.gov/grid/solar-resource/spectra-am1.5.html>.
- [5] Sven Rühle. Tabulated values of the shockley–queisser limit for single junction solar cells. *Solar Energy*, 130:139–147, 2016.
- [6] Albert Polman, Mark Knight, Erik C. Garnett, Bruno Ehrler, and Wim C. Sinke. Photovoltaic materials: Present efficiencies and future challenges. *Science*, 352(6283), 2016.
- [7] William Shockley and Hans J. Queisser. Detailed balance limit of efficiency of p-n junction solar cells. *Journal of Applied Physics*, 32(3):510–519, 1961.
- [8] NREL. Best research-cell efficiency chart. 18.11.2019. <https://www.nrel.gov/pv/cell-efficiency.html>.
- [9] Martin A Green, Anita Ho-Baillie, and Henry J Snaith. The emergence of perovskite solar cells. *Nature photonics*, 8(7):506, 2014.
- [10] B. Goldstein. Properties of photovoltaic films of CdTe. *Phys. Rev.*, 109:601–603, Jan 1958.

- [11] Michio Matsumura, Yoichi Nomura, and Hiroshi Tsubomura. Dye-sensitization on the photocurrent at zinc oxide electrode in aqueous electrolyte solution. *Bulletin of the Chemical Society of Japan*, 50(10):2533–2537, 1977.
- [12] M Beley, P Chartier, V Ern, et al. Dye sensitization of ceramic semiconducting electrodes for photoelectrochemical conversion. *Revue de Physique Appliquée*, 16(1):5–10, 1981.
- [13] Jean Desilvestro, Michael Grätzel, Ladislav Kavan, Jacques Moser, and Jan Augustynski. Highly efficient sensitization of titanium dioxide. *Journal of the American Chemical Society*, 107(10):2988–2990, 1985.
- [14] Brian O'Regan and Michael Grätzel. A low-cost, high-efficiency solar cell based on dye-sensitized colloidal TiO<sub>2</sub> films. *Nature*, 353(6346):737, 1991.
- [15] Anders Hagfeldt, Gerrit Boschloo, Licheng Sun, Lars Kloo, and Henrik Pettersson. Dye-sensitized solar cells. *Chemical reviews*, 110(11):6595–6663, 2010.
- [16] Gerrit Boschloo and Anders Hagfeldt. Characteristics of the iodide/triiodide redox mediator in dye-sensitized solar cells. *Accounts of Chemical Research*, 42(11):1819–1826, 2009. PMID: 19845388.
- [17] Sandra M. Feldt, Elizabeth A. Gibson, Erik Gabrielsson, Licheng Sun, Gerrit Boschloo, and Anders Hagfeldt. Design of organic dyes and cobalt polypyridine redox mediators for high-efficiency dye-sensitized solar cells. *Journal of the American Chemical Society*, 132(46):16714–16724, 2010. PMID: 21047080.
- [18] Mirko Magni, Roberto Giannuzzi, Alessia Colombo, Maria Pia Cipolla, Claudia Dragonetti, Stefano Caramori, Stefano Carli, Roberto Grisorio, Gian Paolo Suranna, Carlo Alberto Bignozzi, Dominique Roberto, and Michele Manca. Tetracoordinated bis-phenanthroline copper-complex couple as efficient redox mediators for dye solar cells. *Inorganic Chemistry*, 55(11):5245–5253, 2016. PMID: 27212146.
- [19] Torben Daeneke, Tae-Hyuk Kwon, Andrew B Holmes, Noel W Duffy, Udo Bach, and Leone Spiccia. High-efficiency dye-sensitized solar cells with ferrocene-based electrolytes. *Nature chemistry*, 3(3):211, 2011.
- [20] Haining Tian, Ze Yu, Anders Hagfeldt, Lars Kloo, and Licheng Sun. Organic redox couples and organic counter electrode for efficient organic dye-sensitized

- solar cells. *Journal of the American Chemical Society*, 133(24):9413–9422, 2011. PMID: 21591709.
- [21] Mingkui Wang, Nathalie Chamberland, Livain Breau, Jacques-E Moser, Robin Humphry-Baker, Benoît Marsan, Shaik M Zakeeruddin, and Michael Grätzel. An organic redox electrolyte to rival triiodide/iodide in dye-sensitized solar cells. *Nature Chemistry*, 2(5):385, 2010.
- [22] Aswani Yella, Simon Mathew, Sadig Aghazada, Pascal Comte, Michael Grätzel, and Mohammad Khaja Nazeeruddin. Dye-sensitized solar cells using cobalt electrolytes: the influence of porosity and pore size to achieve high-efficiency. *J. Mater. Chem. C*, 5:2833–2843, 2017.
- [23] Saif A. Haque, Yasuhiro Tachibana, Richard L. Willis, Jacques E. Moser, Michael Grätzel, David R. Klug, and James R. Durrant. Parameters influencing charge recombination kinetics in dye-sensitized nanocrystalline titanium dioxide films. *The Journal of Physical Chemistry B*, 104(3):538–547, 2000.
- [24] Jenny Nelson. Continuous-time random-walk model of electron transport in nanocrystalline TiO<sub>2</sub> electrodes. *Phys. Rev. B*, 59:15374–15380, Jun 1999.
- [25] Joseph H Montoya, Linsey C Seitz, Pongkarn Chakthranont, Aleksandra Vojvodic, Thomas F Jaramillo, and Jens K Nørskov. Materials for solar fuels and chemicals. *Nature materials*, 16(1):70–81, 2017.
- [26] Roel van de Krol and Michael Grätzel. Photoelectrochemical hydrogen production. 2012. Springer US.
- [27] Oscar Khaselev and John A. Turner. A monolithic photovoltaic-photoelectrochemical device for hydrogen production via water splitting. *Science*, 280(5362):425–427, 1998.
- [28] Jieyang Jia, Linsey C Seitz, Jesse D Benck, Yijie Huo, Yusi Chen, Jia Wei Desmond Ng, Taner Bilir, James S Harris, and Thomas F Jaramillo. Solar water splitting by photovoltaic-electrolysis with a solar-to-hydrogen efficiency over 30%. *Nature communications*, 7:13237, 2016.
- [29] Jifang Zhang, Rodrigo Garcia-Rodriguez, Petra Cameron, and Salvador Eslava. Role of cobalt-iron (oxy)hydroxide (cofeox) as oxygen evolution catalyst on hematite photoanodes. *Energy Environ. Sci.*, 11:2972–2984, 2018.

- [30] A.B. Murphy, P.R.F. Barnes, L.K. Randeniya, I.C. Plumb, I.E. Grey, M.D. Horne, and J.A. Glasscock. Efficiency of solar water splitting using semiconductor electrodes. *International Journal of Hydrogen Energy*, 31(14):1999 – 2017, 2006.
- [31] Omid Zandi and Thomas W. Hamann. The potential versus current state of water splitting with hematite. *Phys. Chem. Chem. Phys.*, 17:22485–22503, 2015.
- [32] Michael Grätzel. Photoelectrochemical cells. *Nature*, 414(6861):338, 2001.
- [33] Kevin Sivula, Florian Le Formal, and Michael Grätzel. WO<sub>3</sub>-Fe<sub>2</sub>O<sub>3</sub> photoanodes for water splitting: A host scaffold, guest absorber approach. *Chem. Mater.*, 21(13):2862–2867, 2009.
- [34] J. H. Kennedy and K. W. Frese. Photooxidation of water at  $\alpha$ -Fe<sub>2</sub>O<sub>3</sub> electrodes. *J. Electrochem. Soc.*, 125:709, 1978.
- [35] P. J. Boddy. Oxygen evolution on semiconducting TiO<sub>2</sub>. *J. Electrochem. Soc.*, 115:199, 1968.
- [36] A. Fujishima and K. Honda. Electrochemical photolysis of water at a semiconductor electrode. *Nature*, 238:37, 1972.
- [37] W. H. Leng, Piers R. F. Barnes, Mindaugas Juozapavicius, Brian C. O Regan, and James R. Durrant. Electron diffusion length in mesoporous nanocrystalline TiO<sub>2</sub> photoelectrodes during water oxidation. *J. Phys. Chem. Lett.*, 1(6):967–972, 2010.
- [38] P. Salvador. Hole diffusion length in nTiO<sub>2</sub> single crystals and sintered electrodes: Photoelectrochemical determination and comparative analysis. *Journal of Applied Physics*, 55(8):2977–2985, 1984.
- [39] Xiaobo Chen and Annabella Selloni. Introduction: Titanium dioxide (TiO<sub>2</sub>) nanomaterials. *Chemical Reviews*, 114(19):9281–9282, 2014. PMID: 25294394.
- [40] Matteo Cargnello, Thomas R. Gordon, and Christopher B. Murray. Solution-phase synthesis of titanium dioxide nanoparticles and nanocrystals. *Chemical Reviews*, 114(19):9319–9345, 2014. PMID: 25004056.

- [41] Xudong Wang, Zhaodong Li, Jian Shi, and Yanhao Yu. One-dimensional titanium dioxide nanomaterials: Nanowires, nanorods, and nanobelts. *Chemical Reviews*, 114(19):9346–9384, 2014. PMID: 24725155.
- [42] Lianzhou Wang and Takayoshi Sasaki. Titanium oxide nanosheets: Graphene analogues with versatile functionalities. *Chemical Reviews*, 114(19):9455–9486, 2014. PMID: 24754464.
- [43] Dina Fattakhova-Rohlfing, Adriana Zaleska, and Thomas Bein. Three-dimensional titanium dioxide nanomaterials. *Chemical Reviews*, 114(19):9487–9558, 2014. PMID: 25137128.
- [44] Yanwu Zhu, Shanthi Murali, Weiwei Cai, Xuesong Li, Ji Won Suk, Jeffrey R. Potts, and Rodney S. Ruoff. Graphene and graphene oxide: Synthesis, properties, and applications. *Advanced Materials*, 22(35):3906–3924, 2010.
- [45] Marianna Kemell, Viljami Pore, Mikko Ritala, Markku Leskelä, and Mika Lindén. Atomic layer deposition in nanometer-level replication of cellulosic substances and preparation of photocatalytic TiO<sub>2</sub>/cellulose composites. *Journal of the American Chemical Society*, 127(41):14178–14179, 2005.
- [46] GK Hyde, SD McCullen, S Jeon, SM Stewart, H Jeon, EG Lobo, and GN Parsons. Atomic layer deposition and biocompatibility of titanium nitride nano-coatings on cellulose fiber substrates. *Biomedical materials*, 4(2):025001, 2009.
- [47] G Kevin Hyde, Giovanna Scarel, Joseph C Spagnola, Qing Peng, Kyoungmi Lee, Bo Gong, Kim G Roberts, Kelly M Roth, Christopher A Hanson, Christina K Devine, et al. Atomic layer deposition and abrupt wetting transitions on non-woven polypropylene and woven cotton fabrics. *Langmuir*, 26(4):2550–2558, 2009.
- [48] Juuso T. Korhonen, Panu Hiekkataipale, Jari Malm, Maarit Karppinen, Olli Ikkala, and Robin H. A. Ras. Inorganic hollow nanotube aerogels by atomic layer deposition onto native nanocellulose templates. *ACS Nano*, 5(3):1967–1974, 2011. PMID: 21361349.
- [49] Christian Buesch, Sean W. Smith, Peter Eschbach, John F. Conley, and John Simonsen. The microstructure of cellulose nanocrystal aerogels as revealed by transmission electron microscope tomography. *Biomacromolecules*, 17(9):2956–2962, 2016. PMID: 27500897.

- [50] Suk-Jun Jung, Seung-Hyun Kim, and Ill-Min Chung. Comparison of lignin, cellulose, and hemicellulose contents for biofuels utilization among 4 types of lignocellulosic crops. *Biomass and Bioenergy*, 83:322 – 327, 2015.
- [51] Kevin J. De France, Todd Hoare, and Emily D. Cranston. Review of hydrogels and aerogels containing nanocellulose. *Chemistry of Materials*, 29(11):4609–4631, 2017.
- [52] Robert J. Moon, Ashlie Martini, John Nairn, John Simonsen, and Jeff Youngblood. Cellulose nanomaterials review: structure, properties and nanocomposites. *Chem. Soc. Rev.*, 40:3941–3994, 2011.
- [53] Eero Kontturi, Päivi Laaksonen, Markus B. Linder, Nonappa, Andre H. Gröschel, Orlando J. Rojas, and Olli Ikkala. Advanced materials through assembly of nanocelluloses. *Advanced Materials*, 30(24):1703779, 2018.
- [54] Xuan Yang and Emily D. Cranston. Chemically cross-linked cellulose nanocrystal aerogels with shape recovery and superabsorbent properties. *Chemistry of Materials*, 26(20):6016–6025, 2014.
- [55] Yuri Kobayashi, Tsuguyuki Saito, and Akira Isogai. Aerogels with 3D ordered nanofiber skeletons of liquid-crystalline nanocellulose derivatives as tough and transparent insulators. *Angewandte Chemie*, 126(39):10562–10565, 2014.
- [56] Xuan Yang, Kaiyuan Shi, Igor Zhitomirsky, and Emily D. Cranston. Cellulose nanocrystal aerogels as universal 3D lightweight substrates for supercapacitor materials. *Advanced Materials*, 27(40):6104–6109, 2015.
- [57] Aurélien Henry, Sandrine Plumejeau, Laurent Heux, Nicolas Louvain, Laure Monconduit, Lorenzo Stievano, and Bruno Boury. Conversion of nanocellulose aerogel into TiO<sub>2</sub> and TiO<sub>2</sub>@C nano-thorns by direct anhydrous mineralization with TiCl<sub>4</sub>. evaluation of electrochemical properties in li batteries. *ACS Applied Materials & Interfaces*, 7(27):14584–14592, 2015. PMID: 25881329.
- [58] Daniel O. Carlsson, Gustav Nyström, Qi Zhou, Lars A. Berglund, Leif Nyholm, and Maria Strømme. Electroactive nanofibrillated cellulose aerogel composites with tunable structural and electrochemical properties. *J. Mater. Chem.*, 22:19014–19024, 2012.
- [59] Kezheng Gao, Ziqiang Shao, Xi Wang, Yunhua Zhang, Wenjun Wang, and Feijun Wang. Cellulose nanofibers/multi-walled carbon nanotube nanohybrid



- aerogel for all-solid-state flexible supercapacitors. *RSC Adv.*, 3:15058–15064, 2013.
- [60] Christian Aulin, Julia Netrval, Lars Wagberg, and Tom Lindström. Aerogels from nanofibrillated cellulose with tunable oleophobicity. *Soft Matter*, 6:3298–3305, 2010.
- [61] Hua Jin, Marjo Kettunen, Ari Laiho, Hanna Pynnönen, Jouni Paltakari, Abraham Marmur, Olli Ikkala, and Robin H. A. Ras. Superhydrophobic and superoleophobic nanocellulose aerogel membranes as bioinspired cargo carriers on water and oil. *Langmuir*, 27(5):1930–1934, 2011. PMID: 21247181.
- [62] Juuso T. Korhonen, Marjo Kettunen, Robin H. A. Ras, and Olli Ikkala. Hydrophobic nanocellulose aerogels as floating, sustainable, reusable, and recyclable oil absorbents. *ACS Applied Materials & Interfaces*, 3(6):1813–1816, 2011. PMID: 21627309.
- [63] Marjo Kettunen, Riitta J. Silvennoinen, Nikolay Houbenov, Antti Nykänen, Janne Ruokolainen, Jani Sainio, Viljami Pore, Marianna Kemell, Mikael Ankerfors, Tom Lindström, Mikko Ritala, Robin H. A. Ras, and Olli Ikkala. Photo-switchable superabsorbency based on nanocellulose aerogels. *Advanced Functional Materials*, 21(3):510–517, 2011.
- [64] Marjo Pääkkö, Jaana Vapaavuori, Riitta Silvennoinen, Harri Kosonen, Mikael Ankerfors, Tom Lindström, Lars A. Berglund, and Olli Ikkala. Long and entangled native cellulose i nanofibers allow flexible aerogels and hierarchically porous templates for functionalities. *Soft Matter*, 4:2492–2499, 2008.
- [65] Wenshuai Chen, Qing Li, Youcheng Wang, Xin Yi, Jie Zeng, Haipeng Yu, Yixing Liu, and Jian Li. Comparative study of aerogels obtained from differently prepared nanocellulose fibers. *ChemSusChem*, 7(1):154–161, 2014.
- [66] Kati Miettunen, Jaana Vapaavuori, Armi Tiihonen, Aapo Poskela, Panu Lahtinen, Janne Halme, and Peter Lund. Nanocellulose aerogel membranes for optimal electrolyte filling in dye solar cells. *Nano Energy*, 8:95 – 102, 2014.
- [67] Hanna Valo, Suvi Arola, Päivi Laaksonen, Mika Torkkeli, Leena Peltonen, Markus B. Linder, Ritva Serimaa, Shigenori Kuga, Jouni Hirvonen, and Timo Laaksonen. Drug release from nanoparticles embedded in four different nanofibrillar cellulose aerogels. *European Journal of Pharmaceutical Sciences*, 50(1):69 – 77, 2013.

- [68] Sui Zhang, Kai Yu Wang, Tai-Shung Chung, Hongmin Chen, Y.C. Jean, and Gary Amy. Well-constructed cellulose acetate membranes for forward osmosis: Minimized internal concentration polarization with an ultra-thin selective layer. *Journal of Membrane Science*, 360(1):522 – 535, 2010.
- [69] Stephanie Beck-Candanedo, Maren Roman, and Derek G. Gray. Effect of reaction conditions on the properties and behavior of wood cellulose nanocrystal suspensions. *Biomacromolecules*, 6(2):1048–1054, 2005. PMID: 15762677.
- [70] Daniel A. Osorio, Bernhard Seifried, Paul Moquin, Kathryn Grandfield, and Emily D. Cranston. Morphology of cross-linked cellulose nanocrystal aerogels: cryo-templating versus pressurized gas expansion processing. *Journal of Materials Science*, 53(13):9842–9860, Jul 2018.
- [71] Markku Leskelä and Mikko Ritala. Atomic layer deposition chemistry: Recent developments and future challenges. *Angewandte Chemie International Edition*, 42(45):5548–5554, 2003.
- [72] Richard W. Johnson, Adam Hultqvist, and Stacey F. Bent. A brief review of atomic layer deposition: from fundamentals to applications. *Materials Today*, 17(5):236 – 246, 2014.
- [73] Markku Hannula, Harri Ali-Löytty, Kimmo Lahtonen, Essi Sarlin, Jesse Saari, and Mika Valden. Improved stability of atomic layer deposited amorphous TiO<sub>2</sub> photoelectrode coatings by thermally induced oxygen defects. *Chemistry of Materials*, 30(4):1199–1208, 2018.
- [74] Jeffrey A. Klug, Nicholas G. Becker, Shannon C. Riha, Alex B. F. Martinson, Jeffrey W. Elam, Michael J. Pellin, and Thomas Proslier. Low temperature atomic layer deposition of highly photoactive hematite using iron(iii) chloride and water. *J. Mater. Chem. A*, 1:11607–11613, 2013.
- [75] Seigo Ito, Takurou N Murakami, Pascal Comte, Paul Liska, Carole Grätzel, Mohammad K Nazeeruddin, and Michael Grätzel. Fabrication of thin film dye sensitized solar cells with solar to electric power conversion efficiency over 10%. *Thin solid films*, 516(14):4613–4619, 2008.
- [76] Sandeep Pathak, Alessandro Sepe, Aditya Sadhanala, Felix Deschler, Amir Haghighirad, Nobuya Sakai, Karl C. Goedel, Samuel D. Stranks, Nakita Noel, Michael Price, Sven Hüttner, Nicholas A. Hawkins, Richard H. Friend, Ullrich

- Steiner, and Henry J. Snaith. Atmospheric influence upon crystallization and electronic disorder and its impact on the photophysical properties of organic-inorganic perovskite solar cells. *ACS Nano*, 9(3):2311–2320, 2015.
- [77] Arto Hiltunen, Kimmo Lahtonen, Jesse Saari, Anniina Ojanperä, Essi Sarlin, Holger Wondraczek, Alexander Efimov, Kimmo Kaunisto, Paola Vivo, Chiara Maccato, Davide Barreca, Pedro Fardim, Nikolai Tkachenko, Mika Valden, and Helge Lemmetyinen. Tailored fabrication of transferable and hollow weblike titanium dioxide structures. *ChemPhysChem*, 18(1):64–71, 2017.
- [78] Zhaodong Li, Chunhua Yao, Yanhao Yu, Zhiyong Cai, and Xudong Wang. Highly efficient capillary photoelectrochemical water splitting using cellulose nanofiber templated TiO<sub>2</sub> photoanodes. *Advanced Materials*, 26(14):2262–2267.
- [79] Thomas W. Hamann, Alex B. F. Martinson, Jeffrey W. Elam, Michael J. Pellin, and Joseph T. Hupp. Atomic layer deposition of TiO<sub>2</sub> on aerogel templates: New photoanodes for dye-sensitized solar cells. *The Journal of Physical Chemistry C*, 112(27):10303–10307, 2008.
- [80] Aravind Kumar Chandiran, Aswani Yella, Morgan Stefiik, Leo-Philipp Heiniger, Pascal Comte, Mohammad. K. Nazeeruddin, and Michael Grätzel. Low-temperature crystalline titanium dioxide by atomic layer deposition for dye-sensitized solar cells. *ACS Applied Materials & Interfaces*, 5(8):3487–3493, 2013. PMID: 23506374.
- [81] Alex B. F. Martinson, Jeffrey W. Elam, Jun Liu, Michael J. Pellin, Tobin J. Marks, and Joseph T. Hupp. Radial electron collection in dye-sensitized solar cells. *Nano Letters*, 8(9):2862–2866, 2008. PMID: 18700800.
- [82] Elham Ghadiri, Nima Taghavinia, Shaik M. Zakeeruddin, Michael Grätzel, and Jacques-E. Moser. Enhanced electron collection efficiency in dye-sensitized solar cells based on nanostructured TiO<sub>2</sub> hollow fibers. *Nano Letters*, 10(5):1632–1638, 2010. PMID: 20423062.
- [83] Alesja Ivanova, Maria C. Fravventura, Dina Fattakhova-Rohlfing, Jiri Rathouský, Liana Movsesyan, Pirmin Ganter, Tom J. Savenije, and Thomas Bein. Nanocellulose-templated porous titania scaffolds incorporating presynthesized titania nanocrystals. *Chemistry of Materials*, 27(18):6205–6212, 2015.

- [84] Tyler Or, Sokunthearath Saem, Aurore Esteve, Daniel A. Osorio, Kevin J. De France, Jaana Vapaavuori, Todd Hoare, Aline Cerf, Emily D. Cranston, and Jose M. Moran-Mirabal. Patterned cellulose nanocrystal aerogel films with tunable dimensions and morphologies as ultra-porous scaffolds for cell culture. *ACS Applied Nano Materials*, 2(7):4169–4179, 2019.
- [85] W. Justin Youngblood, Seung-Hyun Anna Lee, Kazuhiko Maeda, and Thomas E. Mallouk. Visible light water splitting using dye-sensitized oxide semiconductors. *Accounts of Chemical Research*, 42(12):1966–1973, 2009. PMID: 19905000.
- [86] Omid Zandi and Thomas W. Hamann. The potential versus current state of water splitting with hematite. *Phys. Chem. Chem. Phys.*, 17:22485–22503, 2015.
- [87] Stepan Kment, Francesca Riboni, Sarka Pausova, Lei Wang, Lingyun Wang, Hyungkyu Han, Zdenek Hubicka, Josef Krysa, Patrik Schmuki, and Radek Zboril. Photoanodes based on TiO<sub>2</sub> and  $\alpha$ -Fe<sub>2</sub>O<sub>3</sub> for solar water splitting - superior role of 1D nanoarchitectures and of combined heterostructures. *Chem. Soc. Rev.*, 46:3716–3769, 2017.
- [88] Morgan Stefik, Maurin Cornuz, Nripan Mathews, Takashi Hisatomi, Subodh Mhaisalkar, and Michael Grätzel. Transparent, conducting Nb:SnO<sub>2</sub> for host-guest photoelectrochemistry. *Nano Lett.*, 12(10):5431–5435, 2012.
- [89] Lifeng Liu. Efficient water oxidation using  $\alpha$ -Fe<sub>2</sub>O<sub>3</sub> thin films conformally coated on vertically aligned titania nanotube arrays by atomic layer deposition. *Mater. Lett.*, 159(Supplement C):284 – 288, 2015.
- [90] Qinghua Liu, Jingfu He, Tao Yao, Zhihu Sun, Weiren Cheng, Shi He, Yi Xie, Yanhua Peng, Hao Cheng, Yongfu Sun, Yong Jiang, Fengchun Hu, Zhi Xie, Wensheng Yan, Zhiyun Pan, Ziyu Wu, and Shiqiang Wei. Aligned Fe<sub>2</sub>TiO<sub>5</sub>-containing nanotube arrays with low onset potential for visible-light water oxidation. *Nat. Commun.*, 5(5122), 2014.
- [91] Damian Monllor-Satoca, Mario Bartsch, Cristian Fabrega, Aziz Genc, Sandra Reinhard, Teresa Andreu, Jordi Arbiol, Markus Niederberger, and Joan Ramon Morante. What do you do, titanium? insight into the role of titanium oxide as a water oxidation promoter in hematite-based photoanodes. *Energy Environ. Sci.*, 8:3242–3254, 2015.

- [92] Omid Zandi, Benjamin M. Klahr, and Thomas W. Hamann. Highly photoactive Ti-doped  $\alpha$ -Fe<sub>2</sub>O<sub>3</sub> thin film electrodes: resurrection of the dead layer. *Energy Environ. Sci.*, 6:634–642, 2013.
- [93] E. Courtin, G. Baldinozzi, M. T. Sougrati, L. Stievano, C. Sanchez, and C. Laberty-Robert. New Fe<sub>2</sub>TiO<sub>5</sub>-based nanoheterostructured mesoporous photoanodes with improved visible light photoresponses. *J. Mater. Chem. A*, 2:6567–6577, 2014.
- [94] Arto Hiltunen, Tero-Petri Ruoko, Tomi Iivonen, Kimmo Lahtonen, Harri Ali-Löytty, Essi Sarlin, Mika Valden, Markku Leskelä, and Nikolai Tkachenko. Design aspects of all atomic layer deposited TiO<sub>2</sub>-Fe<sub>2</sub>O<sub>3</sub> scaffold-absorber photoanodes for water splitting. *Sustainable Energy Fuels*, 2:2124–2130, 2018.
- [95] Shayne Sorenson, Eric Driscoll, Shima Haghghat, and Jahan M Dawlaty. Ultrafast carrier dynamics in hematite films: The role of photoexcited electrons in the transient optical response. *J. Phys. Chem. C*, 118(41):23621–23626, 2014.



## ORIGINAL PAPERS





# I

## Tailored fabrication of transferable and hollow weblike titanium dioxide structures

by

Arto Hiltunen, Kimmo Lahtonen, Jesse Saari, Anniina Ojanperä, Essi Sarlin, Holger Wondraczek, Alexander Efimov, Kimmo Kaunisto, Paola Vivo, Chiara Maccato, Davide Barreca, Pedro Fardim, Nikolai Tkachenko, Mika Valden, and Helge Lemmetyinen

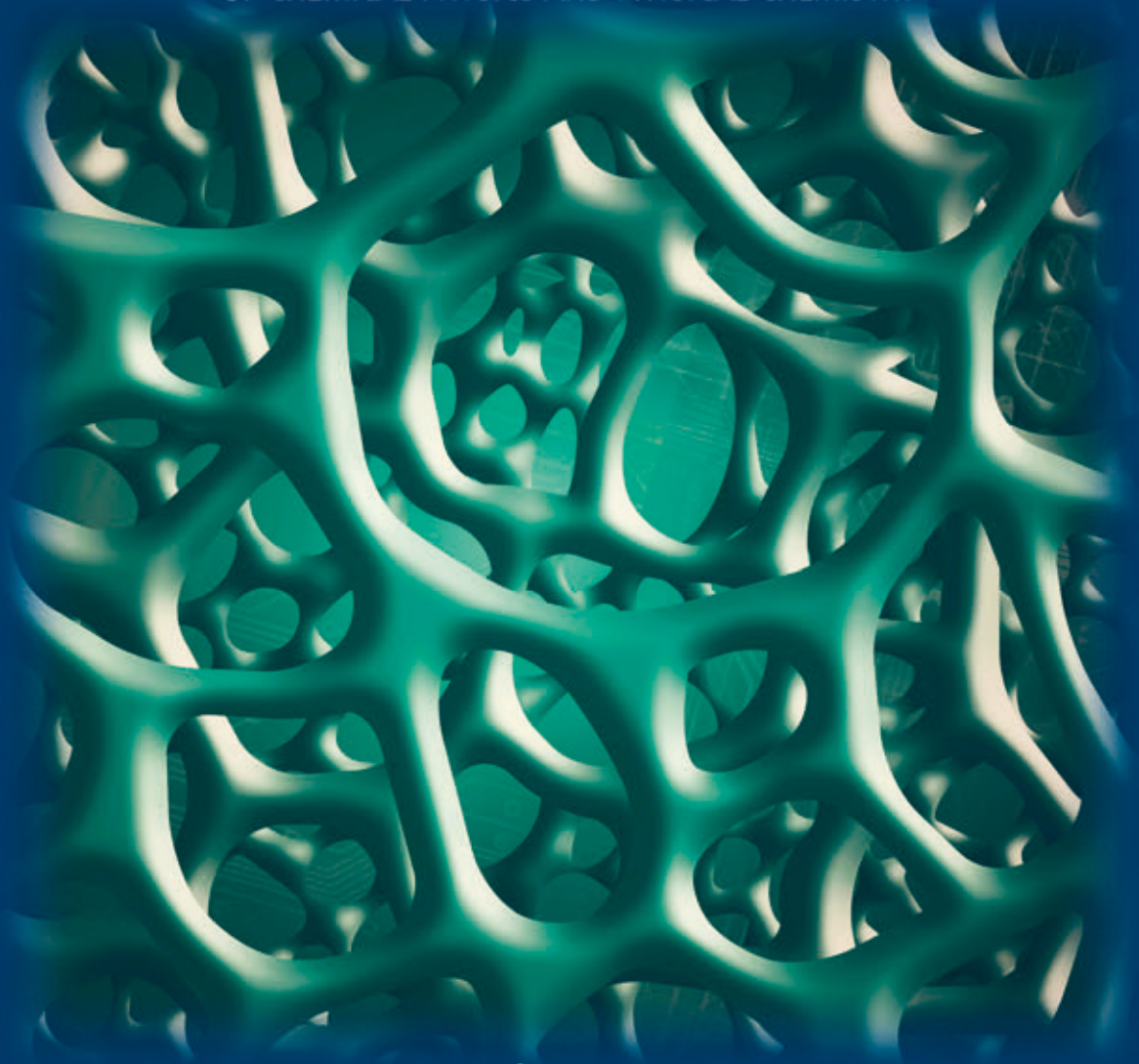
ChemPhysChem **2017**, 18, 64-71

Reproduced by permission of John Wiley and Sons  
©2017 Wiley-VCH Verlag GmbH & Co. KGaA, Weinheim.

A EUROPEAN JOURNAL

# CHEMPHYSCHEM

OF CHEMICAL PHYSICS AND PHYSICAL CHEMISTRY



1/2017

**Cover Picture:**

*A. Hiltunen et al.*

Tailored Fabrication of Transferable and Hollow Weblike Titanium  
Dioxide Structures

A Journal of



WILEY-VCH

[www.chemphyschem.org](http://www.chemphyschem.org)



# Tailored Fabrication of Transferable and Hollow Weblike Titanium Dioxide Structures

Arto Hiltunen,<sup>\*,[a]</sup> Kimmo Lahtonen,<sup>[b]</sup> Jesse Saari,<sup>[b]</sup> Anniina Ojanperä,<sup>[a]</sup> Essi Sarlin,<sup>[c]</sup> Holger Wondraczek,<sup>[d]</sup> Alexander Efimov,<sup>[a]</sup> Kimmo Kaunisto,<sup>[a]</sup> Paola Vivo,<sup>[a]</sup> Chiara Maccato,<sup>[e]</sup> Davide Barreca,<sup>[f]</sup> Pedro Fardim,<sup>[d, g]</sup> Nikolai Tkachenko,<sup>[a]</sup> Mika Valden,<sup>[b]</sup> and Helge Lemmetyinen<sup>[a]</sup>

The preparation of weblike titanium dioxide thin films by atomic layer deposition on cellulose biotemplates is reported. The method produces a TiO<sub>2</sub> web, which is flexible and transferable from the deposition substrate to that of the end application. Removal of the cellulose template by calcination converts the amorphous titania to crystalline anatase and gives the structure a hollow morphology. The TiO<sub>2</sub> webs are thor-

oughly characterized using electron microscopy, X-ray diffraction, and X-ray photoelectron spectroscopy to give new insight into manufacturing of porous titanium dioxide structures by means of template-based methods. Functionality and integrity of the TiO<sub>2</sub> hollow weblike thin films were successfully confirmed by applying them as electrodes in dye-sensitized solar cells.

## 1. Introduction

Modern technologies related to energy storage and conversion, catalysis, sensing, and medicine impose various demands over the active materials and substrates. Nanoscale features, porous structures, and flexibility are often required today.<sup>[1–3]</sup> Porosity combined with nanoscale features is often the requisite for high catalytic activity, which is a result of increased sur-

face area, leading to high performance,<sup>[4]</sup> whereas flexibility is often sought for improved user experience and design.<sup>[5]</sup>

Hollow structures increase the surface area even further relative to their solid counterparts by making the both inner and outer surfaces possible active sites. Hollow structures are especially attractive in lithium-ion battery technology due to increased lithium storage sites and large contact area with the electrolyte. Furthermore, the hollow structure can alleviate strain associated with volume changes related to battery cycling processes.<sup>[6]</sup> Hollow structures for lithium-ion batteries have been demonstrated in various geometries, including TiO<sub>2</sub> spheres,<sup>[7]</sup> microboxes,<sup>[8]</sup> and ellipsoids.<sup>[9]</sup> In addition, TiO<sub>2</sub> hollow structures are advantageous in sensor technology.<sup>[10,11]</sup> Medical applications have multiple uses for hollow structures, including the encapsulation of a drug inside the inner surface of a nanoparticle and functionalizing the outer surface for drug targeting.<sup>[12]</sup>

Several methods have been developed to manufacture porous structures; titanium dioxide is the workhorse material.<sup>[13]</sup> In particular, wet synthetic routes are used to obtain spherical structures with various geometries. The solution synthesis, however, still requires several steps under strict reaction conditions that are prone to cause undesired variations in the end product. In addition, the use of inorganic templates (e.g. spherical SiO<sub>2</sub>) means that they must be removed by using strong chemicals, such as HF, which is still commonly employed to produce hollow TiO<sub>2</sub> spheres.<sup>[14]</sup> To overcome problems imposed by inorganic templates, organic templates can be used due to their easy removal by calcination. In this context, cellulose-based materials are attractive choices thanks to their abundance and nontoxicity.

Previously, cellulose-templated metal oxide thin films have been cast from a paste prepared from the crushed metal oxide

[a] A. Hiltunen, A. Ojanperä, Dr. A. Efimov, Dr. K. Kaunisto, Dr. P. Vivo, Prof. N. Tkachenko, Prof. H. Lemmetyinen  
Department of Chemistry and Bioengineering  
Tampere University of Technology  
P.O. Box 541, 33101 Tampere (Finland)  
E-mail: arto.j.hiltunen@tut.fi

[b] Dr. K. Lahtonen, J. Saari, Prof. M. Valden  
Surface Science Laboratory, Optoelectronics Research Centre  
Tampere University of Technology  
P.O. Box 692, 33101 Tampere (Finland)

[c] Dr. E. Sarlin  
Department of Materials Science  
Tampere University of Technology  
P.O. Box 589, 33101 Tampere (Finland)

[d] Dr. H. Wondraczek, Prof. P. Fardim  
Laboratory of Fibre and Cellulose Technology  
Åbo Akademi University  
Porthansgatan 3, 20500 Turku (Finland)

[e] Prof. C. Maccato  
INSTM, Department of Chemistry  
Padova University, 35131, Padova (Italy)

[f] Dr. D. Barreca  
CNR-ICMATE and INSTM, Department of Chemistry  
Padova University, 35131, Padova (Italy)

[g] Prof. P. Fardim  
Department of Chemical Engineering  
University of Leuven  
Celestijnenlaan 200F bus 2424, B-3001 Leuven Belgium

Supporting Information and the ORCID identification number(s) for the author(s) of this article can be found under <http://dx.doi.org/10.1002/cphc.201600930>.

nanostructure, as a result of template removal.<sup>[15,16]</sup> Ivanova et al. overcame this problem and showed that cellulose-templated metal oxide structures could be prepared directly on the substrate from a nanocrystalline cellulose paste containing a titanium dioxide precursor, followed by combustion of template, and simultaneous crystallization of  $\text{TiO}_2$ .<sup>[17]</sup> Li et al.<sup>[18]</sup> used atomic layer deposition<sup>[19]</sup> (ALD) to deposit  $\text{TiO}_2$  directly on a thin nanocrystalline cellulose film. Their solution requires that the substrate is suitable for template preparation. This is not always possible because the substrate might have a complicated geometry, be too small for template preparation, or prevent template casting due to surface interactions. Herein we describe an approach that enables the preparation of transferable templated  $\text{TiO}_2$  films, which means that the substrate of the final application needs to be compatible only with the deposited functional material, but not with the template. This is achieved by ALD of titanium dioxide on porous cellulose acetate templates, which are easily processible and soluble in common organic solvents such as acetone. Transferability is a useful feature in nanoelectronic applications, including supercapacitors,<sup>[20]</sup> water splitting,<sup>[21]</sup> and dye-sensitized solar cells (DSSCs).<sup>[22]</sup>

The transferable thin films have a porous weblike  $\text{TiO}_2$  structure, which is flexible and has continuous interface-free paths for electron transfer along the strings of the web. Template removal by calcination at the crystallization temperature of  $\text{TiO}_2$  gives the web a hollow structure. The chemical composition of the structure is of utmost importance in the development of high-performance devices. The number of impurities, doping levels, and the oxidation states modify material properties, such as charge carrier concentration and mobility, and may thus have an effect on the performance and lifetime of the devices. Although template-based methods are widely employed, and some reports include XPS results,<sup>[23,26]</sup> the detailed analysis of the chemical composition of the materials under study for different processing steps is often omitted. Herein, we include an XPS study on the ALD-grown  $\text{TiO}_2$  thin films before and after template removal. Finally, the functionality of the  $\text{TiO}_2$  webs is demonstrated by testing them in DSSCs.

Today, ALD can be applied on a roll-to-roll process<sup>[27]</sup> or even open environment outside laboratory conditions on objects such as cars.<sup>[28]</sup> This could make the proposed method applicable on a larger scale as well.

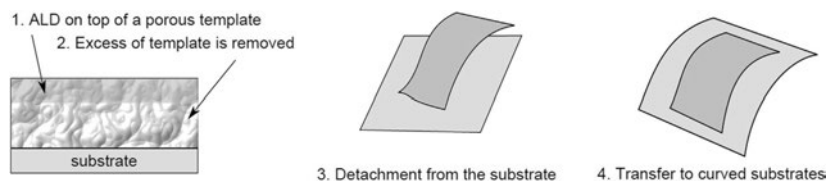


Figure 1. A schematic illustration of transferable thin-film fabrication.

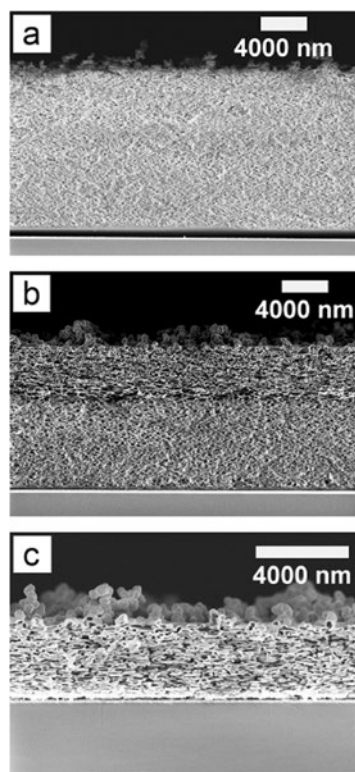


Figure 2. SEM images of the steps of the titania web thin-film preparation. a) First a porous cellulose acetate template is cast, b) then it is coated with titania by means of ALD, and finally c) the template is removed by dissolution and calcination.

## 2. Results and Discussion

The thin-film preparation process is schematically presented in Figure 1 and SEM images of the process are given in Figure 2. Commercially available, cheap, and easily processible cellulose acetate was chosen as the template material for the  $\text{TiO}_2$  webs. A porous cellulose acetate film (Figure 2a) is cast by using a method adapted from the literature<sup>[29]</sup> and used as a template

for ALD. Titania is deposited on the cellulose biotemplates by means of ALD at 100 °C, which results in an amorphous phase at this temperature.<sup>[30]</sup> We observed that it was possible to vary reproducibly the penetration of the ALD precursors into the template by changing the pulsing times, and thus, alter the TiO<sub>2</sub> film thickness. To achieve transferability, pulsing times that leave the bottom part of the template uncoated were selected. By using the reported ALD method, the precursor gases penetrated 4  $\mu\text{m}$  inside the 10  $\mu\text{m}$  thick cellulose template (Figure 2b) to create a 4  $\mu\text{m}$  thick titania structure after dissolution of the excess template (Figure 2c). It was possible to accurately vary the titania layer thickness that grew around the strings of the cellulose template by changing the cycle number: 480 ALD cycles produced a 30 nm thick TiO<sub>2</sub> coating. The film growth was verified ellipsometrically on a reference n-Si(100)(P) substrate, which indicated a titania film thickness of  $(30.0 \pm 0.3)$  nm, with a growth rate of  $0.062 \pm 0.063$  nm/cycle. Penetration of precursor gases into the template was further studied by EDX spectroscopy (Figure S1 in the Supporting Information) to verify titania coating on the upper part of the film only.

The prepared weblike titania structure is shown in Figure 3. It consists of titania strings (Figure 3a), which span a continuous web that extends over the whole film. The diameters of the openings in the web range from 100 nm to 1  $\mu\text{m}$  with an average value of approximately 400 nm. The diameters of the strings vary from 100 to 400 nm, according to the cellulose acetate string thickness in the template. After calcination, the titania strings are hollow due to removal of the template. Figure 3b shows that the cavity diameter in the hollow structure varies from tens of nanometers to a few hundred nanometers with an average value of 250 nm calculated from SEM cross-sectional images. The wall thickness of the titania strings measured from the SEM image matches well with the target value of 30 nm. At the bottom of the web, the titania layer thickness slightly decreases due to reduced diffusion of the ALD precursor gases. The thickness decrease was quantified based on SEM measurements. From the top to the middle of the sample, the TiO<sub>2</sub> layer thickness is close to 30 nm. The thickness decreases down to 15  $\pm$  20 nm at approximately 3.5  $\mu\text{m}$  depth from the sample surface when 4  $\mu\text{m}$  thick films were targeted, resulting in a thinner coating thickness for the last 500 nm. Similar observations were made also for the calcined films.

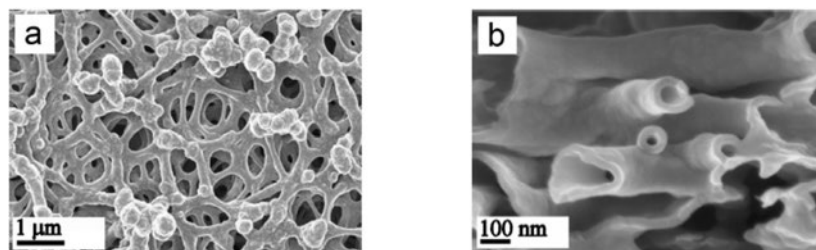


**Figure 3.** SEM images of the resulting titania films. An image a) from the top of the film and b) high magnification of the cross section.

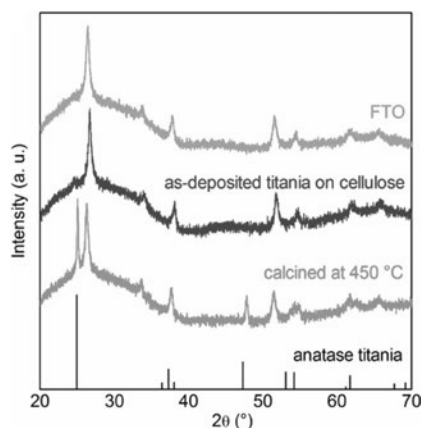


**Figure 4.** XRD pattern of the TiO<sub>2</sub> web before and after calcination.

Prior to calcination, the as-deposited titania is amorphous, as verified by XRD measurements (Figure 4), during which the only reflections observed come from the fluorine-doped tin oxide (FTO) substrate. After calcination, titania is converted into anatase form and the characteristic anatase peaks at  $2\theta = 25^\circ$  and  $47^\circ$  appear in the spectrum (ref. ICDD: 98-016-1908).

Transferability of the TiO<sub>2</sub> webs was achieved through dissolution of excess cellulose acetate in an acetone bath. The web detaches from the substrate in a few seconds and can then be transferred onto another substrate in the bath. It was observed that the film attaches strongly to FTO or glass substrates once the solvent has dried, making them usable without further processing. In the amorphous phase, the TiO<sub>2</sub> web is highly flexible. Flexibility makes it possible to transfer the webs onto curved substrates. Figure 5 shows a photograph of a TiO<sub>2</sub> web, which has been transferred onto a round glass substrate. The fast and easy transfer makes the reported method favorable for practical applications. To obtain a hollow crystalline titania structure, removal of the template was completed by calcining the samples at 450 °C in air at a slow heating rate. Calcination could be realized even when the web had been transferred on the curved glass substrate.

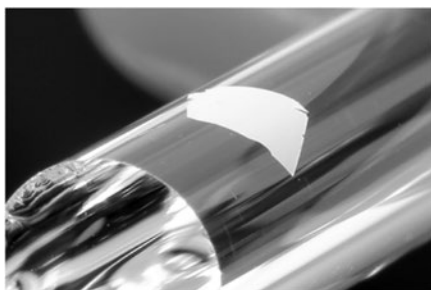


**Figure 5.** Photograph of the web transferred onto a curved substrate 6 mm in diameter.

XPS was employed to determine the chemical composition of the titania web after ALD growth and after removal of the cellulose acetate template by calcination. Figure 6 shows the changes in the  $Ti2p_{3/2}$  and  $N1s$  photoelectron spectra due to the calcining process. The as-deposited titania surface contained 3.3% of  $Ti^{3+}$  suboxides (defects, oxygen vacancies), as indicated by broadening of the  $Ti2p_{3/2}$  spectral features towards lower binding energies (BEs). The symmetric synthetic components were fitted at 458.6 ( $Ti^{4+}$ ) and 456.9 eV ( $Ti^{3+}$ ), as shown in Figure 6a and b. The removal process of the cellulose acetate template by calcining in air decreased the amount of  $Ti^{3+}$  defect states to half and slightly increased the amount of (hydro)carbon contamination (Table 1).

XPS analysis on the cellulose acetate template before ALD enabled us to confirm the absence of nitrogen; thus indicating that both  $N1s$  components shown in Figure 6c and d originate from the deposition process. The assignment of the  $N1s$  photoelectron peaks in the  $N-TiO_2$  system is somewhat controversial.<sup>[35]</sup> Based on previous works, the 399.8 eV component in the  $N1s$  spectrum can be attributed to interstitial N centers ( $N_{int}$ ) in the  $TiO_2$  lattice,<sup>[35,37]</sup> organic  $N-C-H$  species,<sup>[38,39]</sup>  $N_2$  species trapped at grain boundaries, and/or to  $N-O$  bonds in the  $TiO_2$  matrix.<sup>[40]</sup> Nitrogen presumably originates from the functional  $N-CH_3$  groups of the tetrakis(dimethylamino)titanium(IV) (TDMAT) precursor. The higher BE component at 401.7 eV can be associated with chemisorbed  $N$ , adsorbed organic impurities, or  $N-O$  species ( $N_{chem/ads}$ ).<sup>[41,42]</sup> Gole et al.<sup>[43]</sup> and Chen and Burda<sup>[44]</sup> also suggested that a component at

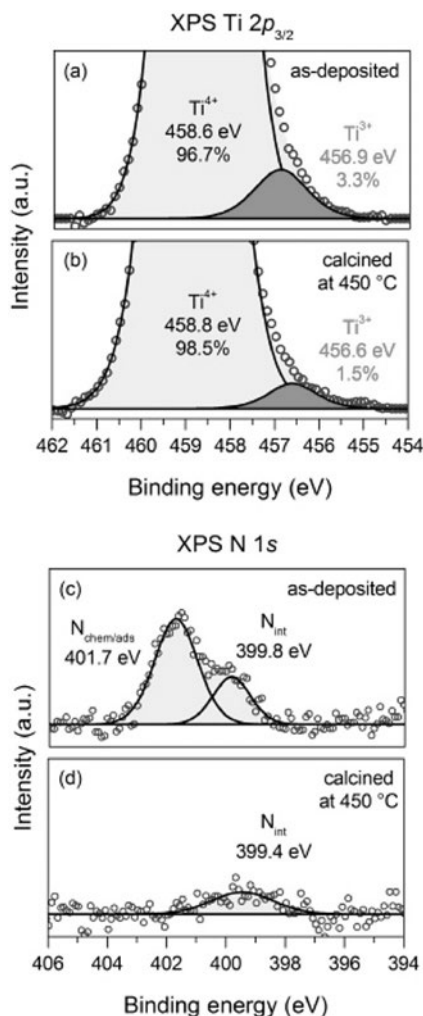


**Figure 6.** XPS  $Ti2p_{3/2}$  (a,b) and XPS  $N1s$  (c,d) spectra of the titania web surface in as-deposited conditions and after removal of the cellulose acetate template by calcining at 450 °C in air.

**Table 1.** Chemical states, relative atomic concentrations, and core-level BEs of the elements determined by XPS on the web titania film.

Sample	Relative concentration (in at%) [component BE in eV]								
	C-C/N/H	C 1s C-O	(O)-C=O	O-Ti	O 1s O-C/C O-H	N 1s $N_{int}$	$N_{chem/ads}$	$Ti^{4+}$	$Ti2p_{3/2}$ $Ti^{3+}$
as-deposited	5.09 [285.0]	3.31 [286.1]	1.75 [289.0]	56.91 [530.2]	6.24 [531.5]	0.38 [399.8]	0.97 [401.7]	24.52 [458.6]	0.83 [456.9]
calcined	9.01	2.39	2.28	52.38	8.36	0.29	<sup>2</sup>	24.90	0.39
at 450 °C	[285.0]	[286.5]	[289.1]	[530.1]	[531.3]	[399.4]	<sup>2</sup>	[458.8]	[456.6]

401.3 eV could be due to N doping and N–Ti–O bond formation, whereas others proposed that the component of substitutional N was located at low BE values (396.2–398 eV).<sup>[35,37,41,42]</sup> The obtained data demonstrated that titanium nitride (396.9<sup>2</sup>–397.4 eV)<sup>[38]</sup> was not present on any studied samples. The removal of the cellulose template by calcining removed all chemisorbed/adsorbed nitrogen and decreased the nitrogen doping level. The full XPS survey spectrum is presented in Figure S2 in the Supporting Information.

The presence of N in the TiO<sub>2</sub> film after calcination can be assumed to be harmless, even useful, since several studies indicate that the usage of N-doped TiO<sub>2</sub> in photoanode applications has advantages over those of pure TiO<sub>2</sub>. Nitrogen doping can be used to tune the optoelectronic and photocatalytic properties of TiO<sub>2</sub>, including band gap engineering, through which the addition of electronic states above the valence band maximum facilitates generation and transport of active charge carriers to the surface under visible-light illumination.<sup>[37,45]</sup>

DSSCs were prepared by using the 4 μm thick titania web as the photoanode sensitized by N719 dye in conjunction with the iodide/triiodide redox couple and platinum counter electrode. Under simulated one sun illumination, a power conversion efficiency (η) of (2.8 ± 0.3)%, fill factor (FF) of (65 ± 2)%, open-circuit voltage (V<sub>oc</sub>) of (0.69 ± 0.01) V, and short-circuit current (I<sub>sc</sub>) of (6.2 ± 0.4) mA cm<sup>-2</sup> were obtained (the IV curve is presented in Figure S3 in the Supporting Information). These values are in the same range as previously reported results for devices employing templated titania electrode morphologies, which take into account that the choices for electrolytes, sensitizers, and device architectures differ.<sup>[15,17,31,34]</sup> The solar cell performances are compared in Table 2.

The amount of dye adsorbed on the titania web was determined by washing the dye from the structure with 1 M NaOH and measuring the absorbance of that solution.<sup>[15]</sup> The surface density of dye was calculated to be 9 × 10<sup>-9</sup> mol cm<sup>-2</sup> for a 4 μm thick web. For comparison, a density of 3 × 10<sup>-8</sup> mol cm<sup>-2</sup> was calculated for a film composed of TiO<sub>2</sub> nanoparticles (Ti-Nanoxide T/SP from Solaronix) with a similar thickness. A lower surface density of the sensitizing dye in the case of titania web is expected because the characteristic pore size of the web is much larger than that of the TiO<sub>2</sub> nanoparticle film.

Structurally the continuous and interface-free strings of the TiO<sub>2</sub> web are well-suited for electron transport compared with

traditional nanoparticle-based electrodes,<sup>[46]</sup> which suffer from hindered electron transport from particle to particle.<sup>[47,48]</sup> Furthermore, the reported method has advantages over previous attempts to build cellulose-templated titania electrodes, which required either milling of the nanofibers<sup>[15,16]</sup> or several deposition steps to grow thicker structures.<sup>[17]</sup> We see these results as a promising proof-of-concept for further development of transferable cellulose-templated titania thin films, which could be applied as electrodes in multiple applications.

### 3. Conclusions

A method to produce weblike titanium dioxide structures by applying ALD on porous cellulose acetate templates was developed. In the amorphous phase, the TiO<sub>2</sub>-web structures were flexible and could be transferred easily to another substrate. The template could be removed by calcination, making the structure hollow and simultaneously converting the titanium dioxide into anatase form. Transfer and subsequent calcination was even achieved on curved substrates. An XPS study on the webs revealed that the Ti<sup>3+</sup> states decreased to half and also nitrogen doping of the oxide lattice decreased due to calcination. Photoactivity and functionality of the weblike TiO<sub>2</sub> structure was demonstrated by successfully applying them as photoanodes in DSSCs.

Modification of cellulose<sup>[49]</sup> is an approach to tune the template properties to suit better particular requirements of the targeted application, which would benefit from the hollow structure, including lithium-ion batteries and sensors. Moreover, this structure could be beneficial for applications requiring bigger pore sizes than those provided by a standard titania nanoparticle film. In particular, the TiO<sub>2</sub> web could serve as a photocatalytic water purification membrane due to suitable pore sizes for bacteria filtration and photocatalytic activity of TiO<sub>2</sub> for the degradation of organic pollutants.<sup>[50]</sup>

### Experimental Section

#### Preparation of Porous Cellulose Templates on Substrates

FTO-coated glass substrates (70 × 90 Ω/square) were cleaned by first sonicating them in a detergent (2% Mucosol); rinsing with water (Milli-Q); and again sonicating in Milli-Q water, acetone, and finally 2-propanol. Each sonication step took 15 min. After sonication, the plates were dried at 150 °C in air and allowed to cool to room tem-

**Table 2.** Comparison of DSSCs employing templated photoanodes. The method reported herein is marked in *italics*.

TiO <sub>2</sub> deposition method	Dye, electrolyte	η [%]	FF [%]	I <sub>sc</sub> [mA cm <sup>-2</sup> ]	V <sub>oc</sub> [V]	Thickness [μm]
solution synthesis on cotton wool <sup>[15]</sup>	C101, I <sup>-</sup> /I <sub>3</sub> <sup>-</sup>	7.15	72	13.0	0.760	9
ALD on SiO <sub>2</sub> nanoparticles <sup>[31]</sup>	YD2-O-C8, Co(II/III)	7.1	71	10.6	0.9425	8
ALD on SiO <sub>2</sub> aerogel templates <sup>[32]</sup>	N719, I <sup>-</sup> /I <sub>3</sub> <sup>-</sup>	4.3	69	9.17	0.67	25
dip coating of nanocrystalline cellulose <sup>[17]</sup>	N719, I <sup>-</sup> /I <sub>3</sub> <sup>-</sup>	3.12	70.9	6.02	0.731	1.8
spin coating on patterned photoresist <sup>[33]</sup>	N719, I <sup>-</sup> /I <sub>3</sub> <sup>-</sup>	2.9 ± 0.3	58 ± 2	6.1 ± 0.3	0.82 ± 0.03	3.7 ± 0.3
<i>ALD on weblike cellulose acetate</i>	N719, I <sup>-</sup> /I <sub>3</sub> <sup>-</sup>	2.8 ± 0.3	65 ± 2	6.2 ± 0.4	0.69 ± 0.01	4
ALD on ITO <sup>[4]</sup> nanotubes <sup>[34]</sup>	N719, I <sup>-</sup> /I <sub>3</sub> <sup>-</sup>	1.1	58	2.6	0.716	60

[a] ITO = indium tin oxide.

perature. The 5 mm wide stripes of cellulose acetate were doctor bladed on cleaned substrates by using tape (Scotch Magic Tape 810) as a spacer from a 271 mg mL<sup>-1</sup> solution of cellulose acetate (CA-398-3 from Eastman) in a 1:5.64 (v/v) mixture of acetone and 1-methyl-2-pyrrolidinone. After doctor blading, the film was dipped into a 1:4 (v/v) mixture of Milli-Q water and 1-methyl-2-pyrrolidinone for 3 s and then into Milli-Q water for 10 min. The films were dried in air at room temperature overnight and shaped into 5 mm × 5 mm squares by using a scalpel. The method to produce the porous cellulose acetate films was adapted from earlier work.<sup>[29]</sup>

### Atomic Layer Deposition of Titanium Oxide

ALD of titanium oxide thin-film deposition was performed on porous cellulose acetate templates and n-Si(100)(P) reference substrates at a substrate temperature of 100 °C by using a Picosun Sunale ALD R200 Advanced reactor. TDMAT (99%, Strem Chemicals, Inc.), deionized water, and Ar (99.9999%, Oy AGA Ab) were used as the Ti precursor, O precursor, and carrier/purge gas, respectively. TDMAT reacted with surface hydroxyl species and adsorbed as Ti[N(CH<sub>3</sub>)<sub>2</sub>]<sub>3</sub>\* surface species. H<sub>2</sub>O reacted with surface methyl species and rehydroxylated the surface. Alternating TDMAT and H<sub>2</sub>O pulses at 100 °C led to the growth of amorphous TiO<sub>2</sub> films.<sup>[30]</sup>

The choice of this precursor as an alternative to classical alkoxides was motivated by the disadvantages associated with the alkoxide tendency to produce oligomers, resulting in an undesired alteration of mass transport properties.<sup>[40]</sup> Alkoxide precursor decomposition also led to an undistinguished ALD temperature window,<sup>[30]</sup> whereas with the TDMAT/H<sub>2</sub>O process growth could be performed at the low temperature needed for a cellulose substrate with low decomposition temperature. In addition, electrodes with TDMAT<sup>2</sup> ALD TiO<sub>2</sub> films showed excellent stability compared with TTIP<sup>2</sup> ALD TiO<sub>2</sub> devices.<sup>[51]</sup>

The precursor vapor pressures were kept constant by sustaining TDMAT bubbling at 76 °C (*P*<sub>v</sub> ≈ 3.6 mbar) and water bubbling at 18 °C (*P*<sub>v</sub> ≈ 21 mbar). The TDMAT connection line was maintained at 85 °C to prevent condensation phenomena. Prior to each growth experiment, the substrate temperature was stabilized for 30 min before the start of deposition. Different ALD recipes were tested to vary the film thickness and penetration depth into the porous cellulose acetate template. After a preliminary optimization of the ALD operating conditions, a 480 cycle recipe at 100 °C substrate temperature, producing the (30.0 ± 0.3) nm film thickness and 4 μm penetration depth, was chosen. The ALD cycle consisted of 1.6 s exposure to TDMAT and 0.1 s exposure to H<sub>2</sub>O, with a 6.0 s purge after each exposure. A constant Ar flow of 100 sccm was maintained in both precursor lines throughout the deposition process.

One of the alternative growth recipes consisted of double pulsing of each precursor. This method increased the penetration depth to 7.5 μm (see Figure S4 in the Supporting Information). However, the single pulsing recipe was chosen because the 4 μm penetration depth was already enough to demonstrate the fabrication and operation of the transferable TiO<sub>2</sub> thin film.

### Removal of Template and Calcination after ALD

Excess cellulose acetate was removed from the electrode by dipping the films into acetone in a Petri dish. The removal of cellulose

acetate caused the titania film to be detached from the FTO substrate. The floating titania web film was carefully placed back on the FTO or transferred to another substrate and removed from the bath and left to dry. To convert the titania to anatase crystals and to complete template removal, the electrode was calcined at 450 °C (heating at an average rate of 7 °C min<sup>-1</sup>) in air for 45 min and cooled at the same rate.

### XPS of the Titania Thin Films

XPS was performed by utilizing non-monochromatized Al Kα X-rays (*h*<sub>ν</sub> = 1486.6 eV) generated by a DAR400 X-ray source (Omicron Nanotechnology GmbH) operated at 300 W for excitation of photoelectrons. Measurements were performed in normal emission with a detection area of 2.93 mm<sup>2</sup>. Core-level spectra were collected with a pass energy of 10 eV, producing a full-width at half-maximum (FWHM) of 1.09 eV for a reference metallic Ag 3d<sub>5/2</sub> peak, employing an Argus hemispherical electron spectrometer (Omicron Nanotechnology GmbH) installed in a multifunctional ultrahigh vacuum (UHV) system with a base pressure below 1 × 10<sup>-10</sup> mbar.<sup>[52]</sup>

The surface elemental concentrations and chemical states of compounds were identified by analyzing the core-level photoemission spectra of C 1s, O 1s, N 1s, and Ti 2p by using CasaXPS software (version 2.3.16 PR 1.6).<sup>[53]</sup> The BE scale was calibrated according to the C 1s C–C/H component at 285.0 eV. After a Shirley-type background subtraction, the peaks were least-squares fitted with a combination of symmetric Gaussian/Lorentzian line shapes. The relative atomic concentrations were calculated by using Scofield photoionization cross sections<sup>[54]</sup> and experimentally measured transmission functions of the Argus analyzer.

The sampling depths of the C 1s, O 1s, N 1s, and Ti 2p signals in TiO<sub>2</sub> calculated by using the TPP2M formula<sup>[55]</sup> were 7.2, 6.0, 6.7, and 6.4 nm, respectively. Thus, the XPS signal was expected to be collected exclusively from the 30 nm thick titania thin film without contributions from the substrate.

### XRD of the Titania Films

The phase structure of the titania films was defined by XRD (Panalytical Empyrean multipurpose diffractometer) with Cu Kα radiation (*λ* = 1.5405 Å) and a cathode voltage and current of 45 kV and 40 mA, respectively. The samples were scanned over 2θ = 20°–90° with a step size of 0.01° min<sup>-1</sup> and step duration of 24 s/step.

### Ellipsometry of Titania/n-Si(100)(P)

The growth rate, film thickness, and refractive index of the ALD grown titania layer on n-Si(100)(P) reference was determined by Rudolph AutoEL III Null ellipsometer operated by a He/Ne laser at *λ* = 632.8 nm. The parameters utilized in ellipsometry were as follows: substrate index of Si, *n*<sub>s</sub> = 3.863; substrate extinction coefficient of Si, *k*<sub>s</sub> = 0.162; angle of incidence, 70°; and approximate film index of titania, *n*<sub>t</sub> = 2.3.

### SEM Analyses

Field-emission (FE) SEM images were recorded with a Carl Zeiss Ultra 55 instrument operated at 1 kV/5 kV in in-lens mode.



## Solar Cell Assembly and Characterization

Solar cells were assembled according to a simplified version of a method published elsewhere.<sup>[56]</sup> The calcined TiO<sub>2</sub> web electrodes were stained for 16 h in a 0.1 mM solution of N719 (Ruthenizer 535-bisTBA from Solaronix) dye prepared in acetonitrile/*tert*-butanol 1:1 (v/v). Platinum counter electrode was prepared by depositing a drop of 5 mM H<sub>2</sub>PtCl<sub>6</sub> in ethanol on a cleaned FTO substrate and then heating it at 450 °C for 15 min. The electrolyte was composed of 0.6 M 1,3-dimethyl-imidazolium iodide, 0.03 M diiodine, 0.1 M guanide thiocyanate, and 0.5 M 4-*tert*-butylpyridine in a 85:15 (v/v) mixture of acetonitrile and valeronitrile. The electrodes were sealed together by using a 25 µm thick hot-melt sealing film shaped to a frame and the holes in the counter electrode were covered by using the hot-melt film and a piece of a microscope glass. The *IV* curves of the prepared solar cells were measured by using an Agilent E5272A source measurement unit under simulated 1 sun illumination that was set with a certified reference solar cell from Oriol Instruments. The light source was a 450 W Xe lamp, with a  $\lambda = 315 \pm 710$  nm bandpass filter (KG-3 from Schott) in front of the solar cells.

## Acknowledgements

This research was supported by the Finnish Funding Agency for Innovation TEKES (Dnro 2294/31/2012), National Doctoral Programme in Nanoscience (NGS-NANO), Fortum Foundation, FP7 project SOLAROGENIX (NMP4-SL-2012-310333), Academy of Finland (decision numbers 141481 and 286713), and Padova University ex-60% 2013/2016 projects. We would also like to thank Antti Siiskonen for taking photographs.

**Keywords:** photochemistry ☞ surface analysis ☞ templated synthesis ☞ thin films ☞ titanium

[1] T. M. Brown, F. De Rossi, F. Di Giacomo, G. Mincuzzi, V. Zardetto, A. Reale, A. Di Carlo, *J. Mater. Chem. A* **2014**, *2*, 10788–10817.  
[2] Y. Hu, X. Sun, *J. Mater. Chem. A* **2014**, *2*, 10712–10738.  
[3] M.-H. Sun, S.-Z. Huang, L.-H. Chen, Y. Li, X.-Y. Yang, Z.-Y. Yuan, B.-L. Su, *Chem. Soc. Rev.* **2016**, *45*, 3479–3563.  
[4] B. Liu, L.-M. Liu, X.-F. Lang, H.-Y. Wang, X. W. Lou, E. S. Aydil, *Energy Environ. Sci.* **2014**, *7*, 2592–2597.  
[5] S. Liu, Z. Wang, C. Yu, H. B. Wu, G. Wang, Q. Dong, J. Qiu, A. Eychmüller, X. W. Lou, *Adv. Mater.* **2013**, *25*, 3462–3467.  
[6] Z. Wang, L. Zhou, X. W. Lou, *Adv. Mater.* **2012**, *24*, 1903–1911.  
[7] G. Zhang, H. B. Wu, T. Song, U. Paik, X. W. Lou, *Angew. Chem. Int. Ed.* **2014**, *53*, 12590–12593; *Angew. Chem.* **2014**, *126*, 12798–12801.  
[8] X.-Y. Yu, H. B. Wu, L. Yu, F.-X. Ma, X. W. Lou, *Angew. Chem. Int. Ed.* **2015**, *54*, 4001–4004; *Angew. Chem.* **2015**, *127*, 4073–4076.  
[9] Z. Wang, Z. C. Wang, S. Madhavi, X. W. Lou, *Chem. Eur. J.* **2012**, *18*, 7561–7567.  
[10] I.-D. Kim, A. Rothschild, D.-J. Yang, H. L. Tuller, *Sens. Actuators B* **2008**, *130*, 9–13.  
[11] H. G. Moon, Y.-S. Shim, H. W. Jang, J.-S. Kim, K. J. Choi, C.-Y. Kang, J.-W. Choi, H.-H. Park, S.-J. Yoon, *Sens. Actuators B* **2010**, *149*, 116–121.  
[12] K. An, T. Hyeon, *Nano Today* **2009**, *4*, 359–373.  
[13] D. Fattakhova-Rohlfing, A. Zaleska, T. Bein, *Chem. Rev.* **2014**, *114*, 9487–9558.  
[14] B. Y. Guan, L. Yu, J. Li, X. W. Lou, *Sci. Adv.* **2016**, *2*, e1501554.  
[15] E. Ghadiri, N. Taghavinia, S. M. Zakeeruddin, M. Grätzel, J. E. Moser, *Nano Lett.* **2010**, *10*, 1632–1638.  
[16] J. T. Korhonen, P. Hiekkataipale, J. Malm, M. Karppinen, O. Ilkka, R. H. A. Ras, *ACS Nano* **2011**, *5*, 1967–1974.

[17] A. Ivanova, D. Fattakhova-Rohlfing, B. E. Kayaalp, J. Rathousky, T. Bein, *J. Am. Chem. Soc.* **2014**, *136*, 5930–5937.  
[18] Z. Li, C. Yao, Y. Yu, Z. Cai, X. Wang, *Adv. Mater.* **2014**, *26*, 2262–2267.  
[19] M. Leskelä, M. Ritala, *Angew. Chem. Int. Ed.* **2003**, *42*, 5548–5554; *Angew. Chem.* **2003**, *115*, 5706–5713.  
[20] Y. Gao, H. Jin, Q. Lin, X. Li, M. M. Tavakoli, S.-F. Leung, W. M. Tang, L. Zhou, H. L. W. Chan, Z. Fan, *J. Mater. Chem. A* **2015**, *3*, 10199–10204.  
[21] K. C. Kwon, S. Choi, K. Hong, C. W. Moon, Y.-S. Shim, D. H. Kim, T. Kim, W. Sohn, J.-M. Jeon, C.-H. Lee, K. T. Nam, S. Han, S. Y. Kim, H. W. Jang, *Energy Environ. Sci.* **2016**, *9*, 2240–2248.  
[22] X. Wang, M. Xi, H. Fong, Z. Zhu, *ACS Appl. Mater. Interfaces* **2014**, *6*, 15925–15932.  
[23] X. Li, T. Fan, H. Zhou, S.-K. Chow, W. Zhang, D. Zhang, Q. Guo, H. Ogawa, *Adv. Funct. Mater.* **2009**, *19*, 45–56.  
[24] X. Chen, D.-H. Kuo, D. Lu, *Chem. Eng. J.* **2016**, *295*, 192–200.  
[25] G. K. Hyde, S. M. Stewart, G. Scarel, G. N. Parsons, C.-C. Shih, C.-M. Shih, S.-J. Lin, Y.-Y. Su, N. A. Monteiro-Riviere, R. Narayan, *Biotechnol. J.* **2011**, *6*, 213–223.  
[26] A. K. Chandiran, P. Comte, R. Humphry-Baker, F. Kessler, C. Yi, M. K. Nazeeruddin, M. Grätzel, *Adv. Funct. Mater.* **2013**, *23*, 2775–2781.  
[27] E. Dickey, W. A. Barrow, *J. Vac. Sci. Technol. A* **2012**, *30*, 021502.  
[28] M. B. M. Mousa, C. J. Oldham, G. N. Parsons, *ACS Appl. Mater. Interfaces* **2015**, *7*, 19523–19529.  
[29] S. Zhang, K. Y. Wang, T.-S. Chung, H. Chen, Y. C. Jean, G. Amy, *J. Membr. Sci.* **2010**, *360*, 522–535.  
[30] C. Jin, B. Liu, Z. Lei, J. Sun, *Nanoscale Res. Lett.* **2015**, *10*, 95.  
[31] A. K. Chandiran, A. Yella, M. Stefiik, L.-P. Heiniger, P. Comte, M. K. Nazeeruddin, M. Grätzel, *ACS Appl. Mater. Interfaces* **2013**, *5*, 3487–3493.  
[32] T. W. Hamann, A. B. F. Martinson, J. W. Elam, M. J. Pellin, J. T. Hupp, *J. Phys. Chem. C* **2008**, *112*, 10303–10307.  
[33] W.-M. Jin, J.-H. Shin, C.-Y. Cho, H.-J. Kang, J. H. Park, J. H. Moon, *ACS Appl. Mater. Interfaces* **2010**, *2*, 2970–2973.  
[34] A. B. F. Martinson, J. W. Elam, J. Liu, M. J. Pellin, T. J. Marks, J. T. Hupp, *Nano Lett.* **2008**, *8*, 2862–2866.  
[35] C. Di Valentin, G. Pacchioni, A. Selloni, S. Livraghi, E. Giamello, *J. Phys. Chem. B* **2005**, *109*, 11414–11419.  
[36] N. Shi, X. Li, T. Fan, H. Zhou, J. Ding, D. Zhang, H. Zhu, *Energy Environ. Sci.* **2011**, *4*, 172–180.  
[37] J. Lynch, C. Giannini, J. K. Cooper, A. Lojudice, I. D. Sharp, R. Buonsanti, *J. Phys. Chem. C* **2015**, *119*, 7443–7452.  
[38] National Institute of Standards and Technology: Gaithersburg, NIST X-ray Photoelectron Spectroscopy Database, Version 4.1, <http://srdata.nist.gov/xps/>, **2012**.  
[39] *The XPS of Polymers Database* (G. Beamson, D. Briggs), SurfaceSpectra, **2000**; <https://surfacespectra.com/xps/>.  
[40] S. J. Kim, V.-S. Dang, K. Xu, D. Barreca, C. Maccato, G. Carraro, R. K. Bhakta, M. Winter, H.-W. Becker, D. Rogalla, C. Sada, R. A. Fischer, A. Devi, *Phys. Status Solidi A* **2015**, *212*, 1563–1570.  
[41] N. C. Saha, H. G. Tompkins, *J. Appl. Phys.* **1992**, *72*, 3072–3079.  
[42] M. Sathish, B. Viswanathan, R. P. Viswanath, C. S. Gopinath, *Chem. Mater.* **2005**, *17*, 6349–6353.  
[43] J. L. Gole, J. D. Stout, C. Burda, Y. Lou, X. Chen, *J. Phys. Chem. B* **2004**, *108*, 1230–1240.  
[44] X. Chen, C. Burda, *J. Phys. Chem. B* **2004**, *108*, 15446–15449.  
[45] R. Asahi, T. Morikawa, T. Ohwaki, K. Aoki, Y. Taga, *Science* **2001**, *293*, 269–271.  
[46] B. O'Regan, M. Grätzel, *Nature* **1991**, *353*, 737–740.  
[47] J. Nelson, R. E. Chandler, *Coord. Chem. Rev.* **2004**, *248*, 1181–1194.  
[48] S. A. Haque, Y. Tachibana, R. L. Willis, J. E. Moser, M. Grätzel, D. R. Klug, J. R. Durrant, *J. Phys. Chem. B* **2000**, *104*, 538–547.  
[49] M. Gericke, J. Trygg, P. Fardim, *Chem. Rev.* **2013**, *113*, 4812–4836.  
[50] A. Lee, J. W. Elam, S. B. Darling, *Environ. Sci. Water Res. Technol.* **2016**, *2*, 17–42.  
[51] M. T. McDowell, M. F. Lichterman, A. I. Carim, R. Liu, S. Hu, B. S. Brunschwig, N. S. Lewis, *ACS Appl. Mater. Interfaces* **2015**, *7*, 15189–15199; PMID: 26083827.  
[52] K. Lahtonen, M. Lampimäki, P. Jussila, M. Hirsimäki, M. Valden, *Rev. Sci. Instrum.* **2006**, *77*, 083901.  
[53] N. Fairley, CasaXPS: Spectrum Processing Software for XPS, AES and SIMS, Version 2.3.16 PR 1.6, Casa Software, Cheshire, **2009**; <http://www.casaxps.com/>.

[54] J. H. Scofield, *J. Electron Spectrosc. Relat. Phenom.* **1976**, 8, 129<sup>2</sup> 137.

[55] S. Tanuma, C. J. Powell, D. R. Penn, *Surf. Interface Anal.* **1994**, 21, 165<sup>2</sup> 176.

[56] S. Ito, T. N. Murakami, P. Comte, P. Liska, C. Grätzel, M. K. Nazeeruddin, M. Grätzel, *Thin Solid Films* **2008**, 516, 4613<sup>2</sup> 4319.

---

Manuscript received: August 23, 2016

Revised: October 12, 2016

Accepted Article published: November 2, 2016

Final Article published: November 16, 2016

---

## II

### Design aspects of all atomic layer deposited $\text{TiO}_2\text{-Fe}_2\text{O}_3$ scaffold-absorber photoanodes for water splitting

by

Arto Hiltunen, Tero-Petri Ruoko, Tomi Iivonen, Kimmo Lahtonen, Harri  
Ali-Löytty, Essi Sarlin, Mika Valden, Markku Leskelä and Nikolai Tkachenko

Sustainable Energy Fuels, **2018**, 2, 2124-2130

Reproduced by permission of The Royal Society of Chemistry

Cite this: *Sustainable Energy Fuels*,  
2018, 2, 2124

# Design aspects of all atomic layer deposited TiO<sub>2</sub>–Fe<sub>2</sub>O<sub>3</sub> scaffold-absorber photoanodes for water splitting†

Arto Hiltunen,<sup>a\*</sup> Tero-Petri Ruoko,<sup>a</sup> Tomi Iivonen,<sup>b</sup> Kimmo Lahtonen,<sup>c</sup> Harri Ali-Löytty,<sup>c</sup> Essi Sarlin,<sup>d</sup> Mika Valden,<sup>c</sup> Markku Leskelä<sup>b</sup> and Nikolai Tkachenko<sup>b</sup>

Iron and titanium oxides have attracted substantial attention in photoelectrochemical water splitting applications. However, both materials suffer from intrinsic limitations that constrain the final device performance. In order to overcome the limitations of the two materials alone, their combination has been proposed as a solution to the problems. Here we report on the fabrication of an atomic layer deposited (ALD) Fe<sub>2</sub>O<sub>3</sub> coating on porous ALD-TiO<sub>2</sub>. Our results show that successful implementation requires complete mixing of the TiO<sub>2</sub> and Fe<sub>2</sub>O<sub>3</sub> layers *via* annealing resulting in the formation of a photoactive iron titanium oxide on the surface. Moreover, we found that incomplete mixing leads to crystallization of Fe<sub>2</sub>O<sub>3</sub> to hematite that is detrimental to the photoelectrochemical performance. IPCE and transient photocurrent measurements performed using UV and visible light excitation confirmed that the iron titanium oxide extends the photocurrent generation to the visible range. These measurements were complemented by transient absorption spectroscopy (TAS), which revealed a new band absent in pristine hematite or anatase TiO<sub>2</sub> that we assign to charge transfer within the structure. Taken together, these results provide design guidelines to be considered when aiming to combine TiO<sub>2</sub> and Fe<sub>2</sub>O<sub>3</sub> for photoelectrochemical applications.

Received 31st May 2018  
Accepted 24th July 2018  
DOI: 10.1039/c8se00252e  
rsc.li/sustainable-energy

## 1 Introduction

Photoelectrochemical hydrogen production from water could provide a clean and inexhaustible source of energy if successfully realized on a large scale.<sup>1</sup> For this reason, it has attracted wide interest among researchers ever since the pioneering reports on the topic were published.<sup>2,3</sup> Efficient photoelectrochemical water splitting has high demands on the material properties, which have proven to be difficult task to combine all in only one semiconductor. Therefore, a solution to the problem has been sought from material combinations.

One strategy to combine two materials is to divide the functions of light absorption and charge transport between an absorber and a high surface area scaffold similarly to dye-sensitized solar cells.<sup>4</sup> The scaffolding approach (also known

as the host-scaffold/guest-absorber approach) was first demonstrated in water splitting by Sivula *et al.* where a 60 nm thick hematite layer was deposited on nanostructured WO<sub>3</sub>.<sup>4</sup> Later, demonstrations of a 25 nm thick hematite layer on TiS<sub>2</sub> nanonets, a 5 nm thick layer on ZnO nanorods,<sup>5</sup> and a few nanometer thick hematite coating on porous ZnO<sup>6</sup> have been reported. The suitability of TiO<sub>2</sub> as a scaffold for hematite has been studied previously despite the unfavorable band alignment for electron injection. Successful combining of the good electron transport properties of TiO<sub>2</sub> and light absorption of iron oxide holds great promise for efficient solar water splitting with safe, abundant and stable materials.

Successful implementation of hematite on TiO<sub>2</sub> has been reported to require an underlayer (Nb<sub>2</sub>O<sub>5</sub>),<sup>7</sup> while at the same time successful realization without an underlayer has also been reported.<sup>8</sup> Moreover, annealing the TiO<sub>2</sub> with Fe<sub>2</sub>O<sub>3</sub> to create a thin Fe<sub>2</sub>TiO<sub>5</sub> layer on the surface has been proposed to be the mechanism to reach high photocurrents.<sup>9</sup> Therefore, the varying experimental results implies that the question of how to combine TiO<sub>2</sub> and Fe<sub>2</sub>O<sub>3</sub> in the scaffold/absorber configuration requires further clarification. Furthermore, a recent review tells that the working principles of the Fe<sub>2</sub>O<sub>3</sub>-TiO<sub>2</sub> heterojunction devices still remain unclear and suggests further investigation on this promising topic.<sup>10</sup>

The aim of this paper is to establish whether TiO<sub>2</sub> is a suitable scaffold for Fe<sub>2</sub>O<sub>3</sub> in the scaffold/absorber configuration.

<sup>a</sup>Laboratory of Chemistry and Bioengineering, Tampere University of Technology, P.O. Box 541, FI-33101 Tampere, Finland. E-mail: arto.j.hiltunen@tut.fi

<sup>b</sup>Department of Chemistry, University of Helsinki, P.O. Box 55, FI-00014 Helsinki, Finland

<sup>c</sup>Surface Science Group, Laboratory of Photonics, Tampere University of Technology, P.O. Box 692, FI-33101 Tampere, Finland

<sup>d</sup>Laboratory of Materials Science, Tampere University of Technology, P.O. Box 589, 33101 Tampere, Finland

† Electronic supplementary information (ESI) available: Additional SEM image, XPS data, XRD diffractograms, IV-curves, IPCE, and TAS spectra. See DOI: 10.1039/c8se00252e

To answer this question, we applied 100, 200 and 400 atomic layer deposition (ALD) cycles of  $\text{Fe}_2\text{O}_3$  on porous  $\text{TiO}_2$ . The thicknesses correspond nominally to 5, 10 and 20 nanometers. The composite materials were characterized by scanning electron microscopy (SEM), transmission electron microscopy (TEM), X-ray photoelectron spectroscopy (XPS), Raman spectroscopy, X-ray diffraction (XRD), and they were tested as anodes in a photoelectrochemical (PEC) water splitting cell. The steady-state PEC experiments were complemented by transient absorption (TAS) and transient photocurrent (TPC) measurements to gain insight into the water oxidation dynamics.

Our results show that an annealing step which creates a thin FeTi-oxide layer on the surface is necessary for successful device operation. Importantly, we find that crystallization of ALD- $\text{Fe}_2\text{O}_3$  to hematite will lead to reduced photocurrent once hematite begins to dominate the surface. The growth of hematite can be avoided by using a low number of ALD cycles. For our device architecture, we discover that 100 ALD-cycles is sufficient to increase the absorption of the photoanode without significant hematite crystal growth.

The results presented herein provide new insight into the fabrication of porous  $\text{TiO}_2/\text{Fe}_2\text{O}_3$  photoanodes with the scaffold/absorber technique by clarifying the surface science of the material composition from the perspective of solar water splitting. While this study was carried out by the means of ALD the here presented phenomena and the design principles derived from them are applicable to other fabrication techniques as well.

## 2 Results and discussion

The  $\text{TiO}_2$  scaffolds used in this work were fabricated according to a previously published method of ALD on cellulose substrates.<sup>11</sup> The resulting weblike  $\text{TiO}_2$  structure was selected to this study for its large pore size allowing easy penetration of ALD precursors. SEM and TEM images of the  $\text{TiO}_2$  scaffolds coated with 100, 200 and 400 cycles of ALD- $\text{Fe}_2\text{O}_3$  after annealing are presented in Fig. 1 (see Fig. S1† for a zoomed-out image). TEM images show the hollow tubular structure of the  $\text{TiO}_2$  scaffold on top of which the ALD- $\text{Fe}_2\text{O}_3$  grow. Based on the SEM images, the application of 100 and 200 iron oxide deposition cycles was found to form individual islands which cover the  $\text{TiO}_2$  scaffolds throughout. The islands are present already prior to annealing. Increasing the cycle number resulted in increased island sizes that grow large enough to coalesce together.

X-ray photoelectron spectroscopy was implemented to further characterize the surface of the structure. Table 1 shows the relative elemental concentrations of Ti, Fe and O for the  $\text{TiO}_2$  sample with 100 cycles of ALD- $\text{Fe}_2\text{O}_3$  coating. Upon annealing at 680 °C the Ti/Fe ratio increases from 1.16 to 2.03, which indicates diffusion of Ti towards the surface. Furthermore, annealing increases the Fe 2p and Ti 2p peak separation by 0.3 eV (Ti 2p peak shifts to lower binding energy), which can be assigned to the formation of a mixed FeTi-oxide. In the studied samples, titanium was found to have oxidation state  $\text{Ti}^{4+}$  and iron  $\text{Fe}^{3+}$  suggesting the formation of a  $\text{Fe(III)Ti(IV)}$

oxide. A similar peak shift has been previously observed and associated to the formation of amorphous  $\text{Fe}_x\text{Ti}_{1-x}\text{O}_y$ , where a thin  $\text{TiO}_2$  coating was deposited over  $\text{Fe}_2\text{O}_3$  nanorods.<sup>12</sup> The XPS spectra for Fe 2p and Ti 2p energy regions are given in the ESI (Fig. S2†). No Sn was detected on the surface, while the diffusion of tin originating from the underlying FTO has been reported to occur upon annealing at high temperatures.<sup>13</sup>

X-ray diffraction (XRD) was used to identify the crystal structures. As XRD is a bulk characterization method, all samples indicated crystalline  $\text{SnO}_2$  from the substrate and anatase  $\text{TiO}_2$ . In the as-deposited condition, the existence of hematite was visible for the sample with 400 ALD cycles, as indicated by its highest intensity {104} peak at 33.3° (see Fig. S3† for the diffractogram). The hematite signal was not detected for the 100 or 200 cycle samples suggesting an amorphous structure. Even though ALD metal oxide films obtained at high temperatures are usually crystalline as-deposited, ultra-thin films (<5 nm) regularly remain amorphous until a critical film thickness value is reached.<sup>14</sup> Upon annealing, the high intensity peak of hematite at 33.3° is intensified for the 400 cycles sample which suggests increased degree of crystallinity in the hematite layers compared to the non-annealed ones. Hematite was found in the annealed 100 and 200 cycle samples only in trace amounts.

Raman spectroscopy was used as a complementary experiment to study the annealed samples in more detail. The  $\text{TiO}_2$  scaffold shows typical anatase signal peaks at 144, 197, 395, 515 and 636  $\text{cm}^{-1}$ .<sup>15</sup> The hematite peaks<sup>16</sup> at 244, 291, 297, 410, 499, 610  $\text{cm}^{-1}$  become clearly visible only after the coating thickness increases up to 400 cycles (Fig. 2). For the 100 and 200 cycle coatings the hematite signal is weak indicating that only a minor amount of ALD- $\text{Fe}_2\text{O}_3$  crystallized to hematite being in line with the XRD results. The LO (longitudinal optical mode) peak at 660  $\text{cm}^{-1}$ , which was observed only for the 400 cycle coated sample, has been assigned to disorder within the hematite lattice.<sup>17</sup> The appearance of this peak has been also previously observed to appear for high temperature (650 °C) annealed  $\text{Fe}_2\text{O}_3$ - $\text{TiO}_2$  systems and assigned to a reaction between hematite and  $\text{TiO}_2$ .<sup>12</sup> This peak is not detected for the 100 and 200 cycle samples as the hematite signal itself is barely visible.

Fig. 3 shows IV-curves for  $\text{TiO}_2$  scaffold coated with ALD- $\text{Fe}_2\text{O}_3$  along with the bare weblike  $\text{TiO}_2$  scaffold for comparison. The IV-curves are measured after annealing at 680 °C, which was found to be prerequisite for obtaining reasonable photocurrent from the ALD- $\text{Fe}_2\text{O}_3$  coated samples (see Fig S4† for the IV-curves of as-deposited samples). The  $\text{TiO}_2$ -web shows an IV-curve with photocurrent in the same order of magnitude that has been previously reported for cellulose templated porous ALD- $\text{TiO}_2$ .<sup>18</sup> This allows us to conclude that the web worked as expected and provided a suitable platform for the ALD- $\text{Fe}_2\text{O}_3$  coatings.

For the ALD- $\text{Fe}_2\text{O}_3$  samples we found out that the 100 and 200 cycle coatings gave significantly higher photocurrent than the thicker 400 cycle coating. Based on the results obtained by Raman spectroscopy and XRD we can see that the drop of the photocurrent is caused by the crystallization of ALD- $\text{Fe}_2\text{O}_3$  into

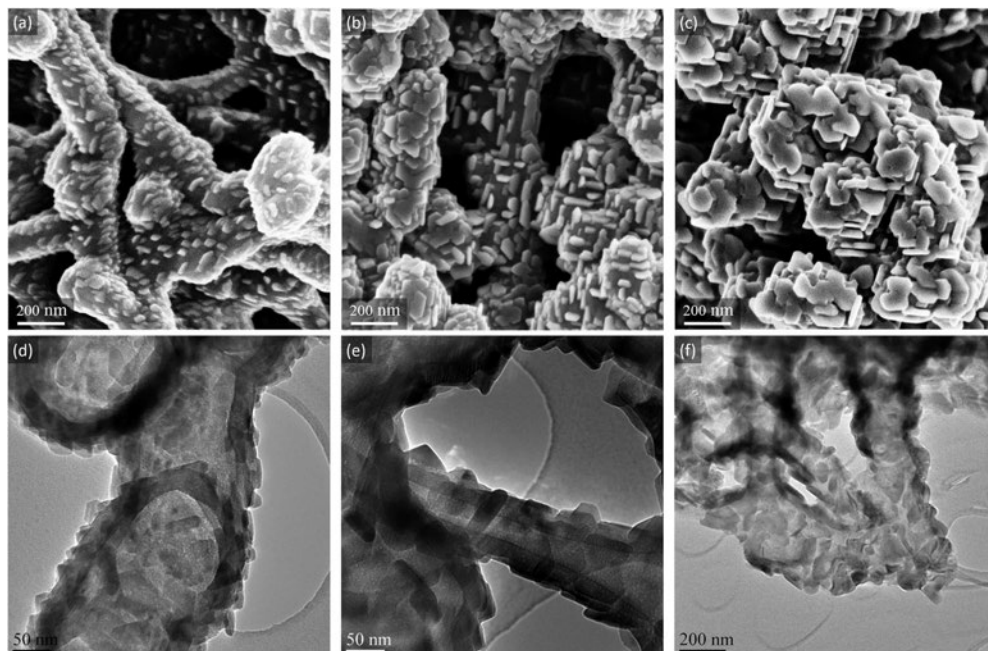


**Fig. 1** (a–c) SEM images of a  $\text{TiO}_2$  scaffold coated with 100, 200, and 400 cycles of ALD- $\text{Fe}_2\text{O}_3$ , respectively. Images (d–f) are TEM images of the corresponding samples.

hematite (see Fig. 2 & 3). This is in accordance with the observation noted previously by Sivula *et al.*<sup>4</sup> and Stefik *et al.*<sup>7</sup> that hematite overlayers on titania results in no photocurrent. This indeed is expected as hematite has a conduction band edge below that of titania, creating an injection barrier for the electrons photogenerated in the hematite layer.<sup>7,19</sup> The photoelectrochemical performance of our materials closely matches those published earlier for  $\text{Fe}_x\text{-TiO}_2$  photoanodes prepared *via* sol-gel.<sup>20</sup>

The XPS analysis indicated the formation of an FeTi-oxide layer on the surface upon annealing. When the ALD- $\text{Fe}_2\text{O}_3$  cycle number is kept low, in our case 200 or below, the mixing of ALD- $\text{Fe}_2\text{O}_3$  with Ti during annealing is complete resulting in FeTi-oxide on the surface. This explains why the 100 & 200 cycle

coated samples overperform the 400 cycle coated sample, where part of the ALD- $\text{Fe}_2\text{O}_3$  film crystallizes as hematite. Previously, a  $\text{Fe}_2\text{TiO}_5$  (pseudobrookite) layer has been synthesized on  $\text{TiO}_2$  nanotubes by high temperature annealing of electrodeposited  $\text{Fe}_2\text{O}_3$ .<sup>9</sup> More frequently, however, the  $\text{Fe}_2\text{TiO}_5$  has been designed to inject electrons to hematite<sup>12,21–23</sup> in contrast to what we report here.

Han *et al.*<sup>24</sup> noted on the importance of not covering the whole  $\text{TiO}_2$  substrate with hematite in their system where the photoactive material was the  $\text{TiO}_2$ . Our system is significantly different as the photoactive material is the mixed FeTi-oxide. To prove that the improved efficiency stems from the increased spectral response, originating from the mixed oxide, incident photon-to-current-efficiency (IPCE) was measured. As expected,

**Table 1** Relative surface concentrations and core level binding energies (BE) of Ti, Fe and O for  $\text{TiO}_2$  scaffold coated with 100 cycles of  $\text{Fe}_2\text{O}_3$ . The BE scale was calibrated according to the C 1s C–C/H component at 285.0 eV. The relative surface concentrations of all the detected elements including adventitious C and traces of N, Ca, Na, Mg and Si are shown in the ESI (Table S1)

Sample	Concentration, at% (XPS peak position, eV)				
	Fe 2p <sub>3/2</sub>	Ti 2p <sub>3/2</sub>	O 1s	Ti/Fe	$\Delta(\text{Fe } 2\text{p}_{3/2}\text{-Ti } 2\text{p}_{3/2})$
As-deposited	11.69 (710.62)	13.53 (458.84)	74.78 (530.07)	1.16	(251.78)
Annealed	7.44 (710.53)	15.07 (458.43)	77.49 (529.78)	2.03	(252.10)

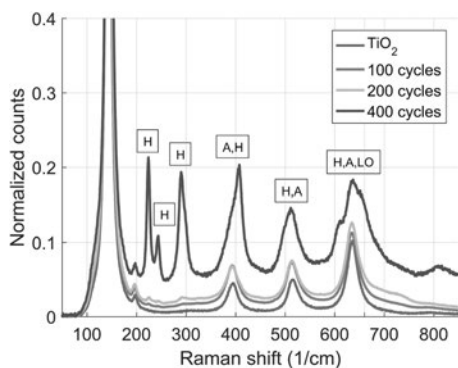


Fig. 2 Raman spectra of  $\text{TiO}_2$  scaffold with varying thickness of ALD- $\text{Fe}_2\text{O}_3$  coating. H: hematite, A: anatase, LO: longitudinal optical mode.

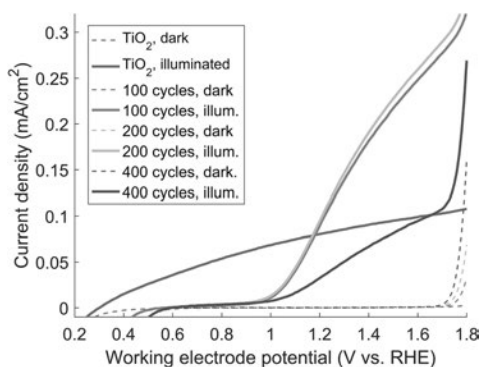


Fig. 3 IV-curves of the studied samples.

the bare  $\text{TiO}_2$  gives rise to photocurrent only with UV excitation, and no signal with visible light excitation due to the large band gap of the material. However, upon coating of the  $\text{TiO}_2$  electrode with ALD- $\text{Fe}_2\text{O}_3$  followed by annealing, the spectral response is observed to extend into the visible range up to 600 nm. The IPCE of the hematite containing sample (400 cycles) is reduced compared to the 100 & 200 cycle samples, because hematite cannot contribute to the photocurrent due to the conduction band misalignment. The IPCE spectra are given in the ESI† along with UV-Vis absorption spectra of the materials Fig. S5a and b.†

Transient photocurrent (TPC) decays, measured with UV (355 nm) and visible light (410 nm) laser excitation, complement the steady-state IPCE measurements. The TPC experiment measures the decay of the photocurrent signal created by the laser excitation. The signal is a sum of two decay pathways: the electron-hole recombination and the electron extraction by the external circuit.<sup>25,26</sup> Fig. 4 shows TPC decays for bare  $\text{TiO}_2$  and

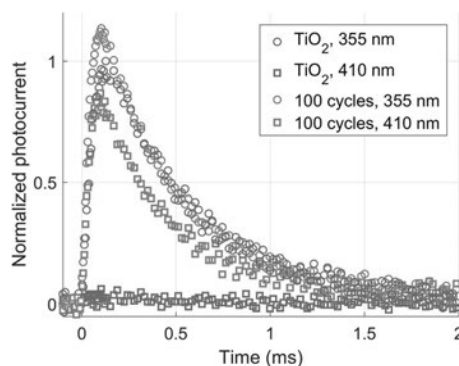


Fig. 4 Photocurrent decays of the ALD- $\text{Fe}_2\text{O}_3$  sensitized (100 cycles, annealed)  $\text{TiO}_2$  electrodes and the reference  $\text{TiO}_2$  scaffold. Decays are normalized relative to the  $\text{TiO}_2$  355 nm signal.

$\text{FeTi}$ -oxide normalized relative to the  $\text{TiO}_2$  355 nm signal. All the presented decays have similar kinetics, which imply that the aforementioned processes are not significantly altered by the coating within the resolution of the experiment. This similarity of the decay curves is evidence that the  $\text{FeTi}$ -oxide layer is able to inject electrons to the  $\text{TiO}_2$  network through which the charges diffuse to the FTO contact.

The charge carrier recombination dynamics were studied in the ps–ns timescale using transient absorption spectroscopy of annealed planar 200 cycles ALD- $\text{Fe}_2\text{O}_3$  samples deposited on FTO and  $\text{TiO}_2$  coated FTO. The 200 cycle sample was selected for the study to achieve high enough absorbance on the planar samples. The excitation wavelength was set to 410 nm to selectively excite only the ALD- $\text{Fe}_2\text{O}_3$  overlayer. In this time-scale the transient absorption is composed of a superposition of the absorptions of both photoexcited holes and electrons.

The negative transient absorption band below 450 nm is due to the bleaching of the ground state absorption. The strong positive absorption band centered at 570–580 nm in the bare hematite sample has previously been assigned to the absorption of photoexcited electrons.<sup>27</sup> However, recent investigations of hematite photoanodes under applied bias voltages have revealed a positive absorption at the same wavelength that is formed due to high valent iron-oxo species.<sup>28,29</sup> We have previously observed that a bias dependent bleaching of this absorption occurs due to electron transfer into oxidised surface states.<sup>30</sup> Thus, we conclude that this absorption band is most probably due to photoexcited holes in the hematite bulk. The decay of the photoexcited electrons is a multiexponential process dominated by recombination and electron trapping.<sup>30</sup> The decay of the TAS signal was best fit with three exponential functions with lifetimes of 0.29, 17, and 320 ps (Fig. S6a–c & Table S2†).

The transient absorption spectrum of the ALD- $\text{Fe}_2\text{O}_3$  sample deposited on top of  $\text{TiO}_2$  and annealed at 680 °C shows the formation of a new broad positive absorption band between

450–680 nm (see Fig. 5b). Neither bare hematite or  $\text{TiO}_2$  (Fig. S6d†) show a positive transient absorption below 535 nm. Additionally, the globally fitted three exponential decay of the TAS signal now has lifetimes of 0.26, 4.7, and 320 ps. The fastest and slowest components of the decay match those for the bare hematite sample, whereas the middle component is now significantly faster. We determine this new positive absorption band to indicate that electrons have been transferred to the  $\text{TiO}_2$  layer. The transfer of electrons between the layers explains the faster decay component, and the positive transient absorption spanning from 450 to 680 nm is assigned to the free electrons transferred to the  $\text{TiO}_2$  layer.<sup>31</sup> Interestingly, the ground state bleach observed for the bare hematite sample below 450 nm is not visible for the sample deposited on top of  $\text{TiO}_2$ . This can be due to the transfer of conduction band electrons away from the FeTi-oxide layer leading to the ground state bleach disappearing, further supporting our determination of the electron transfer occurring through the mixed oxide layer, as indicated by the TPC results. Typically, electron transfer between unmixed layers should take place in the picoseconds to nanoseconds timescale. The fact that the change in the TAS spectrum occurs immediately after excitation suggests towards the proposed mixing of the two metal oxide layers.

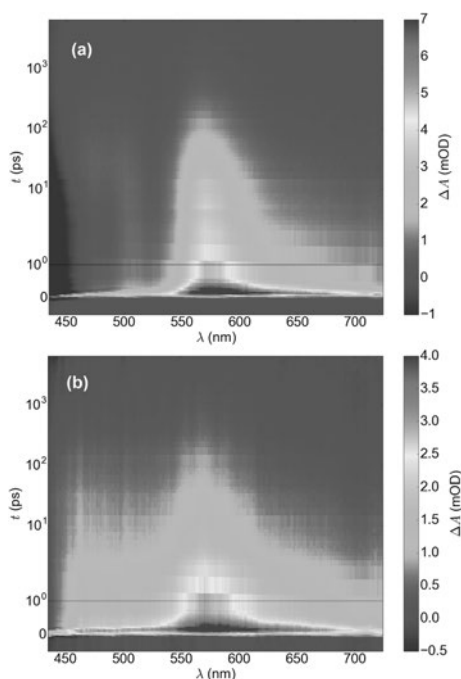


Fig. 5 Transient absorption spectra of (a) hematite and (b) FeTi-oxide. Timescale is linear until 1 ps and logarithmic for longer delay times.

### 3 Conclusions

We have presented a case study on the combination of ALD- $\text{TiO}_2$  and thin ALD- $\text{Fe}_2\text{O}_3$  coating for water splitting purposes in a scaffold/absorber configuration. Our results indicate that the condition for the approach is to induce mixing of the  $\text{Fe}_2\text{O}_3$  and  $\text{TiO}_2$  layers at high temperature, resulting in photoactive  $\text{Fe(III)Ti(IV)}$  oxide on the surface. Furthermore, growth of hematite crystals when a large number of ALD- $\text{Fe}_2\text{O}_3$  cycles was applied resulted in decreased device performance. With 100 and 200 ALD- $\text{Fe}_2\text{O}_3$  cycles crystallization to hematite was avoided, and an increase in the photocurrent over  $\text{TiO}_2$  was achieved. We consider these results as a indication that ALD- $\text{TiO}_2$  and ALD- $\text{Fe}_2\text{O}_3$  is a suitable pair for a host-scaffold/guest-absorber approach when appropriate post-treatments are applied. The tunability of ALD offers vast possibilities for optimization of both the scaffold and coating thicknesses. We propose that follow-up studies should look into applying the same approach on transparent porous  $\text{TiO}_2$  structures, possibly fabricated by the means of nanocelluloses, with even smaller ALD- $\text{Fe}_2\text{O}_3$  cycle number to reveal the full potential of the approach.

### 4 Experimental

#### 4.1 $\text{TiO}_2$ thin film preparation

FTO substrates (TEC 7/2.2, 6–8 ohm  $\text{sq}^{-1}$ , Solems) were cleaned with detergent and water, and subsequently sonicated in water (Milli-Q), acetone and 2-propanol for 15 min in each solvent. A titanium dioxide compact layer was prepared on the cleaned substrates by spin coating from a titanium isopropoxide precursor solution.<sup>32</sup> On these substrates, the porous  $\text{TiO}_2$  structures were built by coating a cellulose scaffold with 30 nm of  $\text{TiO}_2$  using atomic layer deposition. The precursor for the ALD- $\text{TiO}_2$  was tetrakis(dimethylamido)titanium(IV). After ALD the samples were annealed at 450 °C to crystallize the  $\text{TiO}_2$  and remove the cellulose from the structure. The details of the method, including the ALD procedure, have been published previously.<sup>11</sup>

Planar samples for transient absorption measurements were prepared by coating FTO substrates with 30 nm of  $\text{TiO}_2$  using the same ALD procedure as for the cellulose substrates, and annealed at 450 °C. When used as a reference for the ALD- $\text{Fe}_2\text{O}_3$  coated samples, same post-annealings were applied to all.

#### 4.2 Atomic layer deposition of $\text{Fe}_2\text{O}_3$

Hematite thin films were deposited in an F-120 ALD reactor (ASM Microchemistry, Finland) by applying the  $\text{FeCl}_3 + \text{H}_2\text{O}$ -process at 400 °C.<sup>33</sup> At this deposition temperature, the growth rate of the hematite thin films on planar substrates is 0.5 Å per cycle as determined *via* energy dispersive X-ray spectroscopy (EDX) measurements. The EDX spectra were collected using an Oxford INCA 350 microanalysis system connected to a Hitachi S-4800 field emission scanning electron microscope (FESEM). The film thicknesses were calculated from the EDX spectra using the GMRfilm software<sup>34</sup> and assuming a bulk density value of 5.3  $\text{g cm}^{-3}$ .



#### 4.3 Annealing

The high temperature treated samples were annealed at 680 °C for 1 hour using a 20 °C min<sup>-1</sup> heating rate. After annealing the samples were taken out of the oven to room temperature while still hot and let cool down.

#### 4.4 Scanning electron microscopy

Field emission scanning electron microscopy images (FESEM) images were taken with a Carl Zeiss Ultra 55 instrument. Acceleration voltages varied from 1 to 5 kV.

#### 4.5 Transmission electron microscopy

Samples for the transmission electron microscopy study of the structure were prepared by scraping a small amount of the sample in ethanol and casting a drop of the ethanol on a carbon-coated copper grid. After evaporation of ethanol at room temperature, the samples were studied with JEOL TEM 2010 with an acceleration voltage of 200 kV.

#### 4.6 X-ray photoelectron spectroscopy

XPS measurements were performed utilizing a non-monochromatized Al K<sub>α</sub> X-ray source ( $h\nu = 1486.6$  eV) and an Argus hemispherical electron spectrometer (Omicron Nanotechnology GmbH) installed in a multifunctional UHV system with a base pressure below  $1 \times 10^{-10}$  mbar.<sup>35</sup> The surface elemental concentrations and chemical states of compounds were identified by analyzing high-resolution XPS spectra using CasaXPS software (Version 2.3.16 PR 1.6).<sup>36</sup> The binding energy scale was calibrated according to the C 1s C–C/H component at 285.0 eV. After a Shirley-type background subtraction, the peaks were least-squares fitted with a combination of symmetric Gaussian–Lorentzian line shapes. The relative atomic concentrations were calculated using Scofield photoionization cross sections<sup>37</sup> and an experimentally measured transmission function of the Argus analyser.

#### 4.7 X-ray diffraction

The crystal structures were defined by XRD (Panalytical Empyrean multipurpose diffractometer) with Cu K<sub>α</sub> radiation ( $\lambda = 1.5405$  Å) and a cathode voltage and current of 45 kV and 40 mA, respectively. The samples were scanned over  $2\theta = 20$ –90° with a step size of 0.018° and step duration of 19 s per step. The references were ICOD 00-046-1088, ICOD 01-070-6826/ICSD 98-020-2243 and ICSD 98-008-8418 for SnO<sub>2</sub>, TiO<sub>2</sub> and  $\alpha$ -Fe<sub>2</sub>O<sub>3</sub>, respectively.

#### 4.8 Raman spectroscopy

Raman spectra were collected in the backscattering geometry using a confocal Raman microscope equipped with a 532 nm laser source and a 100× objective (NT-MDT Ntegra). The laser power was adjusted to 10 mW at the sample surface using an ND filter. The acquisition time for each measurement was 600 s.

#### 4.9 IV-curves and IPCE

The IV-curves were measured using a three electrode setup having the sample as the working electrode, a platinum counter electrode and a Ag/AgCl reference electrode. 0.1 M NaOH was used as the electrolyte contained in a 1 cm × 5 cm quartz cuvette. The IV-curves were recorded with Agilent E5272A source measure unit under AM1.5G 100 mW cm<sup>-2</sup> (1 Sun) illumination using Sciencetech SS150 – AAA Solar simulator as the light source. The samples were illuminated through the glass substrate. The light intensity was set with a calibrated reference solar cell from Oriol instruments (model 91150V). The photocurrents were scaled relative to the active area of the samples that was typically a 50 mm<sup>2</sup> square. IPCE was measured with the same setup filtering the light through band pass filters (FKB-VIS-40 from Thorlabs, FWHM 40 nm) that were placed in front of the sample.

#### 4.10 UV-Vis absorption

UV-Vis absorption was measured with Shimadzu UV-3600 spectrophotometer. The absorbance was recorded from FTO substrates having a 30 nm ALD-TiO<sub>2</sub> layer on top of which ALD-Fe<sub>2</sub>O<sub>3</sub> (100, 200 or 400 cycles) was deposited, and then subsequently annealed at 680 °C. The reference hematite film was prepared directly on the FTO substrate without the TiO<sub>2</sub> layer.

#### 4.11 Transient photocurrent measurement

The TPC decays were measured with the same three electrode set up described above keeping the working electrode at a potential of 0.5 V vs. Ag/AgCl. A 50 ohm resistor was connected in series with the sample. The sample was excited with laser pulses (355 nm & 410 nm) and the resulting voltage drop over the resistor was measured as a function of time with an oscilloscope (Tektronix TDS 5032B).

#### 4.12 Transient absorption spectroscopy

The transient absorption studies were performed using the femtosecond pump-probe method. The primary laser pulses were obtained with a Ti:Sapphire laser (Libra F, Coherent Inc., 800 nm, 100 fs pulse width, repetition rate 1 kHz). Approximately 90% of the fundamental beam was directed to an optical parametric amplifier (Topas C, Light Conversion Ltd.) to produce the excitation pump pulses at 410 nm with approximately 1 mm beam diameter at the sample, attenuated to 0.65–0.8 mW with neutral density filters with 500 Hz repetition rate. The white light probe pulses were obtained directing the remaining fundamental laser beam energy through a motorized translational stage to a Ti:sapphire crystal for white continuum generation. The measurement system (ExciPro, CDP systems) was equipped with a Si CCD detector. The absorbance changes were averaged 2500 times for each delay time, and the whole measurement sequence was performed four times for each sample to minimize variations caused by possible excitation power fluctuations.

## Conflicts of interest

There are no conflicts to declare.

## Acknowledgements

M. L. and T. I. thank Academy of Finland (Centre of Excellence in Atomic Layer Deposition), and EU-FP7 Grant “G-PHOTO-CAT” (Grant No. 309636). H. A. thanks the Academy of Finland (grant nos 141481, 286713, 310359, and 309920) and the Jenny and Antti Wihuri Foundation. K. L. thanks the Academy of Finland (grant nos 141481 and 286713). A. H. thanks the Finnish Foundation for Technology Promotion. A. H. and T. I. wish to acknowledge the late Dr Leonid Khriachtchev for his assistance in the Raman measurements.

## References

- 1 T. Hisatomi, J. Kubota and K. Domen, *Chem. Soc. Rev.*, 2014, **43**, 7520–7535.
- 2 A. Fujishima and K. Honda, *Nature*, 1972, **238**, 37.
- 3 P. J. Boddy, *J. Electrochem. Soc.*, 1968, **115**, 199.
- 4 K. Sivula, F. L. Formai and M. Grätzel, *Chem. Mater.*, 2009, **21**, 2862–2867.
- 5 Y.-K. Hsu, Y.-C. Chen and Y.-G. Lin, *ACS Appl. Mater. Interfaces*, 2015, **7**, 14157–14162.
- 6 D. Barreca, G. Carraro, A. Gasparotto, C. Maccato, T. Altantzis, C. Sada, K. Kaunisto, T.-P. Ruoko and S. Bals, *Adv. Mater. Interfaces*, 2017, 1700161.
- 7 M. Stefiak, M. Cornuz, N. Mathews, T. Hisatomi, S. Mhaisalkar and M. Grätzel, *Nano Lett.*, 2012, **12**, 5431–5435.
- 8 L. Liu, *Mater. Lett.*, 2015, **159**, 284–288.
- 9 Q. Liu, J. He, T. Yao, Z. Sun, W. Cheng, S. He, Y. Xie, Y. Peng, H. Cheng, Y. Sun, Y. Jiang, F. Hu, Z. Xie, W. Yan, Z. Pan, Z. Wu and S. Wei, *Nat. Commun.*, 2014, **5**, 5122.
- 10 S. Kment, F. Riboni, S. Pausova, L. Wang, L. Wang, H. Han, Z. Hubicka, J. Krysa, P. Schmuki and R. Zboril, *Chem. Soc. Rev.*, 2017, **46**, 3716–3769.
- 11 A. Hiltunen, K. Lahtonen, J. Saari, A. Ojanperä, E. Sarlin, H. Wondraczek, A. Efimov, K. Kaunisto, P. Vivo, C. Maccato, D. Barreca, P. Fardim, N. Tkachenko, M. Valden and H. Lemmetyinen, *ChemPhysChem*, 2017, **18**, 64–71.
- 12 X. Li, P. S. Bassi, P. P. Boix, Y. Fang and L. H. Wong, *ACS Appl. Mater. Interfaces*, 2015, **7**, 16960–16966.
- 13 A. Annamalai, P. S. Shinde, A. Subramanian, J. Y. Kim, J. H. Kim, S. H. Choi, J. S. Lee and J. S. Jang, *J. Mater. Chem. A*, 2015, **3**, 5007–5013.
- 14 V. Mikkulainen, M. Leskelä, M. Ritala and R. Puurunen, *J. Appl. Phys.*, 2013, **113**, 021301.
- 15 B. Lafuente, R. T. Downs, H. Yang and N. Stone, The power of databases: the RRUFF project, in *Highlights in Mineralogical Crystallography*, ed. T. Armbruster and R. M. Danisi, W. De Gruyter, Berlin, Germany, 2015, pp. 1–30.
- 16 B. Lafuente, R. T. Downs, H. Yang and N. Stone, The power of databases: the RRUFF project, in *Highlights in Mineralogical Crystallography*, T. Armbruster and R. M. Danisi, W. De Gruyter, Berlin, Germany, 2015, pp. 1–30.
- 17 A. M. Jubb and H. C. Allen, *ACS Appl. Mater. Interfaces*, 2010, **2**, 2804–2812.
- 18 Z. Li, C. Yao, Y. Yu, Z. Cai and X. Wang, *Adv. Mater.*, 2014, **26**, 2262–2267.
- 19 M. Grätzel, *Nature*, 2011, **414**, 338–344.
- 20 E. Courtin, G. Baldinozzi, M. T. Sougrati, L. Stievano, C. Sanchez and C. Laberty-Robert, *J. Mater. Chem. A*, 2014, **2**, 6567–6577.
- 21 L. Wang, N. T. Nguyen, X. Huang, P. Schmuki and Y. Bi, *Adv. Funct. Mater.*, 2017, **27**, 1703527.
- 22 J. Deng, X. Lv, J. Liu, H. Zhang, K. Nie, C. Hong, J. Wang, X. Sun, J. Zhong and S.-T. Lee, *ACS Nano*, 2015, **9**, 5348–5356.
- 23 D. Monllor-Satoca, M. Bartsch, C. Fabrega, A. Genc, S. Reinhard, T. Andreu, J. Arbiol, M. Niederberger and J. R. Morante, *Energy Environ. Sci.*, 2015, **8**, 3242–3254.
- 24 H. Han, F. Riboni, F. Karlicky, S. Kment, A. Goswami, P. Sudhagar, J. Yoo, L. Wang, O. Tomanec, M. Petr, O. Haderka, C. Terashima, A. Fujishima, P. Schmuki and R. Zboril, *Nanoscale*, 2017, **9**, 134–142.
- 25 B. C. O'Regan and F. Lenzmann, *J. Phys. Chem. B*, 2004, **108**, 4342–4350.
- 26 S. R. Pendlebury, A. J. Cowan, M. Barroso, K. Sivula, J. Ye, M. Grätzel, D. R. Klug, J. Tang and J. R. Durrant, *Energy Environ. Sci.*, 2012, **5**, 6304–6312.
- 27 S. Sorenson, E. Driscoll, S. Haghighat and J. M. Dawlaty, *J. Phys. Chem. C*, 2014, **118**, 23621–23626.
- 28 B. Klahr and T. Hamann, *J. Phys. Chem. C*, 2014, **118**, 10393–10399.
- 29 O. Zandi, A. R. Schon, H. Hajibabaei and T. W. Hamann, *Chem. Mater.*, 2016, **28**, 765–771.
- 30 T.-P. Ruoko, K. Kaunisto, M. Bärtsch, J. Pohjola, A. Hiltunen, M. Niederberger, N. V. Tkachenko and H. Lemmetyinen, *J. Phys. Chem. Lett.*, 2015, **6**, 2859–2864.
- 31 T. Yoshihara, R. Katoh, A. Furube, Y. Tamaki, M. Murai, K. Hara, S. Murata, H. Arakawa and M. Tachiya, *J. Phys. Chem. B*, 2004, **108**, 3817–3823.
- 32 S. Pathak, A. Sepe, A. Sadhanala, F. Deschler, A. Haghighirad, N. Sakai, K. C. Goedel, S. D. Stranks, N. Noel, M. Price, S. Hüttner, N. A. Hawkins, R. H. Friend, U. Steiner and H. J. Snaith, *ACS Nano*, 2015, **9**, 2311–2320.
- 33 J. A. Klug, N. G. Becker, S. C. Riha, A. B. F. Martinson, J. W. Elam, M. J. Pellin and T. Proslir, *J. Mater. Chem. A*, 2013, **1**, 11607–11613.
- 34 R. A. Waldo, *Microbeam Anal.*, 1988, **23**, 310.
- 35 K. Lahtonen, M. Lampimäki, P. Jussila, M. Hirsimäki and M. Valden, *Rev. Sci. Instrum.*, 2006, **77**, 083901.
- 36 N. Fairley, *CasaXPS: Spectrum Processing Software for XPS, AES and SIMS*, Casa Software Ltd., Cheshire, UK, 2009, version 2.3.16 PR 1.6, <http://www.casaxps.com/>.
- 37 J. H. Scofield, *J. Electron Spectrosc. Relat. Phenom.*, 1976, **8**, 129–137.

### III

## Charge carrier dynamics in tantalum oxide overlayered and tantalum doped hematite photoanodes

by

Tero-Petri Ruoko, Arto Hiltunen, Tomi Iivonen, Riina Ulkuniemi, Kimmo Lahtonen, Harri Ali-Löytty, Kenichiro Mizohata, Mika Valden, Markku Leskelä  
and Nikolai V. Tkachenko

J. Mater. Chem. A, **2019**, 7, 3206-3215

Reproduced by permission of The Royal Society of Chemistry



Cite this: *J. Mater. Chem. A*, 2019, **7**, 3206

# Charge carrier dynamics in tantalum oxide overlayers and tantalum doped hematite photoanodes†

Tero-Petri Ruoko,<sup>a</sup> Arto Hiltunen,<sup>a</sup> Tomi Iivonen,<sup>b</sup> Riina Ulkuniemi,<sup>c</sup> Kimmo Lahtonen,<sup>c</sup> Harri Ali-Löytty,<sup>c</sup> Kenichiro Mizohata,<sup>d</sup> Mika Valden,<sup>c</sup> Markku Leskelä<sup>b</sup> and Nikolai V. Tkachenko<sup>a</sup>

We employ atomic layer deposition to prepare 50 nm thick hematite photoanodes followed by passivating them with a 0.5 nm thick Ta<sub>2</sub>O<sub>5</sub>-overlayer and compare them with samples uniformly doped with the same amount of tantalum. We observe a three-fold improvement in photocurrent with the same onset voltage using Ta-overlayer hematite photoanodes, while electrochemical impedance spectroscopy under visible light irradiation shows a decreased amount of surface states under water splitting conditions. The Ta-doped samples have an even higher increase in photocurrent along with a 0.15 V cathodic shift in the onset voltage and decreased resistivity. However, the surface state capacitance for the Ta-doped sample is twice that of the reference photoanode, which implies a larger amount of surface hole accumulation. We further utilize transient absorption spectroscopy in the sub-millisecond to second timescale under operating conditions to show that electron trapping in both Ta<sub>2</sub>O<sub>5</sub>-passivated and Ta-doped samples is markedly reduced. Ultrafast transient absorption spectroscopy in the sub-picosecond to nanosecond timescale shows faster charge carrier dynamics and reduced recombination in the Ta-doped hematite photoanode resulting in the increased photoelectrochemical performance when compared with the Ta<sub>2</sub>O<sub>5</sub>-overlayer sample. Our results show that passivation does not affect the poor charge carrier dynamics intrinsic to hematite based photoanodes. The Ta-doping strategy results in more efficient electron extraction, solving the electron trapping issue and leading to increased performance over the surface passivation strategy.

Received 1st October 2018  
Accepted 14th January 2019

DOI: 10.1039/c8ta09501a  
rsc.li/materials-a

## 1 Introduction

Photoelectrochemical water splitting with stable metal oxide materials produces environmentally friendly hydrogen gas that can be transported over large distances to be burned in conventional gas power plants or converted directly into electricity using fuel cells. This solution allows to store solar energy directly into chemical bonds, thus potentially solving the

problems associated with intermittent and localized solar electricity production.

Hematite ( $\alpha$ -Fe<sub>2</sub>O<sub>3</sub>) has been regarded as one of the most promising candidates for photoelectrochemical water splitting ever since it was first used for this purpose by Hardee and Bard in 1976.<sup>1</sup> Hematite has numerous advantages as a photoanode material, such as a near optimal band gap of 2.2 eV that results in a theoretical solar-to-hydrogen efficiency of 12.9%,<sup>2</sup> high chemical stability in non-acidic conditions, natural abundance, and low production costs.<sup>3,4</sup> However, the efficiencies of hematite photoanodes remain low due to a few intrinsic drawbacks: (i) a flat band potential that is too low for water reduction, (ii) poor electron mobility, and (iii) a small hole diffusion length of 2–20 nm.<sup>5–8</sup> Furthermore, surface states at the hematite–electrolyte interface can also act as recombination centers that drastically decrease the photoanode performance.<sup>9</sup>

Metal oxide surfaces are spontaneously hydroxylated in aqueous conditions.<sup>10</sup> Iandolo *et al.*<sup>11</sup> showed that hematite surfaces are populated by OH- and O-terminations of the iron oxide lattice, both of which act as surface states. The hydroxyl-terminated surface states are occupied mid-gap states that act as surface recombination centers at low applied bias voltages.

<sup>a</sup>Chemistry and Advanced Materials, Laboratory of Chemistry and Bioengineering, Tampere University of Technology, P.O. Box 541, FI-33101 Tampere, Finland. E-mail: tero-petri.ruoko@lii.se

<sup>b</sup>Department of Chemistry, University of Helsinki, P.O. Box 55, FI-00014 Helsinki, Finland

<sup>c</sup>Surface Science Group, Laboratory of Photonics, Tampere University of Technology, P.O. Box 692, FI-33101 Tampere, Finland

<sup>d</sup>Department of Physics, University of Helsinki, P.O. Box 43, FI-00014 Helsinki, Finland

† Electronic supplementary information (ESI) available: XPS elemental analysis table and transient absorption fitting details, decay component spectra, and additional decays. See DOI: 10.1039/c8ta09501a

‡ Present address: Laboratory of Organic Electronics, Department of Science and Technology, Linköping University, SE-60174 Norrköping, Sweden.



On the other hand, the oxo-terminated states are located energetically on the top of the valence band, and take part in the oxygen evolution reaction (OER) at medium biases. Passivation of the hematite surface states has been shown to increase the performance of hematite photoanodes.<sup>4</sup> Numerous different methods have been employed to passivate hematite surfaces, including high temperature annealing,<sup>12</sup> acid treatment,<sup>13</sup> deposition of possibly passivating catalysts such as cobalt phosphate (Co-Pi),  $\text{IrO}_x$  or  $\text{NiFeO}_x$ ,<sup>14–19</sup> and depositing thin metal oxide overlayers, such as  $\text{TiO}_2$ ,<sup>20–22</sup>  $\text{Ga}_2\text{O}_3$ ,<sup>14,17</sup> or  $\text{Al}_2\text{O}_3$ .<sup>14,17–19,23–25</sup> Out of the metal oxide passivating layers used for hematite photoanodes,  $\text{TiO}_2$  has yielded inconclusive results, varying from no improvement<sup>20,23</sup> to improvement only after high temperature annealing<sup>22</sup> or a solution deposition process.<sup>26</sup> On the other hand,  $\text{Ga}_2\text{O}_3$  (ref. 14) and to some extent also  $\text{Al}_2\text{O}_3$  (ref. 27) are susceptible to dissolution in basic electrolytes. For these reasons we chose to study the effects of  $\text{Ta}_2\text{O}_5$  as an overlayer and dopant in hematite photoanodes.

$\text{Ta}_2\text{O}_5$  is a large band gap (3.9 eV)<sup>28</sup> metal oxide which is often used in anti-reflective coatings for solar cells and sensors. Due to its high-permittivity and excellent chemical stability it has also found applications in the semiconductor industry, such as in dielectric layers for transistors and storage capacitors.<sup>29</sup> The band levels of  $\text{Ta}_2\text{O}_5$  straddle the water oxidation and reduction potentials,<sup>28</sup> making it a potential candidate for use as an overall water splitting photocatalyst.<sup>30</sup> However, due to the large band gap it cannot be excited with visible light irradiation, greatly limiting the obtainable photocurrent.  $\text{Ta}_2\text{O}_5$  has previously been used as a dopant in hematite photoanodes, but the results have been inconclusive. Ta-doping increases the conductivity of hematite,<sup>31</sup> but photoelectrochemical improvements due to the doping have varied from non-existent,<sup>32</sup> to a 3.5 time improvement for water oxidation,<sup>33</sup> reaching all the way to a 32 time improvement in photocurrent over pristine hematite in the presence of scavengers.<sup>34</sup>  $\text{Ta}_2\text{O}_5$  was recently used as a surface passivation layer for ZnO photoanodes, leading to nearly two-fold improved photoelectrochemical performance.<sup>35</sup> The chemical stability of  $\text{Ta}_2\text{O}_5$  promises more stable passivating layers in non-neutral solutions than  $\text{Ga}_2\text{O}_3$  or  $\text{Al}_2\text{O}_3$ .  $\text{Ta}_2\text{O}_5$  was recently utilized as an overlayer for hematite photoanodes, which resulted in approximately a three-fold increase in the photocurrent over pristine nanostructured hematite photoanodes.<sup>36</sup>

Herein, we utilized 50 nm thick hematite photoanodes made by atomic layer deposition (ALD). The deposition method and sample thickness were chosen to have a uniform sample surface, while keeping the sample absorbance relatively low in order to characterize the charge carrier dynamics using transient absorption spectroscopy (TAS). The  $\text{Ta}_2\text{O}_5$ -passivated samples were prepared by depositing an ultrathin (roughly 0.5 nm) overlayer by ALD, whereas Ta-doped samples were prepared by applying one  $\text{Ta}_2\text{O}_5$  deposition cycle once every hundred hematite deposition cycles. This resulted in the same number of Ta-precursor cycles for both overlayer and doped samples. We observed a three-fold improvement in photocurrent with the same onset voltage using  $\text{Ta}_2\text{O}_5$ -overlayer hematite photoanodes. Electrochemical impedance spectroscopy (EIS)

under visible light irradiation showed a decreased amount of surface states under water splitting conditions, indicating that the surface has indeed been passivated. However, the Ta-doped samples showed an even larger increase in photocurrent along with a 0.15 V cathodic shift in the onset voltage and decreased resistivity. Remarkably, the surface state capacitance for the Ta-doped hematite was two times larger than for the reference photoanode. We utilized TAS in the sub-millisecond to second timescale under water splitting conditions to show that electron trapping in both  $\text{Ta}_2\text{O}_5$ -passivated and Ta-doped samples was markedly reduced. Ultrafast TAS in the sub-picosecond to nanosecond timescale indicated faster charge carrier dynamics in the Ta-doped hematite photoanode to be a probable reason for the increased photoelectrochemical performance.

## 2 Experimental

Hematite photoanodes were grown on fluorine doped tin oxide (FTO) coated glass substrates (Sigma-Aldrich TEC7,  $\sim 7 \Omega \text{ sq}^{-1}$ ) using the  $\text{FeCl}_3 + \text{H}_2\text{O}$  deposition process<sup>37</sup> in a F-120 ALD reactor (ASM Microchemistry) operated in the cross-flow configuration.<sup>38</sup> The reference and overlayer hematite samples were grown at 400 °C using 1000 ALD-cycles, after which the samples were annealed at 600 °C for 60 minutes in air. The resulting layer thickness was 50 nm. The  $\text{Ta}_2\text{O}_5$ -overlayer was grown by applying 10 cycles of the  $\text{Ta}(\text{OC}_2\text{H}_5)_5 + \text{H}_2\text{O}$  deposition process at 300 °C on the annealed hematite surface.<sup>39</sup> The deposition temperature of the overlayer was lower in order to avoid the thermal decomposition of  $\text{Ta}(\text{OC}_2\text{H}_5)_5$ , which becomes significant at temperatures above 325 °C. The resulting overlayer thickness was 0.5 nm. The Ta-doped samples were grown by repeating the  $\text{Ta}(\text{OC}_2\text{H}_5)_5 + \text{H}_2\text{O}$  cycle once after every 99  $\text{FeCl}_3 + \text{H}_2\text{O}$  cycles at 300 °C for a total of 1000 cycles, followed by annealing at 600 °C for 60 minutes in air. All as-prepared samples were finally annealed at 300 °C for 60 minutes in air to remove possible organic contaminants. The ALD deposition process is presented schematically in Fig. 1. Note that Fig. 1 does not represent the final sample structure due to the rough FTO substrate and the annealing steps inducing diffusion of tantalum within the samples.

X-ray photoelectron spectroscopy (XPS) measurements were performed utilizing a non-monochromatized Al K $\alpha$  X-ray source ( $h\nu = 1486.6 \text{ eV}$ ) and an Argus hemispherical electron spectrometer (Omicron Nanotechnology GmbH) installed in

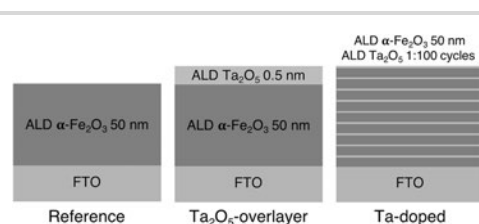


Fig. 1 Schematic representation of the ALD deposition processes for the reference,  $\text{Ta}_2\text{O}_5$ -overlayer, and Ta-doped hematite photoanodes.



a multifunctional UHV system with a base pressure below  $1 \times 10^{-10}$  mbar.<sup>40</sup> The binding energy scale of the XPS spectrometer was calibrated according to the metallic Cu  $2p_{3/2}$  at 932.40 eV and Ag  $3d_{5/2}$  at 368.00 eV. The surface elemental concentrations and chemical states of compounds were identified by analyzing high-resolution XPS spectra using CasaXPS software (Version 2.3.18 PR 1.0). After a Shirley-type background subtraction, the peaks were least-squares fitted with a combination of symmetric Gaussian–Lorentzian line shapes. The relative atomic concentrations were calculated using Scofield photoionization cross sections<sup>41</sup> and the experimentally measured transmission function of the Argus analyser.

Depth profiles for the hematite photoanodes were calculated using combined data from time-of-flight elastic recoil detection analysis (ToF-ERDA) and Rutherford backscattering spectroscopy (RBS) measurements. The ion beam measurements were done at the Accelerator Laboratory at University of Helsinki using a 5 MV tandem accelerator.<sup>42</sup> For the ToF-ERDA measurements, a 50 MeV  $^{127}\text{I}^{9+}$  ion beam was used whereas the RBS measurements were done using a 8 MeV  $^{12}\text{C}^{+}$  ion beam.

Field emission scanning electron microscopy images were taken with a Carl Zeiss Ultra 55 with an acceleration voltage of 4 kV. The absorption spectra of the hematite photoanodes were measured with a Shimadzu UV-3600 UV-Vis-NIR spectrophotometer in transmission mode.

All measurements with bias voltages were carried out in a three electrode photoelectrochemical cell (PECC-2, Zahner) in 0.1 M NaOH (pH  $\approx$  12.8). The bias voltages were set using a potentiostat (CompactStat, Ivium Technologies) or a two channel source-monitoring unit (E5272A, Agilent Technologies) using a Ag/AgCl reference electrode (RE-5B, BASi, 3 M NaCl) and a platinum wire counter electrode. Electrochemical impedance measurements were scanned in the frequency range of 10 kHz to 10 mHz with a 10 mV AC signal. All voltages are reported relative to the reversible hydrogen electrode (RHE) scale, calculated using  $E_{\text{RHE}} = E^{\circ} + E_{\text{Ag/AgCl}} + 0.059\text{pH}$ , where  $E^{\circ}$  is the reference potential of the Ag/AgCl electrode (0.206 V<sub>SHE</sub> at 25 °C),  $E_{\text{Ag/AgCl}}$  is the measured potential *versus* the Ag/AgCl electrode. Current density–voltage and electrochemical impedance measurements were performed under simulated sunlight obtained with a class AAA solar simulator (Sciencetech SS150-AAA) adjusted to one sun total intensity with a calibrated Si reference cell (Oriol 91150V) with electrolyte-side illumination.

Transient absorption in the sub-ms to s timescales was studied using the flash-photolysis method in transmission mode. The third harmonic (F015, Solar TII, 355 nm, 0.2 mJ cm<sup>-2</sup>, electrolyte-side illumination) of a Nd:YAG laser (LF117, Solar TII, 10 ns pulse width, 0.25 Hz repetition rate) was used as the excitation pump. A stabilized halogen light source (SLS201/M, Thorlabs, 9 W) was used as the probe beam. The monochromatic (CM110, Digikröm) transient signal was detected with a silicon photoreceiver (2051-FS, New Focus) and recorded with a digitizing oscilloscope (TDS5032B, Tektronix). An in-lab program was used to manage the experiment. The transient decays were averaged over 200–1000 laser shots.

Transient absorption in the sub-ps to ns timescales was studied using the pump–probe method in transmission mode.

The fundamental laser pulses were generated with a Ti:Sapphire laser (Libra F, Coherent Inc., 800 nm,  $\sim$ 100 fs pulse width, repetition rate 1 kHz). 90% of the fundamental beam energy was directed to an optical parametric amplifier (Topas C, Light Conversion Ltd.) to produce the desired wavelength excitation pump pulses (355 nm, approximately 0.5 mm diameter at the sample, attenuated to 0.3 mJ cm<sup>-2</sup> with neutral density filters). Roughly 10% of the fundamental laser beam energy was directed through a motorized translational stage (delay line) to a 1 mm thick water cuvette for white continuum generation of probe pulses. The probe light was split into the reference and signal beams. The measurement system (ExciPro, CDP Inc.) was equipped with a Si CCD pair for monitoring the transient absorption in the visible range. A chopper synchronized with the fundamental laser pulses was used to block every second pump pulse, and the absorbance change was calculated from consecutive pulses. The spectra were averaged over 10 000 excitation pulses for each delay time.

### 3 Results and discussion

The ALD-grown hematite creates a uniform layer on the rough FTO substrate, as shown in the scanning electron microscope (SEM) images of the photoanode surfaces in Fig. 2. The deposition of a 0.5 nm Ta<sub>2</sub>O<sub>5</sub> overlayer does not change the surface morphology of the photoanode. However, the introduction of the Ta<sub>2</sub>O<sub>5</sub> precursor during hematite film growth as a dopant leads to the formation of a rougher surface texture with larger crystallites of up to 500 nm in diameter. A disturbance of hematite nanorod growth upon Ta-doping,<sup>33</sup> as well as a preferential crystal growth along the {001} facet have been previously reported.<sup>34</sup> Thus, we conclude that the Ta-dopant disturbs the uniform hematite growth, leading to the formation of larger crystallites.

X-ray photoelectron spectroscopy (XPS) was employed for the analysis of Ta addition on the chemical composition of the hematite surfaces. The relative surface composition of elements and chemical species is presented in Table S1† Fig. 3 depicts the Fe 2p and Ta 4f spectra of the samples (spectra with fitted components are presented in Fig. S1†). The spectral features of Fe 2p were similar for all samples, and the binding energies of the Fe  $2p_{3/2}$  peak at 710.4 eV and the satellite peak at 719.5 eV are characteristic to the oxidation state of Fe<sup>3+</sup> in, for example, hematite ( $\alpha$ -Fe<sub>2</sub>O<sub>3</sub>).<sup>43</sup> For the Ta-doped and Ta<sub>2</sub>O<sub>5</sub>-overlayer hematite samples the binding energy of Ta 4f<sub>7/2</sub> at 25.5 eV can be attributed to Ta<sup>5+</sup> in accordance with the value observed by Zhang *et al.*<sup>34</sup> Neither Fe nor Ta species were observed at lower oxidation states than 3+ or 5+, respectively, which indicates a low amount of oxygen vacancies. No change in the Ta 4f peak position was observed despite the change in the Ta/Fe ratio of the Ta-doped and Ta<sub>2</sub>O<sub>5</sub>-overlayer hematite samples from 0.16 to 0.58, respectively. The high Ta/Fe ratio of the Ta-doped sample compared to the bulk ratio (0.01) indicates annealing induced surface segregation of tantalum and the formation of a Ta diffusion profile through the sample, however, the even higher ratio in the Ta<sub>2</sub>O<sub>5</sub>-overlayer hematite suggests the formation of a surface layer.



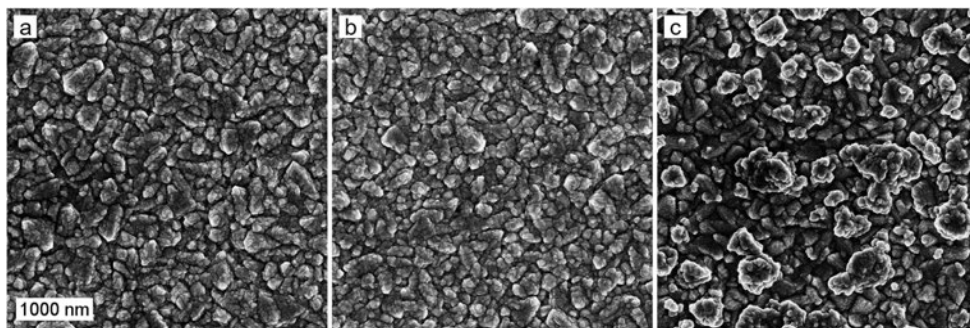


Fig. 2 SEM micrographs of the (a) reference, (b) Ta<sub>2</sub>O<sub>5</sub>-overlayer, and (c) Ta-doped hematite photoanodes. The scale bar represents 1000 nm.

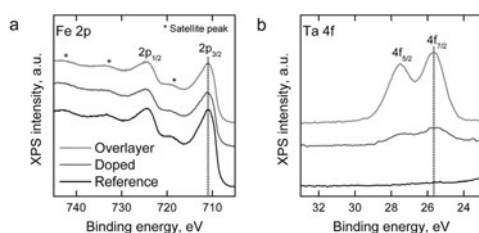


Fig. 3 (a) Fe 2p and (b) Ta 4f XPS spectra of the hematite photoanodes.

We determined the elemental depth distribution within the hematite photoanodes using time-of-flight elastic recoil detection analysis (ToF-ERDA) and Rutherford backscattering spectroscopy (RBS). The elemental depth profiles and the tantalum distribution for the hematite photoanodes are presented in Fig. 4 and S2.†

Diffusion of tin from the FTO substrate towards the surface can be seen for all samples in Fig. S2,† however, tin does not diffuse all the way to the surface. The ToF-ERDA results show very little carbon within the films, indicating that the carbon that was observed in the XPS measurements is a surface contaminant from the atmosphere. Tantalum is not observed for the reference photoanode. The Ta<sub>2</sub>O<sub>5</sub>-overlayer hematite has

a very narrow distribution of tantalum with an extended tail, showing that the Ta<sub>2</sub>O<sub>5</sub> deposition forms a clearly defined overlayer with tantalum diffusing slightly into the hematite layer in the post-deposition annealing. On the other hand, the tantalum distribution in the Ta-doped hematite photoanode is more uniform, suggesting that the annealing step has dispersed the tantalum throughout the hematite layer. A slight surface enrichment can also be seen in the Ta-doped hematite photoanode, as was suggested by the XPS results.

The absorption spectra of the reference and Ta<sub>2</sub>O<sub>5</sub>-overlayer hematite presented in Fig. 5a are almost identical, supporting the fact that the hematite layer thickness is identical for both films. Ta<sub>2</sub>O<sub>5</sub> has a band gap of 3.9 eV,<sup>28</sup> leading to an overlapping absorption with the glass substrate at around 315 nm. The increase in absorption for the doped sample is a result of the rougher surface of the photoanode scattering incident light, leading to a seeming increase in absorption already at 800 nm. However, the Ta-doped photoanode absorbance is roughly the same as for the other photoanodes when the scattering is taken into consideration.

Current density–voltage curves under 1 sun AM1.5G illumination are presented in Fig. 5b. The reference hematite films give a photoresponse similar to what has been previously reported for ALD-grown hematite films of similar thickness,<sup>20</sup> allowing us to conclude that the photoanodes work as expected. Passivating the surface with 10 cycles (~0.5 nm) of Ta<sub>2</sub>O<sub>5</sub> results

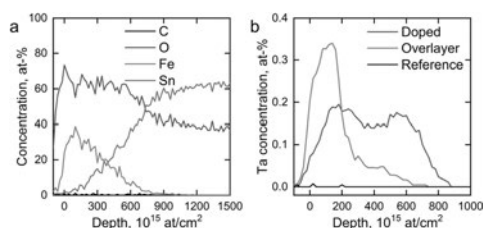


Fig. 4 (a) ToF-ERDA elemental depth profile of the reference photoanode and (b) Ta distribution in the hematite photoanodes.

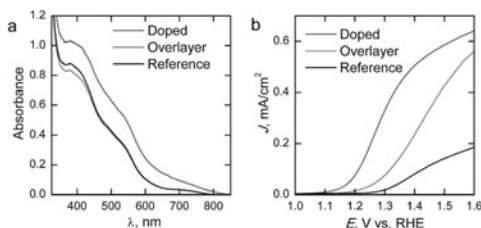


Fig. 5 (a) Absorption spectra and (b) photocurrent density–voltage curves of the hematite photoanodes under 1 sun AM1.5G illumination.



in a three-fold improvement on the photocurrent over the bare hematite photoanode in the whole potential range, while no changes are observed in the onset potential. In a recent paper Forster *et al.*<sup>36</sup> concluded that the optimum Ta<sub>2</sub>O<sub>5</sub> overlayer thickness lies between 0.5 and 2 nm, which also resulted in approximately a three-fold improvement on the photocurrent of nanostructured hematite photoanodes. The improvements in photocurrent are attributed to a passivation of surface states that act as recombination centers. However, our results show that Ta-doping with the same number of ALD-cycles leads to an even larger improvement in photoelectrochemical performance. The Ta-doping approach results in a larger increase in the photocurrent than the Ta<sub>2</sub>O<sub>5</sub>-overlayer, along with a 0.15 V cathodic shift in the onset potential, leading to significantly higher photocurrents in the whole potential range shown. Furthermore, the slope of the photocurrent rise after the onset potential is steeper for the Ta-doped sample, which indicates lower resistivity. The decreased resistivity is presumably due to the Ta-doping inducing preferential growth along the {001} facet of hematite, which has previously been reported to lead up to a one order of magnitude increase in conductivity.<sup>34</sup>

We performed electrochemical impedance spectroscopy (EIS) measurements in order to characterize the surface states present in our materials. Representative Nyquist plots of the materials held at 1.40 V vs. RHE under 1 sun AM1.5G illumination are presented in Fig. 6a. The reference hematite exhibits two clear semicircles, which indicates the presence of two capacitances in the system. The higher frequency (left side) semicircle is only weakly bias dependent, whereas the lower frequency (right side) semicircle first grows with increased bias voltages before disappearing at higher potentials. For the Ta<sub>2</sub>O<sub>5</sub>-overlayer hematite two semicircles are also observed, but both semicircles have a much smaller diameter than for the reference hematite. On the other hand, at this applied potential the Ta-doped hematite only exhibits one semicircle, which almost exactly matches with the high frequency semicircle observed for the reference hematite film. However, two clear semicircles are observed for this sample at lower applied potentials.

To fit the EIS measurements we used the equivalent circuit that has been recently employed for hematite photoanodes by the groups of Hamann and Bisquert, shown in Fig. 6b.<sup>9,25,44,45</sup> The equivalent circuit is composed of five elements: the series

resistance between the FTO and hematite  $R_s$ , the space-charge region capacitance of bulk hematite  $C_{sc}$ , the charge trapping resistance to surface states  $R_{trap}$ , the surface state chemical capacitance  $C_{ss}$ , and the charge transfer resistance from the surface states to solution  $R_{ct}$ .<sup>9,11,25</sup>

The surface state capacitance ( $C_{ss}$ ) and charge transfer resistance ( $R_{ct}$ ) of the hematite photoanodes are presented in Fig. 7 as a function of applied bias voltage. The  $C_{ss}$  has a nearly Gaussian dependence on the bias voltage just above the onset potential, indicating that water oxidation occurs through surface states and *via* direct hole transfer from the valence band at moderate and highly anodic bias voltages, respectively.<sup>9,11</sup>  $C_{ss}$  begins to rise at the same voltage as the photocurrent onset, and reaches a maximum at the potential at which the photocurrent rises most steeply, indicative of capacitive charging of the photoanode surface.<sup>45</sup> The Ta<sub>2</sub>O<sub>5</sub>-overlayer hematite has a lower surface state capacitance than the reference hematite while the photocurrent is three times larger, indicating that the surface has been efficiently passivated. On the other hand, the  $C_{ss}$  of the Ta-doped hematite photoanode is more than two times larger than for the reference hematite, even though it exhibits the highest photocurrent values. This is a clear indication that the Ta-doping has not passivated the surface, yet it performs with the highest efficiency. The  $R_{ct}$  of all of the photoanodes decreases concomitantly with the increase in  $C_{ss}$  until the surface state capacitance drops due to hole transfer from the valence band becoming prevalent. The  $R_{ct}$  for the Ta-doped hematite is an order of magnitude lower at all bias voltages where the surface state capacitance is observed. The charge transfer resistance in our equivalent circuit is attributed to both electron trapping and detrapping to and from the surface states.<sup>9</sup> We believe that the increased performance of the Ta-doped hematite can be attributed to decreased recombination, enabled by the higher conductivity of the material more efficiently extracting electrons away from the photoanode.

The chemical nature of the surface states observed under illumination with EIS for hematite photoanodes has been convincingly attributed to the formation of a high valence Fe(IV)=O species by the Hamann group.<sup>25,45,46</sup> They showed that the formation of this oxidised surface species resulted in the formation of a new absorption band centered at 572 nm when the photoanode was kept under anodic bias voltages.<sup>25</sup> Transient absorption spectroscopy (TAS) performed under operating

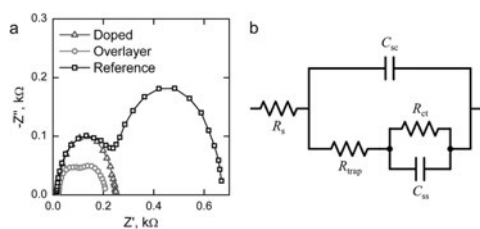


Fig. 6 (a) Representative Nyquist plots of the hematite photoanodes determined under 1 sun AM1.5G illumination at 1.40 V vs. RHE and (b) the equivalent circuit used to fit the measured impedance spectra.

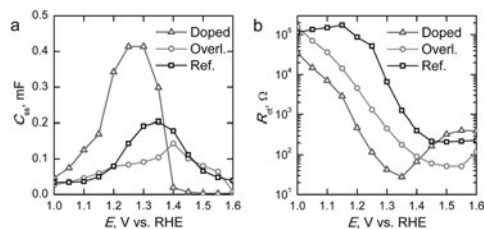


Fig. 7 (a) Surface state capacitances ( $C_{ss}$ ) and (b) charge transfer resistances ( $R_{ct}$ ) of the hematite photoanodes determined under 1 sun AM1.5G illumination.





conditions has been used to show ultrafast sub-picosecond electron trapping into a surface species on the hematite surface, with the trapping extending well into the millisecond timescale.<sup>47,48</sup> This trapping is observed as a bleaching (*i.e.* reduced absorption compared to the ground state) at 575 nm when an anodic bias voltage is applied. We believe that this bleaching occurs when a photogenerated electron is trapped into the surface state seen in the EIS measurements. We have illustrated earlier that an increase in this electron trapping results in the formation of an increased amount of long-lived holes in the hematite surface, resulting in increased photoelectrochemical performance.<sup>48</sup> Thus, we performed sub-millisecond to second timescale TAS measurements under operating conditions to elucidate on the differences in charge carrier dynamics and electron trapping between our photoanodes.

The transient absorption decays of the hematite photoanodes at 575 nm at selected bias voltages are presented in Fig. 8 and the corresponding biexponential decay component spectra at 1.60 V *vs.* RHE are presented in Fig. S3.† The decays for the reference hematite photoanode have two components: a negative bleach that disappears completely within 100 ms and a positive transient absorption on longer timescales that is only visible at bias voltages above the photocurrent onset potential. The lifetimes of the components at 1.60 V *vs.* RHE are 6.4 ms and 405 ms for the bleach and positive signals, respectively. The fast bleach is attributed to prolonged electron trapping into the surface states that we are able to observe with EIS, whereas the positive transient absorption is attributed to long-lived holes in the hematite surface that partake in the water oxidation reaction.<sup>47,48</sup> The bleach is a localised band with a minimum at 575 nm, whereas the positive transient absorption is observed in the whole monitored region. The transient absorption decays and decay component spectra of the reference hematite are a good match to those we have published earlier for TiO<sub>2</sub>-doped hematite photoanodes, even though the electron trapping lifetime of our reference hematite is longer than for the TiO<sub>2</sub>-doped samples (6.4 ms *vs.* 0.3 ms, respectively).<sup>48</sup> We attribute this difference to the faster electron extraction dynamics from the surface states due to the preferable band alignment of the TiO<sub>2</sub>-

doped material.<sup>49</sup> However, the water oxidation dynamics are practically identical (exponential lifetimes 405 ms and 400 ms).

In this timescale the transient absorption amplitude for the Ta<sub>2</sub>O<sub>5</sub>-overlayer hematite sample is zero at potentials below the photocurrent onset voltage and increases with higher voltages, indicating that all of the transient absorption signal observed originates from long-lived carriers within the depletion region. No negative transient absorption is observed. However, there is a slight dip still visible at 575 nm in the decay component spectra shown in Fig. S3.† This is further evidence that the bleach component observed for the reference hematite sample originates from trapping of photogenerated electrons into the surface states that we observe with EIS. Since the Ta<sub>2</sub>O<sub>5</sub>-overlayer passivates these surface states, they are not oxidised due to increased anodic bias voltage, and thus cannot act as trap states for electrons. The transient absorption kinetics are also different when compared to the reference hematite sample. The transient absorption decay at 575 nm is almost an order of magnitude faster, with bi-exponential fit resulting in lifetimes of 3.0 and 65 ms for the fast and slow decay components, respectively. This indicates that water oxidation occurs faster on the passivated hematite surface. The water photo-oxidation kinetics on hematite surfaces are known to be sluggish.<sup>50</sup> The hole lifetime in nanostructured TiO<sub>2</sub> thin films was measured under similar conditions to be ~50 ms by Cowan *et al.*,<sup>50</sup> which is close to the lifetime of our Ta<sub>2</sub>O<sub>5</sub>-overlayer hematite. Thus, in addition to the reduced recombination due to the surface state passivation, some of the improved photoelectrochemical performance of the Ta<sub>2</sub>O<sub>5</sub>-overlayer hematite films may be due to a photocatalytically more favourable surface with a smaller activation energy barrier.<sup>50</sup> Tantalum, as a non-3d high valency metal, may improve the catalytic activity *via* modulating the oxygen evolution reaction energetics in 3d metal oxides, such as hematite.<sup>51</sup>

The fast component in the transient absorption decays of the Ta-doped hematite is the fastest of the samples with a lifetime of 1.4 ms and smallest in amplitude. This is indicative of reduced recombination of the long-lived surface states.<sup>48</sup> Furthermore, the longer component assigned to the reaction of long-lived surface holes with a lifetime of 95 ms is four times

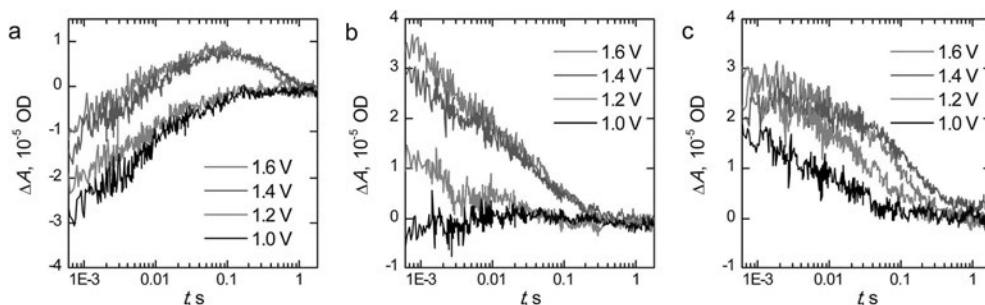


Fig. 8 Sub-millisecond to second timescale transient absorption decays at 575 nm of (a) reference, (b) Ta<sub>2</sub>O<sub>5</sub>-overlayer, and (c) Ta-doped hematite photoanodes held at selected bias voltages *vs.* RHE.  $\Delta A$  is the change in absorbance in dimensionless optical density (OD) units.



faster than for the reference hematite sample. We attribute this to the surface of the material having enough tantalum to influence the water photo-oxidation kinetics, making the reaction faster as was observed for the Ta<sub>2</sub>O<sub>5</sub>-overlayer hematite. This is further supported by the similarities between the decay component spectra between the Ta-doped and Ta<sub>2</sub>O<sub>5</sub>-overlayer hematite. The Ta-doped hematite exhibits a positive transient absorption even at 1.0 V vs. RHE. This is presumably due to the observed anodic shift both in the photocurrent and surface state capacitance leading to accumulation of surface holes at lower potentials. The decay at 1.0 V vs. RHE does not have a long-lived component, indicating that the long-lived holes decay rapidly due to electron back recombination.<sup>52</sup> As a conclusion, TAS measurements under operating conditions indicate the reason for the increased photoelectrochemical performance of the Ta-doped hematite to be due to reduced recombination and charge trapping to defect states.

Although the Ta-doped hematite does have a dip in the transient absorption centered around 575 nm that is very similar to the surface passivated Ta<sub>2</sub>O<sub>5</sub>-overlayer hematite (see Fig. S3†), the EIS measurements show that it has the largest surface state capacitance. We would expect that the bleaching in TAS would be more pronounced with samples where the surface state capacitance is larger if the electron trapping occurs to the same surface states that are observed with EIS. From our results it seems that this is not the case here. However, it is also possible that the higher conductivity of the Ta-doped hematite also increases the rate of photoelectron detrapping. We have previously shown that electron trapping in hematite occurs already in the sub-nanosecond timescale.<sup>48</sup> Forster *et al.* showed that an Al<sub>2</sub>O<sub>3</sub>-overlayer significantly increased the rate of photoelectron detrapping in oxygen deficient hematite photoanodes,<sup>27</sup> although the same group did not observe significant changes in the detrapping rate with Ta<sub>2</sub>O<sub>5</sub>-overlayered hematite.<sup>36</sup> Thus, it is possible that the limited time-scale of our measurement system may miss the trapping in the Ta-doped hematite.

We next turn to transient absorption spectroscopy in the sub-picosecond to nanosecond timescale to probe the ultrafast charge carrier relaxation and recombination processes. The transient absorption spectra are presented as contour plots in Fig. 9. The normalized transient absorption spectra at selected delay times are shown in Fig. S4† and the transient absorption decays at wavelengths with the largest transient absorption and bleach signals are shown in Fig. S5.† On this timescale the transient absorption signal is composed of a superposition of the absorptions of photogenerated electrons, holes, and the ground state bleach. All three samples exhibit a strong positive transient absorption band centered around 585 nm, with a diffuse low energy tail and a sharp high energy edge around the band gap energy. This transient absorption has previously been assigned to originate dominantly from the absorption of photoexcited electrons.<sup>33</sup> However, recent investigations of hematite photoanodes under applied bias voltages have revealed a positive absorption at the same wavelength that is formed due to a high valence iron-oxo species, as discussed earlier. Furthermore, our previous results show that ultrafast

electron trapping into oxidized surface states inverts the positive absorption ~580 nm into a bleaching signal that we can observe still in the millisecond timescale in Fig. 8.<sup>48</sup> Thus, we conclude that the main component of the positive transient absorption is due to photogenerated holes in hematite.<sup>54</sup> All three samples also exhibit a transient bleach signal below 550 nm, attributed to the bleaching of the ground state absorption due to mostly photogenerated electrons, with a secondary weak positive transient absorption band that is split around 500 nm. However, it seems that the bleach intensity grows in the order of reference, Ta<sub>2</sub>O<sub>5</sub>-overlayer, and Ta-doped hematite. The major differences between the samples in the transient absorption spectra lie in the range between 450–550 nm. The transient absorption decays at selected wavelengths from this region are presented in Fig. 10. The four exponential decay component spectra of the different lifetime components are shown in Fig. S6.†

We will first consider the ultrafast dynamics in the reference hematite photoanode in Fig. 10a. The initial relaxation of hot electrons takes place with a lifetime of 0.21 ps,<sup>55,56</sup> with the decay amplitude amounting to approximately 50% of the transient absorption immediately after excitation (see Fig. S5 and S6†). This initial decay is mainly observed at wavelengths with positive transient absorption above 570 nm, although a small bleach recovery is observed at wavelengths below 450 nm with this lifetime. The fast relaxation is presumably due to the formation of polarons in the hematite bulk, partially trapping the charge carriers.<sup>57</sup> The generation of itinerant photoexcited electrons<sup>56</sup> that are free to travel in the conduction band is most clearly observed in the bleach that is formed with a lifetime of 1.6 ps at 530 nm, with a simultaneous decay observed over most of the spectrum above 500 nm. The free conduction electrons are trapped by midgap states,<sup>55</sup> which is seen as a reduction in the bleach at 530 and 520 nm and a formation of a positive transient absorption at 500, 485, and 470 nm with a lifetime of 46 ps. Interestingly, the 470 nm signal shows almost zero transient absorption until the formation increases its transient absorption. Finally, the remaining free and midgap trapped electrons decay into the ground state with a lifetime of 2.4 ns.

The ultrafast dynamics of the Ta<sub>2</sub>O<sub>5</sub>-overlayer hematite exhibit a few noted differences when compared with the reference hematite. Only the signal at 500 nm has a positive transient absorption immediately after excitation, having the same 0.21 ps decay component associated with the relaxation of hot electrons. At 470 and 530 nm a bleach is formed immediately after excitation, with further bleaching with a lifetime of 2.1 ps assigned to the formation of free conduction band electrons observed at 530, 520, and 485 nm. Thus, the formation of free electrons in the Ta<sub>2</sub>O<sub>5</sub>-overlayer hematite is more rapid and observed over a wider energetic range. The trapping of the conduction band electrons by midgap states occurs with a slower lifetime of 61 ps, with nearly identical amplitudes as for the reference hematite. Furthermore, the decay of the free and trapped electrons occurs with a lifetime of 3.4 ns, markedly slower than for the reference hematite. We attribute the faster generation and slower recombination dynamics of electrons to a reduction in surface state assisted recombination.



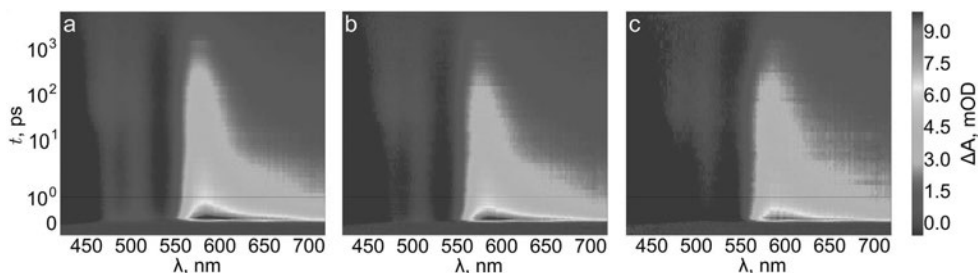


Fig. 9 Transient absorption contour plots of (a) reference, (b) Ta<sub>2</sub>O<sub>5</sub>-overlayer, and (c) Ta-doped hematite photoanodes in air.

However, the transient absorption dynamics for the Ta-doped hematite are drastically different from the reference and Ta<sub>2</sub>O<sub>5</sub>-overlayer hematite photoanodes. The bleach at 470 nm is now three times larger in amplitude than for the Ta<sub>2</sub>O<sub>5</sub>-overlayer hematite, whereas for the reference hematite no bleach was observable at this wavelength. All other wavelengths in the 450–550 nm range are also bleached immediately after excitation, most clearly visible in the raw and decay component spectra immediately after excitation as shown in Fig. S7.† The bleach recovery has two recovery components with lifetimes of 0.38 and 7.7 ps. We interpret this strong bleach immediately after excitation as indication that even the hot electrons are free to travel in the Ta-doped hematite, instead of being excitonically bound. The 0.38 ps component would then be the thermalization lifetime of the free hot electrons, whereas 7.7 ps is the lifetime of the trapping of these free electrons by the midgap states that form a positive transient absorption at 485 and 500 nm. A small component with a lifetime of 270 ps is observed to reduce the transient absorption at all wavelengths in this range, followed by a decay with a lifetime of 5.9 ns. The observation that free electrons are more freely generated and decay with the longest lifetime in the Ta-doped hematite suggests that the Ta-doping increases the conductivity in the hematite bulk substantially. This conductivity increase alters the ultrafast charge carrier dynamics and

separation, leading to noticeable improvements in photoelectrochemical performance.

## 4 Conclusions

We employed atomic layer deposition to prepare 50 nm thick hematite photoanodes followed by passivating them with a 0.5 nm thick Ta<sub>2</sub>O<sub>5</sub>-overlayer samples and compared them with samples uniformly doped with same amount of tantalum oxide deposition cycles. The passivating of hematite surface states resulted in a three-fold improvement in photocurrent with the same onset voltage, while electrochemical impedance spectroscopy under visible light irradiation showed a decreased amount of surface states under water splitting conditions. The Ta-doped samples had the same increase in photocurrent along with a 0.15 V cathodic shift in the onset voltage and decreased resistivity. The surface state capacitance for the Ta-doped sample was double that of the reference photoanode, which implies a larger amount of surface hole accumulation to surface states to which electrons may be trapped into. We utilized transient absorption spectroscopy in the sub-millisecond to second timescale under operating conditions that indicated that electron trapping in both Ta<sub>2</sub>O<sub>5</sub>-passivated and Ta-doped samples was markedly reduced. Ultrafast transient absorption spectroscopy in the sub-picosecond to nanosecond timescale

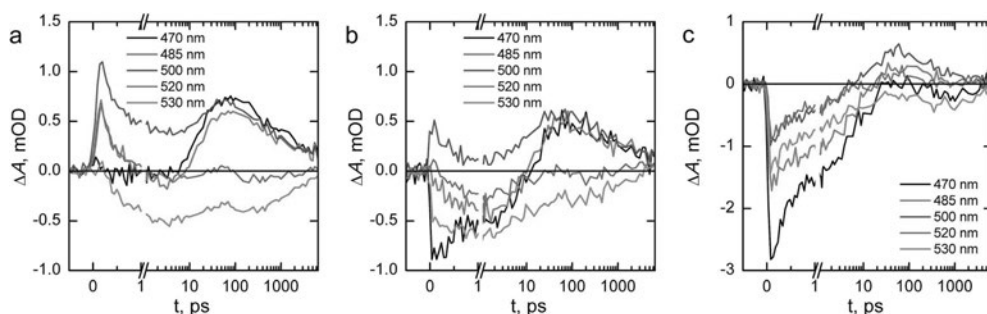


Fig. 10 Transient absorption decays at selected wavelengths of (a) reference, (b) Ta<sub>2</sub>O<sub>5</sub>-overlayer, and (c) Ta-doped hematite photoanodes in air. The timescale is linear until 1 ps and logarithmic for longer delay times.



illustrated increased electron mobility with free electrons forming immediately after excitation. Furthermore, the recombination in the Ta-doped hematite photoanode was reduced, resulting in the increased photoelectrochemical performance when compared with the Ta<sub>2</sub>O<sub>5</sub>-overlayer sample. Our results show that the commonly employed passivation strategy does not affect the poor charge carrier dynamics intrinsic to hematite based photoanodes. The large effect on the water splitting performance that electron trapping into surface states has in hematite based photoanodes has only recently been observed. Our Ta-doping strategy results in more efficient electron extraction, solving the electron trapping issue and leading to increased performance over the surface passivation strategy.

## Conflicts of interest

There are no conflicts to declare.

## Acknowledgements

T.-P. R. was supported by the Finnish Cultural Foundation. H. A. was supported by the Jenny and Antti Wihuri Foundation. This work was supported by the Academy of Finland, decision numbers 141481, 286713, and 309920. The research was also supported by the Finnish Centre of Excellence in Atomic Layer Deposition.

## References

- 1 K. L. Hardee and A. J. Bard, *J. Electrochem. Soc.*, 1976, **123**, 1024–1026.
- 2 A. Murphy, P. Barnes, L. Randeniya, I. Plumb, I. Grey, M. Horne and J. Glasscock, *Int. J. Hydrogen Energy*, 2006, **31**, 1999–2017.
- 3 K. Sivula, F. Le Formal and M. Grätzel, *ChemSusChem*, 2011, **4**, 432–449.
- 4 K. Sivula, *J. Phys. Chem. Lett.*, 2013, **4**, 1624–1633.
- 5 R. K. Quinn, R. Nasby and R. Baughman, *Mater. Res. Bull.*, 1976, **11**, 1011–1017.
- 6 J. H. Kennedy and K. W. Frese, *J. Electrochem. Soc.*, 1978, **125**, 709–714.
- 7 M. P. Dare-Edwards, J. B. Goodenough, A. Hamnett and P. R. Trellick, *J. Chem. Soc., Faraday Trans. 1*, 1983, **79**, 2027–2041.
- 8 K. Itoh and J. O. Bockris, *J. Appl. Phys.*, 1984, **56**, 874–876.
- 9 L. Bertoluzzi, P. Lopez-Varo, J. A. J. Tejada and J. Bisquert, *J. Mater. Chem. A*, 2016, **4**, 2873–2879.
- 10 A. Hellman and R. G. Pala, *J. Phys. Chem. C*, 2011, **115**, 12901–12907.
- 11 B. Iandolo and A. Hellman, *Angew. Chem., Int. Ed.*, 2014, **126**, 13622–13626.
- 12 O. Zandi and T. W. Hamann, *J. Phys. Chem. Lett.*, 2014, **5**, 1522–1526.
- 13 Y. Yang, M. Forster, Y. Ling, G. Wang, T. Zhai, Y. Tong, A. J. Cowan and Y. Li, *Angew. Chem., Int. Ed.*, 2016, **55**, 3403–3407.
- 14 T. Hisatomi, F. Le Formal, M. Cornuz, J. Brillet, N. Tétreault, K. Sivula and M. Grätzel, *Energy Environ. Sci.*, 2011, **4**, 2512–2515.
- 15 M. Barroso, C. A. Mesa, S. R. Pendlebury, A. J. Cowan, T. Hisatomi, K. Sivula, M. Grätzel, D. R. Klug and J. R. Durrant, *Proc. Natl. Acad. Sci. U. S. A.*, 2012, **109**, 15640–15645.
- 16 C. Du, M. Zhang, J.-W. Jang, Y. Liu, G.-Y. Liu and D. Wang, *J. Phys. Chem. C*, 2014, **118**, 17054–17059.
- 17 L. Steier, I. Herraiz-Cardona, S. Gimenez, F. Fabregat-Santiago, J. Bisquert, S. D. Tilley and M. Grätzel, *Adv. Funct. Mater.*, 2014, **24**, 7681–7688.
- 18 R. Liu, Z. Zheng, J. Spurgeon and X. Yang, *Energy Environ. Sci.*, 2014, **7**, 2504–2517.
- 19 T. Wang, Z. Luo, C. Li and J. Gong, *Chem. Soc. Rev.*, 2014, **43**, 7469–7484.
- 20 O. Zandi, B. M. Klahr and T. W. Hamann, *Energy Environ. Sci.*, 2013, **6**, 634–642.
- 21 X. Yang, R. Liu, C. Du, P. Dai, Z. Zheng and D. Wang, *ACS Appl. Mater. Interfaces*, 2014, **6**, 12005–12011.
- 22 X. Li, P. S. Bassi, P. P. Boix, Y. Fang and L. H. Wong, *ACS Appl. Mater. Interfaces*, 2015, **7**, 16960–16966.
- 23 F. Le Formal, N. Tétreault, M. Cornuz, T. Moehl, M. Grätzel and K. Sivula, *Chem. Sci.*, 2011, **2**, 737–743.
- 24 F. Le Formal, K. Sivula and M. Grätzel, *J. Phys. Chem. C*, 2012, **116**, 26707–26720.
- 25 B. Klahr and T. Hamann, *J. Phys. Chem. C*, 2014, **118**, 10393–10399.
- 26 M. G. Ahmed, I. E. Kretschmer, T. A. Kandiel, A. Y. Ahmed, F. A. Rashwan and D. W. Bahnemann, *ACS Appl. Mater. Interfaces*, 2015, **7**, 24053–24062.
- 27 M. Forster, R. J. Potter, Y. Ling, Y. Yang, D. R. Klug, Y. Li and A. J. Cowan, *Chem. Sci.*, 2015, **6**, 4009–4016.
- 28 W.-J. Chun, A. Ishikawa, H. Fujisawa, T. Takata, J. N. Kondo, M. Hara, M. Kawai, Y. Matsumoto and K. Domen, *J. Phys. Chem. B*, 2003, **107**, 1798–1803.
- 29 C. Chanceliere, J. Autran, R. Devine and B. Balland, *Mater. Sci. Eng., R*, 1998, **22**, 269–322.
- 30 P. Zhang, J. Zhang and J. Gong, *Chem. Soc. Rev.*, 2014, **43**, 4395–4422.
- 31 V. Aroutiounian, V. Arakelyan, G. Shahnazaryan, G. Stepanyan, J. A. Turner and O. Khaselev, *Int. J. Hydrogen Energy*, 2002, **27**, 33–38.
- 32 C. Jorand-Sartoretto, B. D. Alexander, R. Solarska, I. A. Rutkowska, J. Augustynski and R. Cerny, *J. Phys. Chem. B*, 2005, **109**, 13685–13692.
- 33 Y. Fu, C.-L. Dong, Z. Zhou, W.-Y. Lee, J. Chen, P. Guo, L. Zhao and S. Shen, *Phys. Chem. Chem. Phys.*, 2016, **18**, 3846–3853.
- 34 X. Zhang, H. Li, S. Wang, F.-R. F. Fan and A. J. Bard, *J. Phys. Chem. C*, 2014, **118**, 16842–16850.
- 35 C. Li, T. Wang, Z. Luo, D. Zhang and J. Gong, *Chem. Commun.*, 2015, **51**, 7290–7293.
- 36 M. Forster, R. J. Potter, Y. Yang, Y. Li and A. J. Cowan, *ChemPhotoChem*, 2018, **2**, 183–189.
- 37 J. A. Klug, N. G. Becker, S. C. Riha, A. B. Martinson, J. W. Elam, M. J. Pellin and T. Proslir, *J. Mater. Chem. A*, 2013, **1**, 11607–11613.



- 38 T. Suntola, *Thin Solid Films*, 1992, **216**, 84–89.
- 39 K. Kukli, M. Ritala and M. Leskelä, *J. Electrochem. Soc.*, 1995, **142**, 1670–1675.
- 40 K. Lahtonen, M. Lampimäki, P. Jussila, M. Hirsimäki and M. Valden, *Rev. Sci. Instrum.*, 2006, **77**, 083901.
- 41 J. H. Scofield, *J. Electron Spectrosc. Relat. Phenom.*, 1976, **8**, 129–137.
- 42 J. Jokinen, J. Keinonen, P. Tikkanen, A. Kuronen, T. Ahlgren and K. Nordlund, *Nucl. Instrum. Methods Phys. Res., Sect. B*, 1996, **119**, 533–542.
- 43 M. C. Biesinger, B. P. Payne, A. P. Grosvenor, L. W. Lau, A. R. Gerson and R. S. C. Smart, *Appl. Surf. Sci.*, 2011, **257**, 2717–2730.
- 44 B. Klahr, S. Gimenez, F. Fabregat-Santiago, T. Hamann and J. Bisquert, *J. Am. Chem. Soc.*, 2012, **134**, 4294–4302.
- 45 B. Klahr, S. Gimenez, F. Fabregat-Santiago, J. Bisquert and T. W. Hamann, *Energy Environ. Sci.*, 2012, **5**, 7626–7636.
- 46 O. Zandi and T. W. Hamann, *Nat. Chem.*, 2016, **8**, 778–783.
- 47 S. R. Pendlebury, X. Wang, F. Le Formal, M. Cornuz, A. Kafzas, S. D. Tilley, M. Grätzel and J. R. Durrant, *J. Am. Chem. Soc.*, 2014, **136**, 9854–9857.
- 48 T.-P. Ruoko, K. Kaunisto, M. Bärtsch, J. Pohjola, A. Hiltunen, M. Niederberger, N. V. Tkachenko and H. Lemmetyinen, *J. Phys. Chem. Lett.*, 2015, **6**, 2859–2864.
- 49 D. Monllor-Satoca, M. Bärtsch, C. Fàbrega, A. Genç, S. Reinhard, T. Andreu, J. Arbiol, M. Niederberger and J. R. Morante, *Energy Environ. Sci.*, 2015, **8**, 3242–3254.
- 50 A. J. Cowan, C. J. Barnett, S. R. Pendlebury, M. Barroso, K. Sivula, M. Grätzel, J. R. Durrant and D. R. Klug, *J. Am. Chem. Soc.*, 2011, **133**, 10134–10140.
- 51 B. Zhang, X. Zheng, O. Voznyy, R. Comin, M. Bajdich, M. Garcia-Melchor, L. Han, J. Xu, M. Liu, L. Zheng, F. P. García de Arquer, C. T. Dinh, F. Fan, M. Yuan, E. Yassitepe, N. Chen, T. Regier, P. Liu, Y. Li, P. De Luna, A. Janmohamed, H. L. Xin, H. Yang, A. Vojvodic and E. H. Sargent, *Science*, 2016, **352**, 333–337.
- 52 F. Le Formal, S. R. Pendlebury, M. Cornuz, S. D. Tilley, M. Grätzel and J. R. Durrant, *J. Am. Chem. Soc.*, 2014, **136**, 2564–2574.
- 53 S. Sorenson, E. Driscoll, S. Haghighat and J. M. Dawlaty, *J. Phys. Chem. C*, 2014, **118**, 23621–23626.
- 54 A. Hiltunen, T.-P. Ruoko, T. Iivonen, K. Lahtonen, H. Ali-Löytty, E. Sarlin, M. Valden, M. Leskelä and N. Tkachenko, *Sustainable Energy Fuels*, 2018, **2**, 2124–2130.
- 55 A. G. Joly, J. R. Williams, S. A. Chambers, G. Xiong, W. P. Hess and D. M. Laman, *J. Appl. Phys.*, 2006, **99**, 053521.
- 56 L. Fu, Z. Wu, X. Ai, J. Zhang, Y. Nie, S. Xie, G. Yang and B. Zou, *J. Chem. Phys.*, 2004, **120**, 3406–3413.
- 57 J. Husek, A. Cirri, S. Biswas and L. R. Baker, *Chem. Sci.*, 2017, **8**, 8170–8178.





## IV

### Ultrathin-walled 3D inorganic nanostructured networks templated from crosslinked cellulose nanocrystal aerogels

by

Arto Hiltunen, Tyler Or, Kimmo Lahtonen, Harri Ali-Löytty, Nikolai Tkachenko,  
Mika Valden, Essi Sarlin, Emily D. Cranston, Jose M. Moran-Mirabal, and Jaana  
Vapaavuori

manuscript (submitted)





